Development of the Flash-heating Method for Measuring Melting Temperatures in the Diamond Anvil Cell

Dissertation
zur Erlangung des Doktorgrades
der Naturwissenschaften

vorgelegt beim Fachbereich Geowissenschaften/Geographie
der Johann Wolfgang Goethe-Universität
in Frankfurt am Main

von

Amol Karandikar
aus Mumbai, India

Frankfurt (2016)
(D 30)

vom Fachbereich Geowissenschaften/Geographie der

Johann Wolfgang Goethe-Universität als Dissertation angenommen.

Dekan : Prof. Dr. Ulrich Achatz

Gutachter : Prof. Dr. Björn Winkler
Prof. Dr. Lars Ehm

Datum der Disputation : 15 September 2016

Zusammenfassung der Doktorarbeit

Entwicklung der Laserpuls Heizmethode zur Messung von Schmelztemperaturen in der Diamantstempelzelle

Die Änderung der Schmelztemperatur einer Substanz unter hohen Drücken ist insbesondere in den Erd- und Materialwissenschaften von Interesse und deren Messungen sind für die Entwicklung bisher unzureichender theoretischer Modelle von grosser Wichtigkeit. In den Erdwissenschaften spielen Schmelzeigenschaften bei hohen Drücken eine wichtige Rolle bei der Interpretation seismischer Daten und der Modellierung dynamischer Prozesse. Insbesondere sind die Schmelztemperaturen von Eisen (Fe) und seiner Verbindungen mit Elementen kleiner Ordnungszahl an der Grenze des inneren Kerns (einem Druck von 330 GPa entsprechend) ein Schlüssel zur Abschätzung der Kerntemperatur. Da eine Messung von Schmelztemperaturen mit der notwendigen Genauigkeit bei solch extremen Bedingungen (über 300 GPa und 4000 K) nicht möglich ist, müssen bei niedrigeren Drücken gemessene Daten angemessen extrapoliert werden. Dies erfordert die genaue Messung von Schmelzkurven bei P-T-Bedingungen, die mit den verfügbaren experimentellen Techniken erreichbar sind.

Die einzigen verfügbaren Methoden zur Messung von Schmelztemperaturen bei solchen P-T-Bedingungen sind shock-compression (SC) und die lasergeheizte Diamantstempelzelle (LHDAC). Obwohl diese P-T-Bedingungen routinemäßig mit diesen Techniken erreicht werden können, ist die Messung von Schmelztemperaturen immer noch ein experimentelles Problem und bisherige Daten zeigen erhebliche Streuung.

Die Hauptgründe dafür sind bei der LHDAC Methode die sehr kleinen Probenvolumina ($< 10^{-3}$ mm^3) und die Identifikation von noch kleineren Schmelzvolumen und bei Stoßwellenexperimenten die extrem kurzen Zeitdauern.

Die Abweichungen der gemessenen Schmelztemperaturen für Metalle wie Eisen und hochschmelzende Metalle wie Ta, W, Mo (wichtig in den Materialwissenschaften) sind mehrere Tausend Grad, die genauen Gründe sind nicht bekannt und reflektieren die experimentellen Schwierigkeiten solcher Messungen.

Die Unsicherheiten bei Stoßwellenexperimenten sind im Wesentlichen:

1. In der direkten pyrometrischen Messung von Temperaturen wird die thermische Strahlung der geschockten Probe, die durch ein optisches Fenster beobachtet wird, durch die optischen und thermi-schen Eigenschaften des Fenstermaterials verzerrt. Durch unzureichende Kenntnis dieser Eigenschaften bei extremen P-T-Bedingungen und ihre komplexe Zeitabhängigkeit sind Korrekturen von mehr als 500 K auf die Schmelztemperatur notwendig.

2. Aus thermodynamischen Modellen berechnete Temperaturen haben typischerweise eine Unsicherheit von ±500 K.

3. Extreme Heizraten (10^9-10^{13} K/s) in shock-compression Experimenten können die Probe im festen Zustand weit über die Schmelzkurve hinaus überhitzen.

Die Hauptschwierigkeiten in der Feststellung von Schmelzen und Messung der Schmelztemperatur bei der Verwendung von continuous wave Laserheizung durch winkeldispersive Röntgenbeugung (ADXRD), Brillouin/Mössbauer-Spektroskopie und Beobachtung von Textur und Konvektion in der Schmelze sind die folgenden:

1. Ein idealer Weg zur Messung der Schmelztemperatur in der DAC ist es, die gesamte Probe lang genug geschmolzen und stabil eingeschlossen zu haben, um mit spektroskopischen Mitteln die Temperatur zu bestimmen und die Schmelze *in situ* mit winkeldispersiver Röntgenbeugung zu charakterisieren. Die ADXRD misst die radiale Verteilungsfunktion oder Strukturfaktoren der Schmelze, die sich von denen der festen Phase unterscheiden. Allerdings können bei der Verwendung von CW Lasern innerhalb weniger Sekunden im Bereich der Schmelztemperatur Instabilitäten, sowie Dispersion der Schmelze in das umgebende Material, unkontrollierbare Laserabsorption mit sprunghaftem Anstieg der Temperatur (thermal runaway) und chemische Reaktion der Probe mit Umgebung oder Diamant auftreten.

2. Weiterhin führt das kleine Schmelzvolumen (a) leicht zu optischer Fehljustierung und dadurch erheblichen Fehlern bei spektroskopischen Temperaturmessungen und (b) bei Röntgenbestimmungen zu ungenügenden Beugungsintensitäten.

Anstrengungen, diese Schwierigkeiten zu überwinden, hatten nur be-

grenzten Erfolg. Beispielsweise können viele der Schwierigkeiten durch eine drastische Reduzierung der Heizzeiten überwunden oder minimiert werden. Zwar ist gepulstes Laserheizen mit Mikro- oder Picosekunden Pulsbreiten und synchronisiertem Detektor (gated CCD) zur schnellen Temperaturmessung möglich, aber die extrem kurzen Heizzeiten machen Messungen der Höchsttemperatur ungenau.

In ADXRD Experimenten an Synchrotronstrahlungsquellen für Schmelzstudien in der LHDAC ist das Schmelzkriterium das Erkennung diffuser Beugungsringe und/oder das Auftreten von Rekristallisation. Der Röntgendetektor benötigt Belichtungszeiten von einigen Sekunden und dies verursacht meistens erhebliche Diffusion der Schmelze in das umgebende Medium oder eine chemische Reaktion. Selbst bei computerkontrolliertem inkrementellem Heizen und schnellen XRD Techniken kann die Heizdauer pro Röntgenbelichtung nicht unter einige Sekunden reduziert werden.

Zwei weitere Techniken, die das Problem der Detektion kleiner Schmelzanteile vermeiden, sind die ,,speckle“ Methode und die ,,melt-quench“ (Abschreck-)Methode. Diese beruhen auf der optischen Beobachtung von Schmelzen durch texturelle Änderungen der Probenoberfläche. Diese Techniken sind vergleichsweise einfach auszuführen.

In der ersten Methode wird Schmelzen durch eine Konvektionsbewegung der Schmelze und kontinuierliche Bewegung der Laserspecklemuster, die von der Probe reflektiert werden, detektiert.

In der zweiten Methode wird die Oberflächentextur in Abschreckversuchen untersucht und das Auftreten eines glänzenden Kraters als Schmelzkriterium verstanden. Diese Methoden haben allerdings Einschränkungen: mit zunehmendem Druck verringert sich die Bewegung des Specklemusters erheblich und texturelle Veränderungen können auch durch chemische Reaktionen verursacht werden. Um die Möglichkeit einer chemischen Reaktion auszuschließen zu können müssen komplementäre Untersuchungen wie *in situ* Raman-Spektroskopie oder *ex situ* chemische Analyse unter Verwendung von energiedispersiver Röntgenspektroskopie (EDS) an den zurückgewonnenen Proben durchgeführt werden.

Zusammenfassend gibt es bisher keine Methode zur Messung von Schmelztemperaturen, die alle bisherigen Schwierigkeiten umgeht.

In dieser Dissertation präsentiere ich die Entwicklung einer neuen Methode der Messung von Schmelztemperaturen von Metallen bei Drücken von 10-100 GPa und Temperaturen von 2000-5000 K in der lasergeheizten Diamantstempelzelle (LHDAC). Diese Methode verhindert die vormaligen Schwierigkeiten, die durch lange Heizdauern entstehen, beispielsweise die Probeninstabilität, Dispersion der Schmelze in das umgebende Druckmedium, thermischen runaway oder chemische Reaktionen bei gleichzeitiger genauer spektroskopischer Messung der Temperatur. Weiterhin vermeidet sie die Mängel von kurz-gepulster Laserheizung und nutzt ein Schmelzkriterium, das konsistent mit der bekannten Schmelztemperatur bei Normaldruck ist. Ausserdem umfasst die Messung eine sorgfältige chemische und texturelle Untersuchung der wiedergewonnenen Proben.

Im experimentellen Aufbau wird ein Ytterbium Faserlaser (λ = 1070 nm, TEM_{00} Modus, kontinuierlich) mit einem Pulsgenerator moduliert, so dass ein rechteckiger Puls (flash) für eine gewisse Zeit (typisch 20 ms) produziert wird. Bedingt durch die extrem geringe Masse der Probe sind die Aufheiz- und Abkühldauern fast vernachlässigbar und die Probentemperatur ist für 20 ms nahezu konstant. Diese Heißdauer ist lang genug, um die Temperatur genau zu messen und kurz genug, um chemische Reaktionen in der Probenkammer und Probeninstabilitäten zu vermeiden. Der Laserpuls und die thermische Emission der Probe werden mit eine Photodiode bzw. mit einem Photomultiplier gemessen.

Bei hohem Druck wird eine Flash-Schmelzmessung wie folgt durchgeführt: Mikroskopbilder der Probe (25-50 μm Durchmesser, 5-10 μm dick) werden vor und nach der Ladung in die DAC aufgenommen. Die Probe wird thermisch in der DAC durch ein chemisch inertes Druckübertragungsmedium isoliert. Der Laser wird defokussiert, um einen Heizpunkt mit einem Temperaturgradienten kleiner 10 K über die zentrale Probenfläche (< 5 μm) zu erzeugen. Die Probe wird dann durch einen einzigen 20 ms-Puls geheizt und die Temperatur durch spektrale Radiometrie nach dem Planckschen Gesetz gemessen. Mikroskopbilder werden vor und erneut nach Entladen der Proben aufgenom-

men. Bei einem gewissen Druck wird eine Versuchsreihe bei Temperaturen von 500 K unter und oberhalb der Temperatur durchgeführt, bei der ein glänzender Kranz in der geheizten Fläche erscheint und Schmelzen anzeigt. Die zurückgewonnenen Proben werden mit dem Rasterelektronenmikroskop (REM) auf ihre Topographie, mit EDS auf chemische Spuren und mit der Focused Ion Beam Milling (FIBM) Technik zur Messung der Tiefe der Schmelzereignisse untersucht. EDS hat eine Sensitivität von 0.1-0.2% in der Kohlenstoff- und Sauerstoffdetektion, wesentlich genauer als die Detektionsmöglichkeiten von Standard-XRD.

Das Schmelzkriterium ist die Bildung eines Kraters, der eine komplette Restrukturierung der Probenmasse mit einer Tiefe von einigen Mikrometern zeigt. Diese Restrukturierung ist eindeutig mit der REM und FIBM Analyse nachweisbar. Dieses Kriterium ist identisch mit demjenigen, das bei den bei Atmosphärendruck bekannten Schmelztemperaturen der Proben beobachtet wurde. Die Daten bei Atmosphärendruck wurden durch Flash-Heizen der Proben (Folien) in einer inerten Um-gebung und ebenfalls mittels Analyse durch REM, EDS und FIBM erzeugt. Die Unsicherheit in der Schmelztemperatur wird als Differenz zwischen der niedrigsten Temperatur für Schmelzmerkmale und der höchsten Temperatur für Festkörpermerkmale berechnet. Die Unsicherheit ist typischer Weise kleiner als ±100 K und kann durch Vergrößerung der Anzahl der Messungen verbessert werden.

Wegen ihrer Wichtigkeit in der Materialwissenschaft und zur Lösung des Problems der extremen Diskrepanzen in den Schmelztemperaturen wurden die Schmelzkurven der hochschmelzenden Metalle Re, Mo und Ta mit der Flash-Laserheizmethode gemessen.

Die scheibenförmigen Re und Ta Proben wurden mittels eines Lasers aus dünnen Folien herausgeschnitten. Die Proben wurden poliert, gereinigt und mit Argon als Druckübertragungsmedium in einer 0.3 GPa Gasapparatur in die Diamantstempelzelle DAC geladen. Mo Proben wurden durch Flachdrücken von Mo Körnern zwischen Diamantstempeln erzeugt. Dünne Platten von Saphir isolierten die Proben thermisch vom Diamant. Druck wurde durch Rubinfluoreszenz von Rubinkörnern oder durch Raman-Spektroskopie an Diamant bestimmt. Gaskets aus Re dienten als Probenkammern. Die culet Durchmesser der Diamanten betrugen 100-200 μm.

In Re und Mo Experimenten wurden die Probe an verschiedenen Stellen Flash-lasergeheizt während die jeweilige Temperatur unter- und oberhalb des Schmelzens (Auftreten eines glänzenden Kraters) aufgenommen wurde. Dieses limitiert die Anzahl von Experimenten bei einem gewissen Druck an einer Probe. Im Fall von Ta wurde nur eine Einzelpulsmessung pro Probe durchgeführt. Dies erlaubte stärkere Defokussierung und erhöhte Genauigkeit der Temperaturmessung im Vergleich zu den Re und Mo Experimenten.

Schmelztemperaturen von hcp-Re wurden bis 48 GPa und 4600 K gemessen - eine fünffache Erweiterung des bisher bekannten Datenbereichs. Druck verstärkt den hochschmelzenden Charakter von Re drastisch und oberhalb von 20 GPa wird es zum Metall mit dem höchsten Schmelzpunkt, da seine Schmelzkurve erheblich steiler als die von Wolfram ist.

Die Schmelzkurve von bcc-Mo wurde bis 45 GPa und 3100 K gemessen. Sie ist konsistent mit der zuvor gemessenen relativ flachen Schmelzkurve, die in der LHDAC mit ADXRD und der Speckle-Methode gemessen worden war. Sie hat deshalb als Testfall für die Reproduzierbarkeit von Flash-Schmelzen gedient. Diese flache Schmelzkurve ist drastisch verschieden von der aus Stoßwellenversuchen abgeleiteten.

Die Schmelzkurve von bcc-Ta wurde bis 85 GPa und 4300 K gemessen. Im Gegensatz zu vorherigen Experimenten wurde diese Schmelzkurve durch unzweideutige Erkennung des Schmelzens und ohne chemische Reaktion gemessen und damit, verglichen mit bisherigen Messungen, eine erheblich höhere Genauigkeit erziehlt. Die Schmelzkurve liegt höher als die bislang veröffentlichte flach-ansteigende Schmelzkurve aus der LHDAC, ist aber tiefer als die meisten Kurven aus Theorie, Schockdaten und ADXRD Messungen aus der LHDAC. Zum ersten Mal wurden sowohl texturelle als auch chemische Veränderungen der Proben beim Schmelzen durch Mikroskopie der wiedergewonnenen Proben beobachtet. Weitere Analysen der zurückgewonnenen Schmelze durch Transelektronenmikroskopie (TEM) mag wichtige strukturelle Informationen zu vorhergesagten strukturellen Übergängen in Ta liefern.

Die Flash-Schmelzmethode ist im Druck limitiert, bedingt durch die abnehmende Probengröße und zunehmende Probleme bei der optischen Justierung.

Diese Dissertation zeigt, dass die neue Methode „Flash-Heizen in der DAC“ auf einer Zeitskala von Millisekunden alle bisherigen experimentellen Probleme in der LHDAC bei langen Heizdauern zum grossen Teil verhindert und zudem eine Brücke zwischen Schockexperimenten und statischen Methoden beim Schmelzen bei hohen P-T-Bedingungen schlägt. Sie erlaubt weiterhin Analyse und Charakterisierung der zurückgewonnenen Proben in REM, FIBM, EDS und TEM.

——o|o——

Contents

Chapter 1

Melting phenomenon in the diamond anvil cell

1.1 Introduction

Melting is a commonplace phenomenon in nature, and changes in the melting temperature of a substance under different conditions like varying pressure are of significance in our everyday life, e.g.

1. Lowering of the melting temperature of ice under pressure[1] is the very reason we slip or slide on ice.

2. Most metals, when heated, start losing their mechanical strength at temperatures as low as half of their melting temperatures[2]. Since the melting temperature is known to vary under pressure or stressed conditions, and metals being an integral part of civil constructions, monitoring of their melting behaviour under different physical conditions becomes imperative.

3. Life on the Earth is protected by its magnetic field from the charged particles in the solar wind that can harm the ozone layer[3]. The Earth's magnetic field originates from convection of fluids containing iron and its compounds in the interior, and it is partly governed by the distribution of temperature at different depths (pressures)[4]. To model the dynamic processes responsible for the geodynamo is a fundamental scientific problem in Geoscience, which demands accurate measurements of melting temperatures, and of the structure of iron and its compounds at pressures representing different depths[5].

Such examples underline the importance of knowing the dependence of a melting temperature on pressure. Predicting the nature of such dependence has been a difficult task, as many experimentally measured melting curves present a wide variety of melting behaviour[6]. Such measurements under extreme conditions of pressure and temperature are technically challenging, and for decades, enormous efforts have been made to improve the techniques.

Melting: Thermodynamically, a substance is said to melt when the Gibbs free energy (G) of its solid and liquid forms are equal at a given pressure.

If U: internal energy, P: pressure, V: volume, T: temperature, S: entropy, the Gibbs free energy is $G = U + PV - TS$, and melting occurs when

$$G_{solid}(P, T_m) = G_{liquid}(P, T_m), \quad \text{where } T_m\text{: melting temperature.}$$

At this condition, the solid and liquid phases co-exist in equilibrium. The amount of liquid present depends on the thermal energy or the latent heat supplied to the substance since its arrival at the co-existence condition[7].

Since the numerical difference between G for solid and liquid phases of a material is very small compared to their individual G values, while calculating melting temperatures by numerical methods using a computer, the resulting melting temperatures highly rely on the precision of G values[8]. In addition, difficulties in computationally simulating different physical and chemical conditions increase the complexity of calculations. In such cases, accurately measured melting temperatures often provide constraints for testing the theories.

In order to measure a melting temperature experimentally, it is imperative to identify the condition under which melting takes place. Such a condition is called a 'criterion for melting' or a 'melt-criterion'.

Since the early 20th century, many melt-criteria were suggested based on the atomic nature of substance, namely the amplitude of atomic vibrations exceeding a threshold[9–11], instability caused by vibrational motion of two simple, rigid sublattices against each other[12], diminishing of the 2nd derivative of lattice energy with respect to lattice spacing[13], minimisation of pressure with volume change[14], structural order-disorder transition[15–17] , and failure of elastic resistance against a shearing stress[18].

Many of these criteria are used in theoretical calculations of melting curves but cannot be directly implemented in experimental measurements unless the criteria are manifested in certain measurable or observable properties of the substance.

For instance, Born's criterion[19] for melting is perhaps the only one that uses the most evident difference between solid and liquid states, namely a solid resists elastically against a shearing stress while liquid does not. In other words, the shear modulus becomes zero at melting, resulting in a discontinuity in the temperature dependence of sound velocity in the material. This criterion can be implemented theoretically as well as experimentally at ambient and at high pressures.

In practice, depending on the nature of a substance, a criterion needs to be chosen that allows an identification of melting in a certain measurable or observable property.

1.2 Melting at high pressure

Detecting an onset of melting while measuring temperature at that instant becomes increasingly difficult as the pressures and temperatures get higher, as discussed ahead.

For example, when a substance at ambient pressure is heated at a steady rate, its temperature rises steadily, assuming the heat loss to be insignificant. The instant at which the temperature becomes constant in time indicates an onset of melting, as the supplied heat energy is used as the 'heat of fusion' in the solid to liquid transformation.

Based on this phenomenon, the 'Differential Thermal Analysis' (DTA) technique is developed in which the temperature difference (ΔT) between a sample and a reference material is monitored while supplying the same amount of heat energy to both. The onset of melting (or freezing) while heating (or cooling) is distinctly identified by a plateau developed in the plot ΔT vs. $T_{reference}$ (or time).

For melting at moderately high pressures this method is adaptable to large volume presses like the Multi-Anvil Apparatus (MAA). However, compared to measurements at 1 atm, the smaller amount of sample results in a relatively weak signal over the background, making the onset of melting less prominent to detect. It is the derivative of ΔT with $T_{reference}$ (or time) that distinctly indicates melting[20].

However, above the pressures reached by the MAA, adapting this method to a routinely used diamond anvil cell (DAC) apparatus is not practical. The heat of fusion to melt a typical sample (diameter 50 μm, thickness 10 μm) in a DAC turns out to be ∼100 μJ or less, which is an insignificant fraction of the total heat supplied to the sample, and beyond the detection capabilities of standard detectors used.

In such cases, melting curves calculated by computational methods are helpful. Theoretically, the effect of pressure on the melting temperature has been widely explored. Clapeyron[21] described the P-T relation of coexisting gas and liquid phases on thermodynamic basis, that was extended to solid and liquid phases by Clausius[22]. It can be derived directly from the Gibbs free energy criterion for melting at pressure P as:

$$\mathrm{d}T_m/\mathrm{d}P = (V_L - V_S) / (S_L - S_S) = T_m \, \Delta V_m / H_f$$

where V_L, S_L and V_S, S_S are the specific volume and entropy of liquid and solid phases, respectively; ΔV_m and H_f indicate the volume difference and latent heat of fusion at the melting temperature T_m, respectively.

Several semi-empirical laws (Simon-Glatzel[23;24], Kraut-Kennedy[25;26]) and melting-models (e.g. dislocation mediated melting[27–29]) developed predict melting temperatures in the P-T regime where creating the experimental conditions is difficult. Yet, an experimental report of a melting curve having an unusual nature, like that of lithium[30] that melts below the room temperature between 40-65 GPa, questions our understanding of the melting behaviour even at moderate P-T conditions.

Such cases demand validation of theoretical predictions and revalidation of the existing melting curves with suitable criteria that allow accurate measurements on melting temperatures.

1.3 Diamond anvil cell and melt-criteria

1.3.1 Reaching high P-T conditions by static compression

In static compression[31], steady pressure is applied for a duration much longer than that required for thermal transport in or out of a sample, e.g. of the order of seconds or more for a sample few micrometres in dimension. Thus, the compression is isothermal at the temperature of the

surroundings, and external heating is required to raise the temperature of the sample. Different apparatus used to reach high temperatures with static compression are briefly described as follows.

Among the large volume apparatus, namely the piston-cylinder, belt apparatus, toroid anvil, Bridgman anvil, and MAA, the highest pressures reached are with MAA. With recent advances in nano-polycrystalline diamond anvils in MAA, pressures as high as 125 GPa can be attained[32] but the standard MAA employing tungsten carbide anvils are still limited in pressures to < 28 GPa and temperatures < 2800 K[33]. In some MAA 3000 K[34] can be reached but at modest pressures (< 15 GPa). Beyond the limit of the strength of typical large volume presses, the pressure intensification is achieved at the expense of reducing the sample volume from tens of mm^3 to less than 10^{-3} mm^3. The pressure cells become very compact, yet suffice to generate very high pressures. Other than diamond, the materials used for anvils in these cells include cubic zirconia (ZrO_2)[35], sapphire (Al_2O_3)[35;36] and moissanite (SiC)[37;38]. These have been tested to about 17, 26 and 59 GPa, respectively and their high temperature behaviour is unexplored.

A DAC, when heated as a whole externally[39;40] or heated 'resistively' with heaters surrounding the anvils[41–45] barely allows temperatures to reach 1300 K due to mechanical instability and chemical reactivity of different parts of the cell. When heated internally within the sample chamber[46–48], it can reach about 3000 K[49]. However, these heating procedures become increasingly impractical to implement above moderately high pressures due to pressure gradients causing deformation or failure of the heating circuit[50]. To avoid this problem, in the recent 'designer anvils' the heating elements and the measuring probes are fabricated on the culets with the sample sputtered in shape of a sheet on a heating element. These have been tested to 21 GPa and 2000 K[50].

The laser-heated diamond anvil cell (LHDAC) is the only apparatus that has reached static pressures in excess of 350 GPa[51] and allowed measurement of temperatures above 5000 K[5;51;52]. Diamond is transparent to electromagnetic radiation in a wavelength range from infrared to X-rays. This property of diamond facilitates heating of metals and non metals using suitable laser wavelengths, ~1 μm and ~10 μm, respectively. Moreover, the *in-situ* characterisation of samples using probes like X-ray (diffraction / absorption), Raman[48;53;54] and Brillouin spectroscopy[55–57] is possible by maintaining the sample in a thermal steady state for long

enough durations.

Since the advent of the laser-heating technique[58] in a DAC, advances in laser technology have made lasers more compact, more stable and reaching over 100 W with better quality of beams. Moreover, crucial improvements in the design of the diamond anvils and cells[59;60], specialised optical components and novel use of imaging detectors[61], and new synchrotron probes[62;63] have allowed improved or new criteria, and refined ways[64–66] of measuring melting temperatures at extreme P-T conditions.

1.3.2 Diamond anvil cell

As an example, one of the commonly used DAC for laser-heating, called as the 'plate-DAC' is shown in Fig. 1.1. Two jewel-cut diamonds, with their tips polished off to create a flat area (culet), are mounted on two tungsten carbide (WC) seats. The seats sit in two hardened steel plates. The diamond culets, the seats and the plates are aligned to be concentric using set-screws, and the culets are then made nearly parallel to each other by adjusting their tilt using the outer alignment screws.

To create a sample chamber, a hole smaller than the size of the culets is drilled in a metallic gasket which is preindented to a desired thickness. The diameters of culets and dimensions of the hole are decided by the pressure to be reached. The hole serves as a sample chamber containing a sample placed on a thermal insulator resting on the bottom culet along with a pressure marker, and an inert, thermally insulating pressure transmitting medium. The volume of a sample chamber that typically has 150 μm diameter and 40 μm thickness is 0.7 nL.

An external gear mechanism turns the inner screws simultaneously by an equal amount to bend the plates pivoting on the outer screws. This action advances the anvils towards each other to first seal the sample chamber, and squeeze the gasket further to reach the desired pressure. The sample is heated through the diamonds using infrared laser radiation and the temperature of the heated area is measured by spectroscopic means using the emitted thermal radiation (see Fig. 2.9). Procedural details of heating and measuring temperature are described in section 2.1. Detailed specifications and photographs of the cell are in Appendix A.

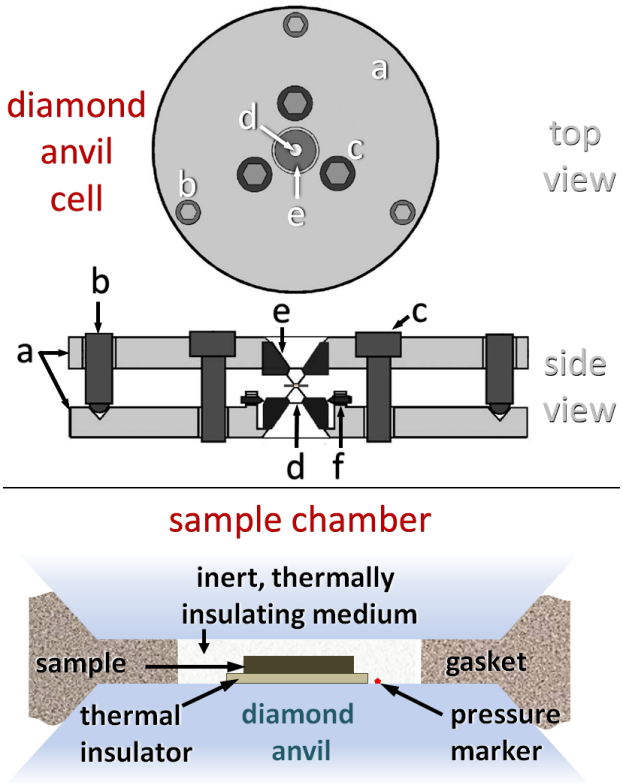

Figure 1.1: **DAC and sample chamber.** Schematic drawings of a plate-DAC from top and side views. a: steel plates. b: screws to adjust the tilt of plates. c: screws to bend the plates. d: diamond anvils. e: tungsten carbide seats. f: set screws for lateral seat alignment. For clarity, the side view is magnified compared to the top view. The top two drawings are adapted from ref. [60]. Below is a magnified view of the sample chamber. See text for description.

1.3.3 Overview of the melt-criteria

The criteria that have been prominently used in the DAC over the past three decades are described briefly with one of the first or selected examples as follows. The maximum *P*-*T* conditions reached in those experiments are mentioned in brackets.

1. In the early experiments on melting involving an internally, resistively heated DAC, a current was passed through the sample itself in the form of a wire (Fe[46]: 20 GPa, 2100 K, W[67]: 10 GPa, 3800 K) and its electrical resistance was monitored while measuring the temperature by optical pyrometry. Melting was inferred from fluctuation or discontinuities in the resistance plotted against temperature, and/or visual observations of melting (Fig. 1.2). In the recent 'designer anvils'[50], with a microcircuit for heating and measurement fabricated on the culets with the sample

(Sn[68]: 45 GPa, 2000 K) sputtered in shape of a sheet on the circuit, a large increase in resistance was considered as a signature of melting[69].

The use of these criteria is limited to sample materials which are ductile or can be sputtered, and to the maximum pressure, temperature reached by internal resistive heating as discussed earlier. Also, oxidation of metals upon prolonged heating was found to hamper the measurements[67].

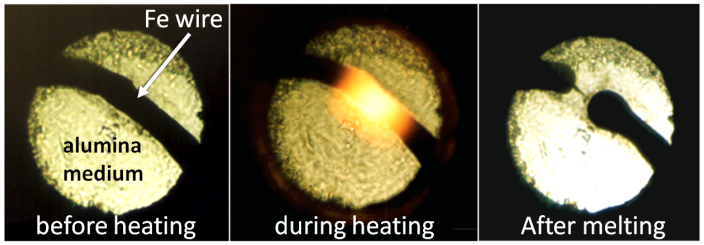

Figure 1.2: **Microphotographs of a resistively heated Fe wire in a DAC sample chamber.** Image courtesy: R. Boehler.

2. For nonmetallic samples (Na and K[70]: 15 GPa, 400 K) the whole DAC was externally heated and temperatures were measured by thermocouples attached to the diamonds. The onset of melting was detected by changes in shapes, surface textures and reflectivity of the samples monitored in reflected and transmitted light.

3. For optically transparent samples (Ar[71]: 6 GPa, 717 K), loaded in the externally or resistively heated DAC, melting was inferred by visual observations and interferometry. At lower pressures, disappearance of the crystal grain boundaries indicated melting. At higher pressures, in the transmitted white light, an interference pattern formed between the opposite anvils was observed to shift continuously due to changing refractive index of the sample with temperature. A strong discontinuous shift in the pattern coincided with melting. In some cases (H_2[72]: 17 GPa, 280 K, H_2O[73]: 13.1 GPa, 752 K), an appearance of aggregation of crystallites coexisting with the fluid indicated an onset of melting.

With the advent of stable and high power (~100 W) solid state lasers (Nd:YAG, YLF, Yb-Fibre, λ ~1 μm) and gas lasers (CO_2, λ: 10.64 μm), unlike the methods discussed above, metals and electrically insulating samples could be heated in a DAC to temperatures > 3000 K. With the

new possibility of local heating by controlling the laser focus, the electrical leads for heating or probing in a DAC became obsolete and the samples could be pressurised to much higher pressures. Similarly, thermocouples to measure temperatures were replaced by 'contactless' spectroscopic techniques. These technological advances brought in many new criteria.

4. Melting was inferred by observing formation of optically isotropic, circular blobs, several micrometres in diameter, upon quenching to room temperature ($Mg_{0.9}Fe_{0.1}SiO_3$ [8]: 65 GPa, 3000 K) or by detecting a hole in the sample with a sharp discontinuity in the laser power monitored against the measured temperature (Fe [74]: 40 GPa, 2300 K).

5. At the onset of melting, to detect any changes in surface texture or a distinct change in reflectivity or both, the sample was illuminated with a laser in the visible region ($\lambda \sim$488 nm). Melting was detected by a sharp decrease in the intensity of the reflected signal measured by a photo diode (Fe [75]: 120 GPa, 3000 K) to support visual observation of convecting motion of the melt in the heated area (FeO, FeS, FeS_2 [76]: 45 GPa, 2700 K).

6. The convective motion could more clearly be detected *in-situ* by sending the reflected laser light to a CCD camera, that recorded the 'speckle' pattern formed by the texture of the sample surface. Melting was inferred from the onset of a continuous movement of the speckles (Fig. 1.3) within the hotspot (Fe-FeS eutectic [77]: 65 GPa, 2200 K), whereas a discrete change in the speckle pattern was associated with a change in the surface texture due to chemical reaction or a solid-solid transition. This criterion was used for a various types of materials that could give rise to a speckle pattern, e.g. metals [78–83], noble gases [84], alkali halides [85], water [86].

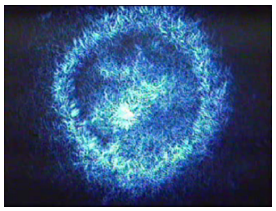

Figure 1.3: **CCD-image of a speckle pattern generated by illuminating the sample surface by a blue laser.**
The central bright portion is the centre of the hot spot generated by the heating-laser. Image courtesy: R. Boehler.

7. When heating silicates with a CO_2 laser, a dramatic increase in absorp-

tion of the laser radiation was observed near melting and round melt features with signs of recrystallisation were observed upon quenching from the high temperatures ((Mg,Fe)SiO_3[78]: 63 GPa, 5000 K, $CaSiO_3$[87]: 43 GPa, 4100 K). In some studies the 'speckle-motion' and 'sudden increase in laser radiation absorption' criteria were combined (LiF[85]: 102 GPa, 3500 K).

8. Laser-heated glassy substances (Pyrolite[88]: 60 GPa, 3400 K) were recovered and analysed using the Scanning Electron Microscope (SEM) and Atomic Force Microscope (AFM) to distinguish melt features from those for un-molten areas. Cracks developed in the heated zone indicated crystallisation of glass whereas the features with raised heights, quantitatively characterised by the AFM, were interpreted as the quenched melt (Fig. 1.4).

An improvement on this method was achieved by laser-heating a sample at different locations to different temperatures and analysing the quenched texture of the recovered sample optically and using the SEM (Ta[65]: 48 GPa, 3800 K). The melting was attributed to an appearance of a shiny, smooth, bead-like feature, distinct from the unmodified, rough texture of un-molten areas (Fig. 1.5).

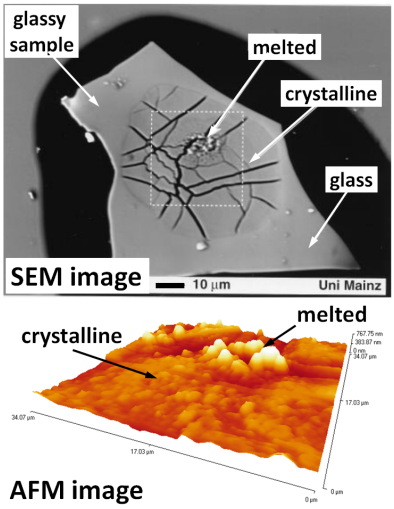

Figure 1.4: **Melt detection using SEM, AFM images.** Figure adapted from ref. [88]. See text for further description.

With the availability of synchrotron radiation sources, intense X-rays focussed to an area spanning a few micrometres have facilitated melting temperature measurements in a LHDAC using various X-ray techniques. These include Energy / Angle Dispersive X-ray Diffraction (EDXRD / ADXRD), Synchrotron Mössbauer Spectroscopy (SMS), and X-ray Absorption Spectroscopy (XAS). In these techniques, unlike in the previous methods, the axial temperature gradients in the sample are minimised by laser-heating through both the anvils while probing with X-rays. This way of heating is called 'double sided laser heating'.

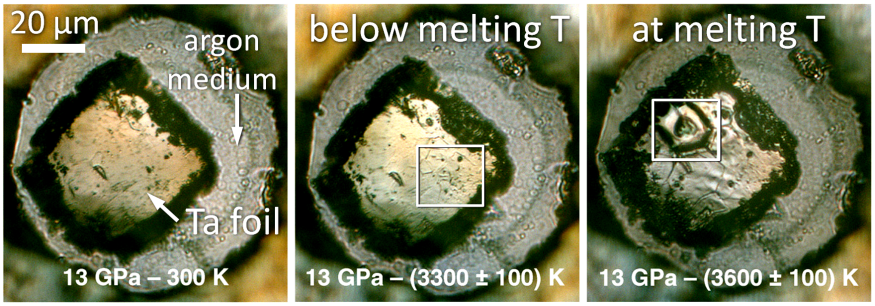

Figure 1.5: **Ta melting inferred from textural changes upon quenching.** White squares indicate areas heated with a continuous wave (CW) laser. Figure adapted from ref. [65].

Solids, with a long range order in their atomic arrangement, scatter X-rays coherently to produce characteristic Bragg peaks. Liquids, lacking this long range order, produce a diffuse scattered signal with a rise in the background around Bragg peaks. Melting is thus manifested in the X-ray diffraction patterns.

9. In the earlier EDXRD measurements using the LHDAC, intensity reduction and subsequent loss (disappearance) of diffraction peaks of the sample into the background were attributed to melting (Fe[89]: 65 GPa, 3000 K). Upon cooling, the intensities of the peaks were found to be restored to some extent and the same sample could be cycled through the solid-liquid transition (Fe[90]: 47 GPa, 3000 K). However, the intensity loss of the peaks could also be attributed to recrystallisation upon heating[91].

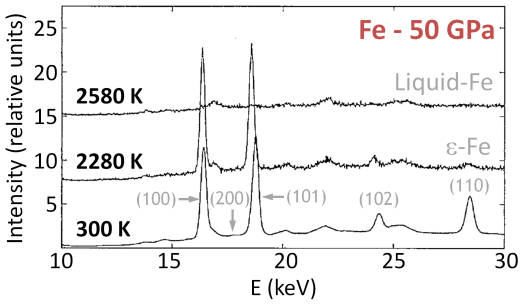

Figure 1.6: **Synchrotron EDXRD spectra for Fe melting in the LH-DAC.** The indexed peaks belong to the hcp (ϵ) phase. See text for description. Figure adapted from ref. [89].

With the development of the X-ray area detectors and the ADXRD technique, melting could be distinguished from recrystallisation. Observation of diffuse scattering from the melt with simultaneous disappear-

ance of all the crystalline diffraction peaks became the criterion for melting (In[91]: 3 GPa, 550 K). With this criterion, the much desired structure of the melt in the LHDAC was also measured (Fe[92]: 58 GPa, 2900 K). However, such measurements were difficult due to challenges in maintaining a sample in its liquid state long enough (few tens of seconds) to measure the structure.

With the improved experimental techniques, detecting changes in the XRD patterns was possible on a timescale of a few seconds, which also reduced the CW laser-heating time. With this technique, diffraction spots from the solid sample, either un-molten or unsteadily recrystallised from the melt were observed together with the diffuse scattering signal from the melt. Moreover, these XRD features indicating a solid-liquid equilibrium appeared along with a plateau in the measured temperature - laser power plot. Therefore, the melt-criterion using ADXRD was modified as 'appearance of a diffuse scattered ring and/or distinct spots due to recrystallisation' (Pb[93]: 80 GPa, 3700 K) (Fig. 1.7). The difficulties in following this criterion are discussed in detail in subsection 1.4.1.

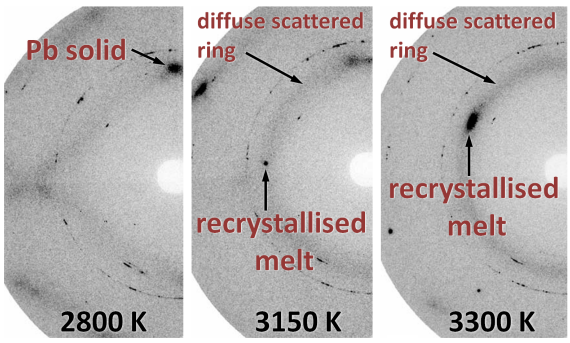

Figure 1.7: **Synchrotron ADXRD images of lead in the LHDAC at 65 GPa.** Diffraction spots from recrystallisation and a diffuse scattered ring from the melt are observed together. X-ray exposure time is 1 second. See text for description. Images adapted from ref. [93].

10. Energy dispersive X-ray absorption spectroscopy (EDXAS) provides structural information within a few Ångströms around the photoabsorbing atom with the same sensitivity, regardless of the physical state (crystalline, amorphous, or liquid) of the sample. In an XAS spectrum, the features at energies close to but lower than the X-ray absorption edge, namely the pre-edge 'shoulder' or peaks are attributed to different band-hybridisations, and the oscillations above the energy of the edge are related to the bond-distances of and around the photoabsorbing atom as well as to the degree of thermal disorder in the sample material[63;64].

In routine XAS, the energy of the incident X-ray is varied sequentially to cover the spectral range of interest and the exposure times involved are too long for melting studies. However, in the recent studies using a latest CCD-based position sensitive detector, the entire XAS spectrum could be captured in nanoseconds to seconds, making it possible to study melting in the LHDAC. In these studies, melting was inferred from broadening and disappearance of a peak in the pre-edge region, along with damping of the oscillations above the edge due to the increasing thermal disorder (Fe[64]: 78 GPa, 2900 K (Fig. 1.8), Fe[63]: 103 GPa, 3100 K) .

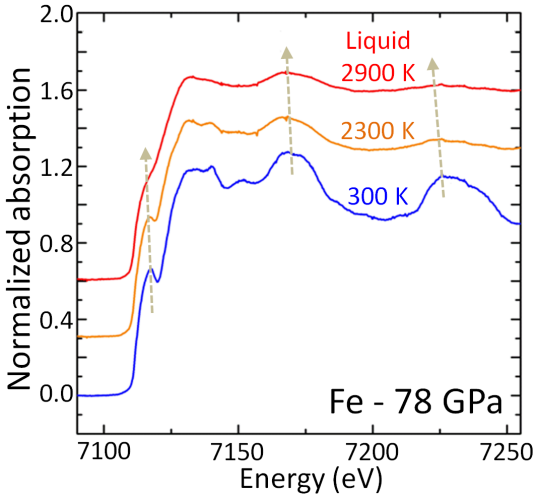

Figure 1.8: **EDXAS spectra for Fe in the LHDAC at 78 GPa.** The arrows indicate evolution of the characteristic features with temperature. See text for further description. Figure adapted from ref [64].

This method requires the sample to remain flat and maintain a uniform thickness during heating and while acquiring spectra, which is technically quite challenging.

11. Synchrotron Mössbauer Spectroscopy (SMS)[94] is the latest technique for detecting melting in the LHDAC. It monitors the motion of atoms (drift) from their equilibrium positions at the sub-Ångström scale, quantified as the Lamb-Mössbauer factor f. When this drift extends to tens of Ångström, f becomes exponentially small indicating presence of a liquid. For practical purposes, f $\rightarrow$ 0 indicates melting (Fe[62]: 82 GPa, 3025 K).

This method is limited in use because 1. not all synchrotron X-ray beamlines have energy resolution fine enough to tune in to the resonance energies of a known Mössbauer isotope (e.g. ^{57}Fe, ^{119}Sn) present in the sample, and 2. the isotope should be present in high enough quantity to generate an unambiguous spectroscopic signal.

12. Brillouin Spectroscopy exploits the most basic difference between the solid and liquid states, expressed by Born's criterion[19] of melting: the shear modulus vanishes at the melting transition as liquids do not support a shear stress but solids do. The criterion is manifested as an abrupt drop in the frequency of the longitudinal acoustic mode (Fig. 1.9) of the sample with respect to temperature, at the onset of melting (Ice[95]: 26 GPa, 1200 K). The drop is also reflected as a discontinuity in the sound velocity plotted against temperature. Moreover, the width of a scattered peak for liquid is distinguishably smaller than that for solid.

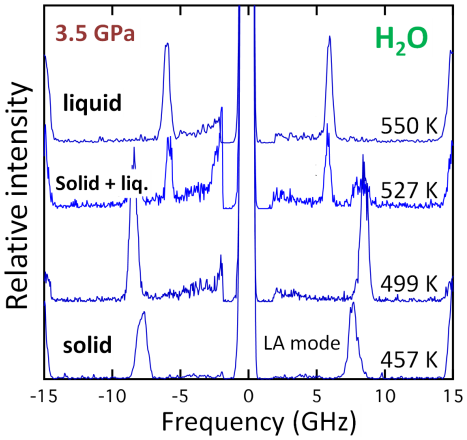

Figure 1.9: **Detecting ice melting in the LHDAC using Brillouin scattering.**
Temperature evolution of Brillouin spectra of ice at 3.5 GPa is shown. At the onset of melting, the longitudinal acoustic (LA) mode abruptly shifted to a lower frequency. Image adapted from ref. [95].

However, this spectroscopy is limited only to optically transparent and homogenous samples[55], and the acquisition times require the sample to be maintained in a steady state for several minutes/hours, which may not always be practically possible.

13. Raman spectroscopy (RS) probes excitations in energy associated with different kinds of degrees of freedom viz. vibrational, rotational, electronic, and those arising from lattice vibrations (optical phonons)[54;96]. Since the nature of degrees of freedom and symmetry are different in the solid and liquid phases of a material, RS, being sensitive to both, is used to infer melting. The materials that exhibit Raman active modes distinctly characterising the liquid state, can be probed for melting by RS e.g. silicates[97], N_2[98–100], H_2[99;101;102]. As an instance, melting of ice in a DAC (Fig. 1.10) is inferred from 1. significant broadening and subsequent disappearance of a translational/phonon mode, 2. increase in the frequency

of the O-H stretching modes (A_{1g}, B_{1g}) and reversal in their peak intensities (Ice[103]: 22 GPa, 900 K, Ice[104]: 56 GPa, 1400 K).

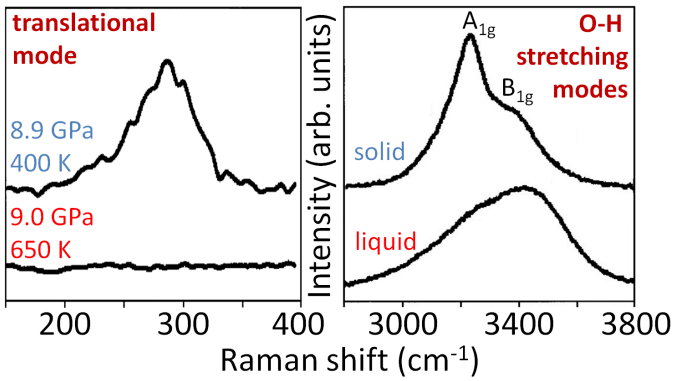

Figure 1.10: **Detecting ice melting in the LHDAC using Raman scattering.** See text for description. Figures adapted from ref. [103]

However, the following main difficulties in the LHDAC limit the usage of RS for studying melting: 1. Increase in background due to fluorescence from impurities[105] and stress[106] in the diamond, 2. Above 2000 K, incandescent radiation is emitted over a wide spectral range increasing the background[105], Raman signal from metals is too weak to detect due to low penetration depth of < 100 nm[54] for laser excitation wavelengths even at 300 K, 3. The typical acquisition times require the sample to be maintained in the molten state for several seconds/minutes, which may not always be possible (see subsection 1.4.1).

1.3.4 Shock-induced melting[31;107;108]

Other than the static methods discussed so far, melting is achieved by dynamic compression as well. The only method that can create P-T conditions beyond the capabilities of the LHDAC and study melting is the 'shock-compression'. It is extensively used to reach multimegabar pressures and temperatures above 10000 K[31].

A mechanically driven or laser-accelerated flyer (impactor) is made to hit and impart a large amount of energy (shock) in a fraction of a nanosecond to the sample to reach a state of higher density, pressure and temperature. By varying the shock strength and measuring velocities of the shock wave and that of the sample material, a locus of pressure-volume-temperature (usually P-V or P-$density$ (ρ)) states reached by the sample, called Hugoniot, is obtained. The time resolution for such measurements varies from nanoseconds to picoseconds.

Unlike in the static methods, there is no direct control over the temperature in shock-compression as for a given shock-pressure, the density and temperature reached are entirely specific to the material[31]. The temperature, coupled to the P-ρ values, can either be measured by optical pyrometry[109] or calculated using models of thermodynamic state of the sample considering Grüneisen parameter and different contributions to the heat capacity[110]. On a P-T diagram, the shock-melting temperature is the temperature on the Hugoniot corresponding to the pressure at which the discontinuities in the sound velocity or volume are observed. It is also the temperature corresponding to the intersection of the Hugoniot and melting curves calculated using empirical models or theory (e.g. Lindemann melting).

However, there are problems with the accuracy of the melting temperatures obtained in shock-experiments, which will be described in subsection 1.4.1.

1.4 Need for a new method

The melting temperature, being a physical property of a substance, is independent of the method and the criterion used for measuring it.

This is indeed observed experimentally in case of metals like aluminium (Al) (Fig. 1.11) and copper (Cu) (Fig. 1.12). Different static (LHDAC, large volume apparatus) and shock compression methods, and different melt-criteria have produced melting temperatures in an excellent agreement with each other and with theory. An excellent agreement between static and shock measurements also exists for alkali halides (CsI, KCl, KBr[111], LiF, NaCl[85]), silicates ($MgSiO_3$[112]) and silica (SiO_2[113]).

On the other hand, there have been conflicting reports which show very large differences in the slopes of melting curves measured by different available methods. In case of the well known example of iron (Fe) (Fig. 1.13), the maximum discrepancy among melting temperatures measured in the LHDAC using static methods but different criteria (visual observation, XRD, SMS) is about 1000 K at the outer core-mantle boundary (130 GPa) of the Earth. Similarly, at the depth of the inner core boundary (330 GPa), the extrapolated melting temperature from a static method[121]

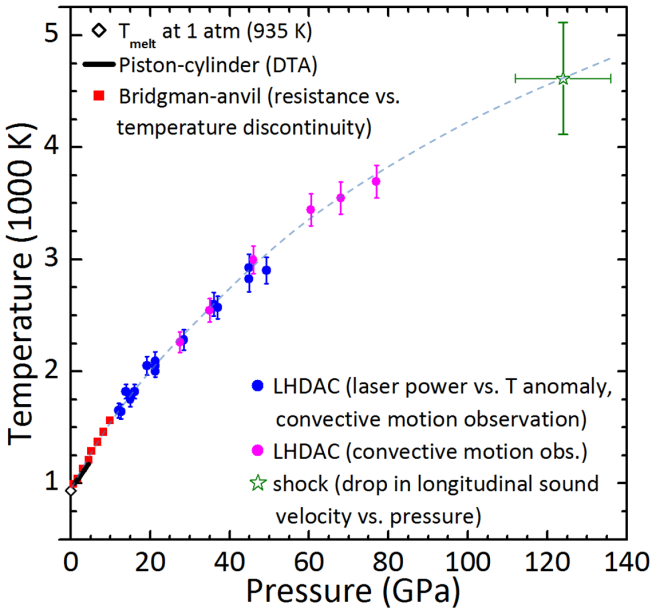

Figure 1.11: **Agreement of melting data on aluminium using different methods and criteria.** References for data: ▬ Jayaraman *et al.* (1963)[114], ■ Errandonea *et al.* (2010)[115], ● Hänström *et al.* (2010)[116], ● Boehler *et al.* (1997)[117], ☆ Shaner *et al.* (1984)[110]. The dashed curve is a guide to an eye.

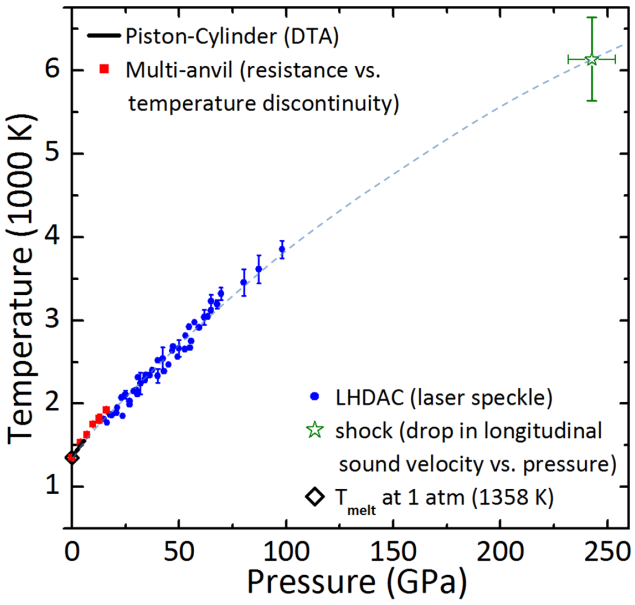

Figure 1.12: **Agreement of melting data on copper using different methods and criteria.** References for data: ▬ Akella *et al.* (1971)[118], ■ Brand *et al.* (2006)[119], ● Japel *et al.* (2005)[81], ☆ Hayes *et al.* (2000)[120]. The dashed curve is a guide to an eye.

differs from the shock data[122] by as much as 2000 K. Such serious discrepancies are hard to reconcile, and in effect, hamper the calculation of depth dependence of viscosities of iron and its compounds, resulting in an inaccurate picture of the Earth's interior[5].

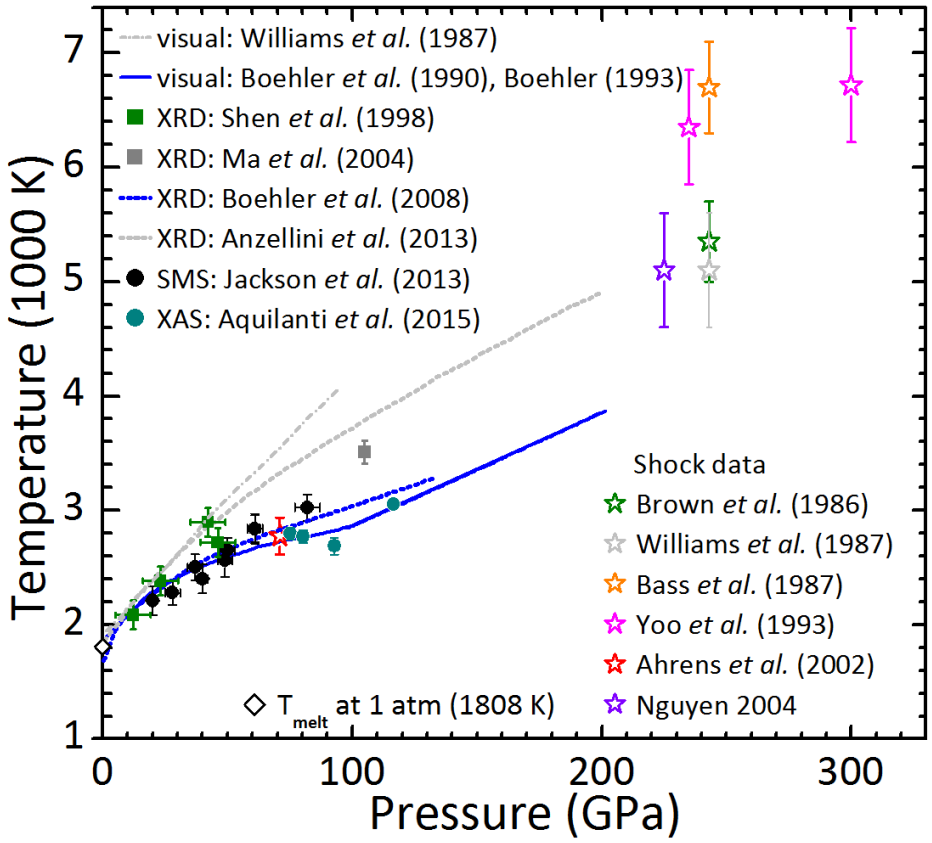

Figure 1.13: **Melting data on iron using different methods and criteria.** The static data are from LHDAC experiments. References for data: :[123], :[75;121], :[90], :[124], :[125], :[126], :[62], :[63], :[127], :[123], :[128], :[129], :[122], :[130].

Another example is that of the refractory transition metals, which are extensively used in manufacturing components of machineries operated in harsh temperatures and stress. Their melting behaviour under high pressure is of interest as the strength of materials and their melting temperatures are correlated. Melting temperatures of metals, that melt from the bcc structure (Ti, V, Cr, Mo, Ta and W), measured in the LHDAC show flat melting slopes[79] ($\mathrm{d}T/\mathrm{d}P \to 0$) at high pressures. In contrast, the shock measurements and computational models report very steep melting slopes. Tantalum (Ta) presents an extreme case, where the melting temperatures measured by two static LHDAC methods, both XRD, differ

by about 2000 K at 125 GPa. Also, the shock data are higher than the extrapolated flat melting curve by 6000 K at 300 GPa. The discrepancies in case of Ta are discussed in detail in chapter 3 with Fig. 3.1 and Fig. 3.2.

Since these discrepancies cannot be accommodated within the experimental uncertainties by applying corrections, e.g. wavelength dependence of emissivity, or by a physical phenomena like solid-solid phase transition, there is a need to closely investigate and remedy the difficulties associated with the experimental approaches in the LHDAC.

1.4.1 Difficulties in studying melting in the LHDAC

Despite many technological advances in the field of high pressure research, the experimental detection of solid - liquid transition and accurately measuring temperature at the onset of the transition has remained a challenging task due to several difficulties.

An ideal way to measure the melting temperature in the LHDAC is to have the molten portion confined long enough in a stable way for measuring the temperature, and simultaneously characterising the melt using an *in-situ* probe, e.g. ADXRD. It allows experimental determination of the radial distribution function or the structure factor of the sample to clearly distinguish its solid and liquid states.

However, when using a CW heating laser, a few seconds of heating near the melting temperature often causes sample instability, dispersion of the melt in the surrounding medium, an uncontrollable absorption of the laser radiation with sudden rise in temperature (thermal runaway), and chemical reactions of the sample with the medium or diamond.

Such generic difficulties in detecting melting and related sources of uncertainties in the temperature measurement are discussed using routine probes and criteria as follows.

Using X-rays

The schematics of double sided laser-heating in a DAC are shown in Fig. 1.14. The sample is typically a piece of foil or a flat chunk or a pellet of compressed powder in shape of a disc that is confined to the sample-chamber in an inert pressure transmitting medium. In the figure, a cross-section of such a disc (horizontal grey rectangle) is shown for clarity.

It is being heated from the top and the bottom with an infrared laser (red shapes). The thermal emission is collected from the centre of the hot spot (yellow cones) while probing with X-rays (vertical grey column). The dimensions shown are typical.

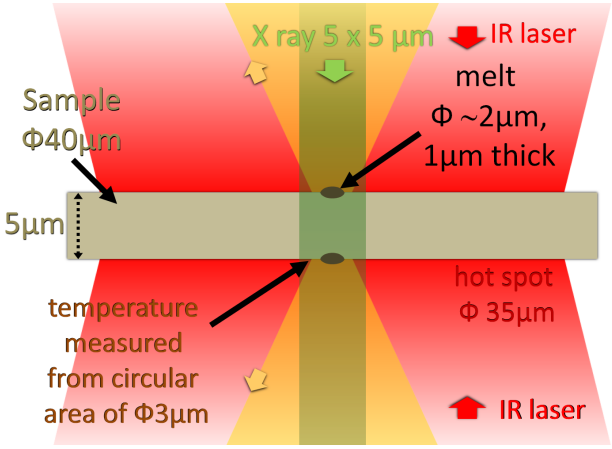

Figure 1.14: **Schematics of double sided laser heating.**
See text for the description.

When using a heating laser with a Gaussian profile, melting is initiated in the central area within the hot spot where the temperature is the highest. To measure temperatures accurately, the optics that collect incandescent light from the sample have to be perfectly aligned with this centre. A few micrometres of misalignment can result in a temperature difference of a few hundreds of degrees between the measured and the real melting temperatures[5]. Additionally, the X-ray beam must be aligned with the centre of the hot spot to obtain the maximum scattering signal from the melt and ideally, it should be completely contained within the lateral extent of the melt.

When using prolonged CW laser-heating, the collecting optics, the hot spot centre, and the X-ray beam need to remain perfectly aligned all the time during melting of the sample. This alignment is not always guaranteed to be maintained at the synchrotron X-ray sources due to long optical paths for the incident lasers and emitted thermal signals. There are four possibilities which can result in an erroneous temperature measurement of the onset of melting (T_{melt}) when the melt volume is small.

1. The hot spot centre is aligned with the X-rays but not with the optics ⇒ the thermal radiation is collected from a spot away from the hot spot centre i.e. from a cooler region, while XRD indicates melting ⇒ T_{melt} is underestimated.

2. The hot spot centre is aligned with the optics but not with the X-rays ⇒ X-rays sample a solid portion even when melting is initiated ⇒ T_{melt} is overestimated.

3. The X-rays and the optics are aligned with a spot away from the hot spot centre ⇒ X-rays sample a solid portion even when melting is initiated ⇒ T_{melt} overestimated.

4. The X-rays, the optics, and the hot spot centre are not aligned with each other ⇒ X-rays sample a solid portion even when melting is initiated ⇒ T_{melt} is overestimated.

Even when the solid sample is well confined and well aligned, one may overestimate the melting temperatures as follows. For the XRD measurements in the double sided LHDAC, the accepted melting criterion is an appearance of a diffuse scattered ring and/or spots due to fast recrystallisation[93;131]. At the onset of melting, the melt is initiated at the hottest portion of the heated area on the sample, which is typically a few micrometres in diameter. A rough estimate of the volume of such a molten portion compared to the solid portion within a typical synchrotron X-ray beam turns out to be less than 10% (Fig. 1.14). The increase in the background due to the diffuse scattering signal from this tiny liquid portion in presence of the Bragg peak from the solid portion (> 90%) is extremely weak to be measurable using the standard X-ray CCD detectors or image plates. Only with a further increase in temperature, when the liquid to solid ratio is large enough to constitute a measurable XRD signal, the accepted melting criterion of the appearence of a diffuse scattered ring is likely to be satisfied.

In addition, a standard X-ray CCD requires a few seconds of exposure time to collect enough signal to detect melting[93]. If the melt is not contained well, it quickly disperses into the pressure medium and creates a hole ('hole burning')[132] in the sample leading to a reduction in the scattered intensity of the Bragg peaks. In the integrated pattern this intensity reduction may be wrongly attributed to melting if the sample is not carefully inspected after heating. In such an event, the temperature measured over a few seconds would have a little contribution from

the melt before it dispersed. Also, for reactive samples a few seconds of heating can favour a chemical reaction with the surrounding medium[131]. Even the computer controlled incremental heating and fast XRD techniques have failed to prevent such chemical reactions[131] as the heating durations per X-ray exposure could not be reduced below a few seconds.

In the Synchrotron Mössbauer Spectroscopy technique, discussed earlier, the 'hole burning' causes an abrupt change in the signal collected and can be distinguished from melting[62] without inspecting the sample. Hence, this difficulty can be taken care of, if it could not be avoided.

Such difficulties associated with prolonged heating are encountered irrespective of the probe used and hence are common to most methods described earlier. These can be avoided or minimised by reducing the heating time, which however, is limited by the exposure time required for the CCD detector for measuring temperature. The exposure time varies typically from a few milliseconds to seconds, depending on the intensity of the thermal emission from the sample loaded in the DAC. Pulsed laser-heating with nanoseconds of pulse-width has been used with synchronised gated CCD detectors for fast measurement of temperature[133;134]. The temperature must be measured when the sample is in a thermal steady state. In pulsed-heating, during a single pulse, this state may not last long enough to produce enough photons for a reliable Planck-fit. Therefore, the photons are accumulated through multiple heating events at the same location on the sample. This process may damage the sample as the peak temperatures reached in a single pulse can be quite high. Morever, such peak temepratures are difficult to assess[135].

Using visual observation

Two techniques that avoid the problem of detecting a small amount of melt in presence of a large unmolten solid portion are the speckle method and the melt-quench method discussed earlier. Both use single sided laser-heating and rely on the visual detection of melting by means of textural changes in the sample. These experiments are simpler to carry out compared to the other techniques. In the former method, convective motion of the melt is detected by monitoring continuous movement of the laser speckle pattern[77] (Fig. 1.3) reflected from the surface of the sample. In the latter, the texture on the surface quenched from different temperatures to ambient conditions is monitored and an appearance of a shiny crater indicates melting[8;65;79] (Fig. 1.5).

However, as the pressure increases, due to increased stiffness of the pressure medium surrounding the melt, detecting a minute change in the speckle pattern at the onset of melting becomes difficult. In addition, the change in speckle pattern could originate from the textural changes due to chemical reactions or due to melting of the pressure medium locally. One needs to rule out these possibilities by choosing an appropriate pressure medium to unambiguously infer melting of the sample. In both, the 'speckle' and the 'melt-quench' methods, to track any presence of chemical reactions, complementary *in-situ* probes like Raman spectroscopy, or *ex-situ* chemical analysis (EDS) on the recovered sample must be employed. Moreover, a precise control over the laser power is required while monitoring the textural changes to avoid overestimation of melting temperatures.

While the static methods have difficulties due to prolonged heating, the dynamic methods / shock-induced melting have difficulties mainly due to short timescales.

Melting temperatures from shock-induced melting
With the shock technique described in subsection 1.3.4, the pressure and the density along a Hugoniot can be accurately measured[5]. However, the following problems occur in obtaining the melting temperature:

1. In the direct (pyrometric) measurements of temperature, the thermal emission from the shocked sample, measured through an optical window, gets distorted due to changing optical and thermal properties of the window material[31]. Due to insufficient data on the relevant properties e.g. thermal conductivity and emissivity at the extreme P-T conditions, their complex time dependent behaviour is difficult to calculate. The corrections required in such melting temperatures are higher than 500 K (e.g. iron[129], steel[136]).

2. Temperatures estimated from theoretical models considering different contributions to the heat capacity show an uncertainty of typically ±500 K (e.g. Ta[137], Fe[127;138]) that is too large compared to the errors in the static measurements.

3. With the heating rates of 10^9-10^{13} K/s, the temperature may rise faster than the rate required to melt the material[139]. It causes superheating of the sample, resulting in a melting behaviour distinct from the equilibrium melting[140]. Therefore, while interpreting the shock-induced

melting, the effects of superheating need to be considered. For example, for a heating rate of 10^{12} K/s, the maximum superheating predicted by theory is as high as 0.43 times the melting temperature[141].

In view of the difficulties discussed in measuring melting temperatures in the static LHDAC methods and in shock-experiments, a need for a new method emerges that can overcome the limitations of the prolonged heating using CW lasers and the shortcomings of too short heating durations in the pulsed-heating or the shock-compression techniques.

1.4.2 Conclusion

The ultimate aim of measuring the melting temperature in the LHDAC is to be able to confine the melted portion of the sample in a stable way and long enough for characterising the melt using the *in-situ* probes.

Until such a technique arrives, new experimental methods need to be explored that will circumvent the difficulties in detecting an onset of melting, avoid chemical reactions, provide deeper insight into the structural changes during melting and bridge the large gap in the timescales between static and shock experiments by a drastic reduction in the heating duration in the LHDAC.

The following chapters describe the development of a new 'flash-heating' method that allows to accurately detect an onset of melting and measure the melting temperature of a substance subjected to pressures from ambient to near megabar, while avoiding most of the previous difficulties.

——o——

Chapter 2

Development of the flash-heating method

2.1 Primary CW laser-heating set up

The basic apparatus used in this work for single sided CW laser-heating in the DAC and temperature measurement is shown in Fig. 2.1. It will be developed further to incorporate flash-heating. Specifications of the components are listed in the legend.

The DAC routinely used in the experiments is a plate type[60] cell (Appendix A) tightly clamped in a water-cooled copper holder, which is mounted on a manually operated x-y-z micrometre stage. A tight mechanical contact with copper maintains the DAC near room temperature. Radiation from an ytterbium fibre laser is incident on the sample loaded in the DAC using a laser mirror (m1) and focussed by an achromat (ac1). A dc-motorised stage (ORIEL) moves ac1 along its optic axis to control the size of the hot spot on the sample. The hot spot can be moved across the sample chamber by adjusting m1, mounted on a piezo-actuated stage (LINOS) having sub-micrometre resolution.

The laser requires no cooling. A manually or computer operated dc power supply controls its power with milliwatt resolution. It is operated in the TEM_{00} mode to produce a nearly ideal Gaussian beam profile ($M^2 \approx 1.1$)[§], that simplifies the hot spot alignment for measuring temperatures.

[§] Beam quality factor M^2 = Ratio of an actual beam divergence to the ideal Gaussian beam divergence, both having the same location and radius of waist.

Optics and filters: For an accurate temperature measurement, a crucial requirement is to minimise chromatic aberration in optics (collection optics) that collects thermal radiation from the sample. Standard achromatic lenses can introduce an error as large as 1000 K[142], depending on the size of a hot spot. On the other hand, the aberration-free reflective objectives (Schwarzschild objectives) that are commercially available are difficult to accommodate in the geometry of the laser-heating set up. The customised objectives often lack the optical resolution required for imaging. To circumvent these problems, a pair of standard achromats (ac2, ac3) is used and its numerical aperture is reduced with an iris to an extent where the effect of chromatic aberration becomes insignificant, yet allowing enough resolution for optical imaging. The iris is typically re-

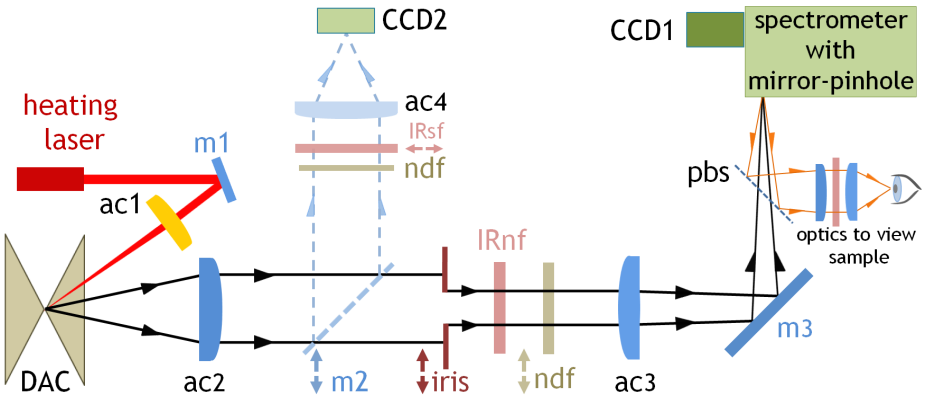

Figure 2.1: **Schematics of a single sided CW laser-heating set up.** heating laser: Ytterbium fibre laser (λ=1070 nm, TEM_{00}, 110 W, IPG Laser GmbH). m1: mirror for laser radiation. ac1: IR achromat (ϕ25 mm, f100 mm). DAC: depicts the diamond anvils of the DAC. ac2: achromat (ϕ10 mm, f25 mm). m2: insertable mirror. iris: insertable, ϕ3 mm. IRnf: Notch filter (1064 nm). ndf: insertable neutral density filters (coloured glass, Schott, optical density 1). ac3, ac4: achromats (ϕ25 mm, f300 mm). m3: optical mirror. pbs: pellicle beamsplitter (THORLABS BP108), 8:92 (R:T). Mirror-pinhole: ϕ35 µm. Spectrometer: SpectraPro 2156, f150 mm. CCD1: PIXIS 100-BR, Princeton Instruments. IRsf: short pass IR filter (Schott, KG3). CCD2: viewing CCD (Hitachi KP-FD 32F-S3). The double headed dashed arrows indicate insertion and removal of components. See text for more description.

moved for better viewing of the sample. It is inserted while aligning the hot spot with a mirror-pinhole at the entrance of the spectrometer and while measuring temperatures.

The standard spectrometers have entrance slits that collect thermal emission from a rectangular area on the circular hot spot. This rectangular area samples unwanted contributions to the spectral intensity, due to which the measured temperatures need large corrections [8;123]. To remedy it, the slits are replaced with a mirror-pinhole to collect the emission from a circular area. This pinhole is a disk of steel or tungsten carbide polished to mirror quality, with a hole drilled into it. Aluminium is sputtered onto it for better reflectivity. A pellicle beamsplitter (pbs) passes the hot spot image to the mirror-pinhole and sends the image reflected from the mirror-pinhole unit to the viewing-optics that includes infrared filters for safely observing with a naked eye. This way, both, the hot spot and the pinhole are viewed simultaneously (Fig. 2.2 a), allowing an accurate alignment for a straightforward temperature measurement.

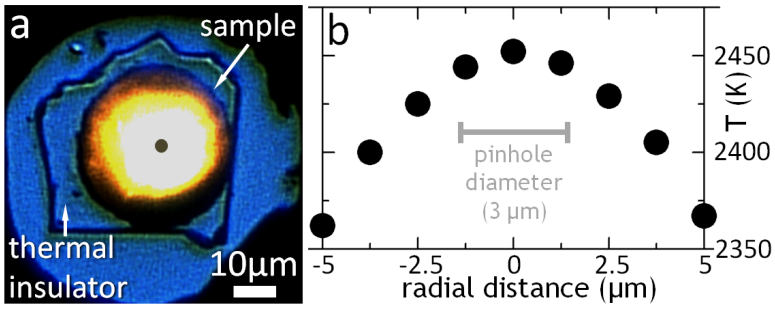

Figure 2.2: **Laser hot spot and the corresponding temperature gradient.** a: CCD image of a laser-heated sample in the DAC as viewed through the optics for sample viewing shown in Fig. 2.1. A hot spot created on the sample (disc) is aligned with the image of the mirror-pinhole projected at its centre (black spot, 3-4 µm dia.). b: Temperature measured along the diameter of a hot spot. This temperature profile dictates the size of the hot spot needed to reduce temperature variation to < 10 K within the central 3-4 µm for accurate temperature measurements.

The focal lengths of the achromats are chosen to magnify the sample image about 12 times and project it onto the mirror-pinhole of diameter 35 µm. This allows to collect thermal radiation from a circular area about 3-4 µm in diameter within the hot spot on the sample (Fig. 2.2 a).

The infrared notch filter (IRnf) blocks the laser wavelength. Neutral density filters (ndf) of appropriate transmission efficiency (30-10-5%) are introduced only to prevent saturation of the signal (counts > 70000) in the CCD detector (CCD1).

Spectrometer and CCD

The spectrometer used has a focal length of 150 mm, a 300 lines/mm grating (500 nm blaze) and a 25.4 mm wide CCD chip mounted to collect spectra over a range of 500 nm, typically from 425 nm to 925 nm (Fig. 2.3). The CCD1 is a Peltier-cooled silicon array detector (H×V : 1340×100 pixel) with which, temperatures are measured most reliably at wavelengths below the laser excitation wavelength. Above this wavelength in the IR region, a nonlinear wavelength dependence of sample emissivity, and Raman effect due to the laser radiation contribute to emission spectra complicating the temperature measurement[64]. With CCD1, a back illuminated, deep depletion detector temperatures can be measured down to 650 K[86] within a few seconds and above 1100 K within a second, for the optics described earlier.

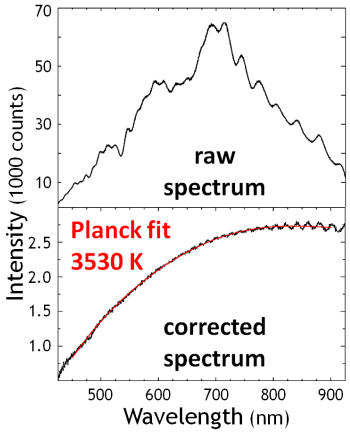

Figure 2.3: **Spectrum for temperature measurement.**

Alignment for measuring temperatures

First, the laser is operated in the CW mode at 1-3 mW of power, mirror m2 is inserted and the IR short pass filter (IRsf) is removed to view the image in the CCD (CCD2). The sample and the laser spot are brought in view by adjusting the DAC stage and the laser mirror m1, respectively. The laser is focussed for a better alignment with the desired location on the sample. Next, the IRsf is inserted, laser is defocussed by moving the laser achromat towards the sample and the laser power is gradually increased until the hot spot is visible at the desired location on the sample. By alternate gradual defocussing and power increment, the hot spot size is made large enough to reduce the temperature gradient over the central portion of the hot spot. For the final alignment, m2 and the iris are retracted. Looking through the optics for viewing the sample, the centre of

the hot spot is aligned with the mirror-pinhole by fine adjustment of the m1 and the DAC stage. For a bright enough hot spot, the iris is inserted and the adjustments are tweaked for a perfect alignment.

Temperature measurement

Temperatures are measured using the 'Spectral Radiometry' method. A hot object emits electromagnetic radiation with a spectrum (intensity vs. wavelength) characteristic of its absolute equilibrium temperature and emissivity[143]. The spectrometer disperses the collected radiation intensity into the wavelength range that is selected considering the sensitivity of the detector. The temperature is calculated by fitting Planck's radiation function (see Appendix B for details) to the measured intensity over the wavelength range, taking into account the emissivity of the sample and the optical transfer function of the set up.

In the set up, a graphical user interface (GUI) (Fig. 2.4) created[64;144] in IGOR PRO (Wavemetrics Inc.) software controls the acquisition, processing and fitting of the spectra emitted from the laser-heated sample.

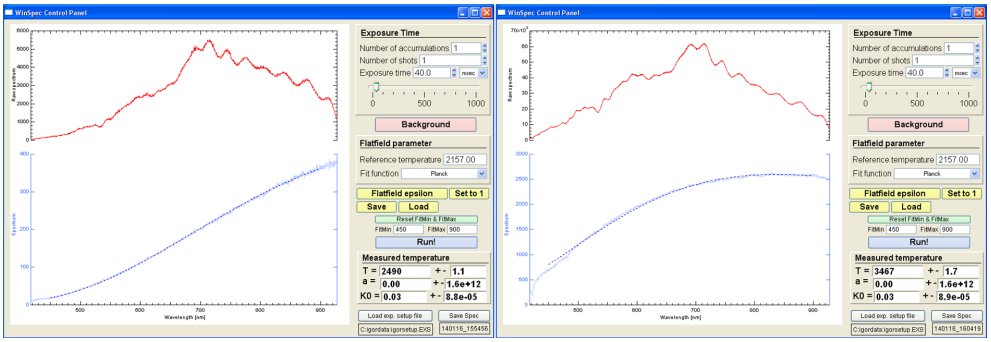

Figure 2.4: **A GUI to collect spectra and measure temperature**
Two examples of temperature measurement (2490 K, 3467 K) using a GUI. The set up optics is calibrated using a tungsten calibration lamp at a reference temperature of 2157 K. The 'Flatfield epsilon' calculates the flatfield (optical transfer function) using the calibration spectrum. Before measuring temperatures using an optical set up, the flatfield specific to that set up is loaded. 'FitMin', 'FitMax' decide the wavelength (nm) range for fitting Planck's function. Raw spectra (red) accumulated in 40 ms are corrected (light blue) and fitted with Planck's equation (dashed blue) in the range (450–900) nm. The CCD gets saturated at 70000 counts.

The GUI runs 'Visual Basic' scripts to communicate with the WinX/32 WINSPEC (Roper Scientific) software that controls the CCD detector and the shutter of the spectrometer. The GUI action for spectra collection, data processing, and temperature extraction is summarised as follows.
1. Capture a background spectrum with the spectrometer-shutter closed.
2. Subtract it from the spectra acquired with the shutter open.
3. Collect a spectrum ($C_{T_{ref}}$) from a calibration lamp at a known temperature (T_{ref}) using the optics to be used later for the laser-heating experiment (step 6).
4. Calculate theoretical Planck spectrum ($P_{T_{ref}}$) at T_{ref}.
5. Calculate 'optical transfer function' or 'flat-field' as $C_{T_{ref}}$ /$P_{T_{ref}}$.
6. Collect a spectrum (S_{RAW_T}) from a laser-heated sample using the optics set up (refer to Fig. 2.3 for steps 6, 7, and 8).
7. Calculate the corrected spectrum (S_{CORR_T}) as S_{RAW_T} / flat-field.
8. Fit Planck's equation to S_{CORR_T} using the Levenberg-Marquardt nonlinear least square method to extract the temperature T.

A temperature thus measured is precise within ±5 K. Compounding the errors from calibration, fitting, and dispersion of thermal radiation due to diamond, a temperature reported is accurate within ±20 K. For a discussion on accuracy and systematic errors due to emissivity, see Appendix B.

2.2 Development of the flash-heating set up

As discussed in the subsection 1.4.1, to circumvent the difficulties arising from too long or too short heating durations in the LHDAC experiments while measuring temperatures, the primary CW laser-heating set up was modified for controlled heating in the milliseconds timescale as shown in Fig. 2.5.

The power of the heating laser was modulated by a function generator (Toellner, TOE 7404) producing a pulse-train at 4 Hz with 20 ms pulse duration. This duration must fulfill 4 essential needs for a successful flash-heating measurement. It should be 1. short enough to avoid chemical reactions of the sample with the pressure medium or the anvils, 2. short enough to avoid a thermal 'run away' (uncontrollable rise in temperature), 3. long enough to reach a thermal steady state, and 4. long enough to provide a sufficient photon-count for temperature measure-

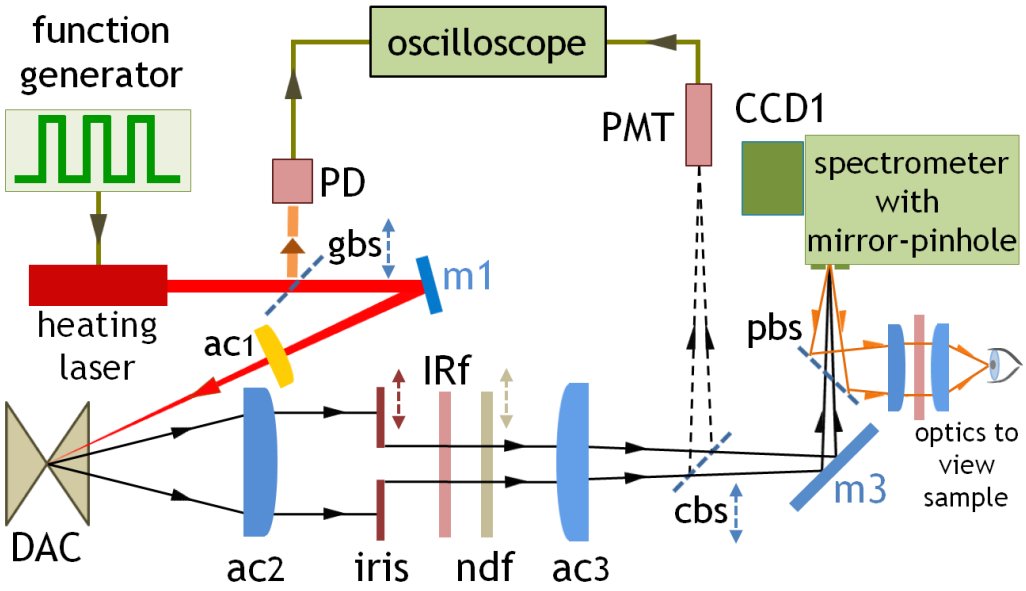

Figure 2.5: **Schematics of the optical set up for flash-heating in a DAC.** A function generator triggers the heating laser to produce a 20 ms rectangular laser pulse. A laser photodiode (PD) and a photomultiplier (PMT) measure the laser emission and the corresponding thermal response from the sample, respectively, as monitored in an oscilloscope (Fig. 2.6). Iris reduces the numerical aperture of the achromat ac2 to minimise the chromatic aberration. Mirror m2 retractable from the optical path from ac2 to iris, and the optical arrangement with CCD2 shown in Fig. 2.1 are a part of the set up but not displayed here for clarity. Temperature is measured with a CCD - spectrometer by fitting Planck's function in the wavelength range 425-925 nm (Fig. 2.3). gbs: Insertable beam splitter (BK7 glass, 7:93 (R:T)), cbs: Insertable cubical 50-50 beam splitter (THORLABS BS016). For more description and specifications of the elements in this figure see text and the legend of Fig. 2.1

ments. The pulse duration depends on the nature of thermal response from the sample and has to be inferred from trial runs. For the test cases of rhenium (Re) and molybdenum (Mo) discussed in the following sections, 20 ms is found to be optimum. The laser emission and the corresponding thermal response from the sample were measured with a Si-photodiode (PD) (Thorlabs 201/579-7227) and a photomultiplier tube

(PMT) (Hamamatsu H6780-20), respectively. Both have a response time of nanoseconds and were monitored using a digital oscilloscope (Tektronix DPO4032, 350MHz).

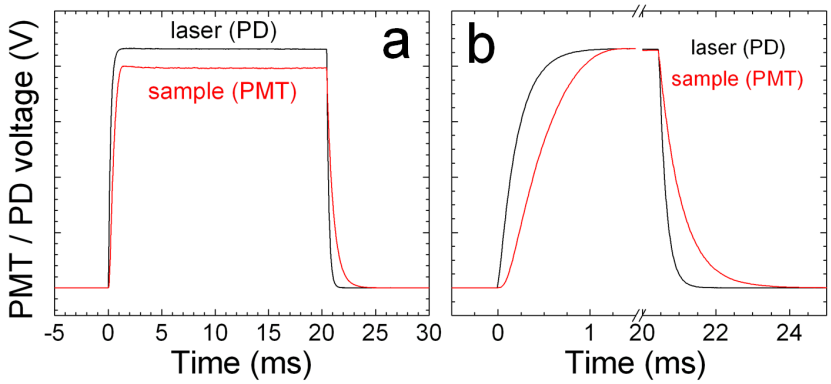

Figure 2.6: **Modulation in laser emission and corresponding thermal response from the sample in a flash-heating event.**
(a) Black curve is the laser emission measured with a Si-photo diode (PD), when the laser power is modulated by a 20 ms rectangular pulse from a function generator. The red curve is the thermal emission from the sample measured with a photomultiplier tube (PMT) during a 20 ms flash-heating event at 3896 K. (b) Expanded view of the rise and fall nature of the laser power and the sample response shown in (a). The voltages are adjusted for clarity. The PMT generates a signal for temperatures $\geq$ 1800 K. The time required for the sample to reach a thermal steady state is $\sim$1 ms. The delay between the laser emission reaching a stable value and the sample reaching the corresponding steady temperature is about 0.5 ms.

Fig. 2.6 shows a flash-heating event at a steady state temperature of 3896 K. The PMT starts generating a detectable signal for temperatures 1800 K and higher. The time required for the sample to reach a thermal steady state from 1800 K to the final temperature of 3896 K is about 1 ms. In a separate test, the rise and fall times were found to be independent of the final temperatures reached in the experiments. The contribution of the lower temperatures during the rise and fall time durations was calculated approximately using $I \propto T^4$ (Stefan-Boltzman Law), where I is the intensity of the incandescent light and T is the absolute temperature. This contribution to the steady state temperature measured is less than 1% and is insignificant compared to the other experimental uncertainties.

In a second test, the pulse duration was changed from 20 to 80 ms in steps at a constant laser power to reach above 3000 K for a fixed hot spot size. The temperatures were found to be within 1% of those measured for 20 ms.

The flash-heating procedure is described in detail with the test cases of refractory metals in subsection 2.3.3.2.

2.3 Rhenium and Molybdenum as test cases

The flash-heating method was tested by accurately reproducing the well established melting points of Re and Mo at 1 atm as described next. Other reasons for chosing these metals are the lack of data on Re melting above 8 GPa and a drastic disagreement in melting temperatures between static, shock and theoretical results for Mo at high pressures.

2.3.1 Rhenium

Among metals, Re has the second highest melting temperature (3453 K)[145], the third highest elastic and shear modulii[145], and the highest strength up to 2275 K among the refractory metals[146]. These properties and its resistance to corrosion make it an important metal in manufacturing of the components in high-temperature, high-stress applications[147–149], such as gas turbine and jet engine blades, electrodes, thermocouples, petroleum catalysis, and reactors. In the high pressure research, Re is a primary material used for gaskets in a DAC. Despite its importance, a little is known about its properties at high P-T conditions[150].

Re crystallises in the hcp structure at ambient conditions and no phase transition has been observed in static compression measurements using Raman spectroscopy to 63 GPa[151], using EDXRD to 216 GPa[152] and shock compression experiments to 279 GPa[153]. Theoretical calculations predict the hcp structure to remain stable to 1 TPa at room temperature[154].

The only high pressure data on melting of Re was obtained to 8 GPa in a belt-type apparatus with optical windows and using electrical heating. Temperatures were measured with the 'three-wavelength pyrometry'[155]. It reported a steep increase (linear slope: 32 K/GPa) in the melting temperature from 3450 K to 3770 K.

2.3.2 Molybdenum

Mo is extensively used in structural and engineering steel for its corrosion resistance and strength, without adding much weight[156]. Due to their ability to sustain high temperatures and stresses, components made from Mo superalloys are indispensable in making turbine blades used in the rocket engines, airplanes and power plants[149;156].

Unlike Re, the behaviour of Mo is well studied (see Fig. 2.7) at extreme conditions of pressure and temperature in shock, DAC and computational investigations.

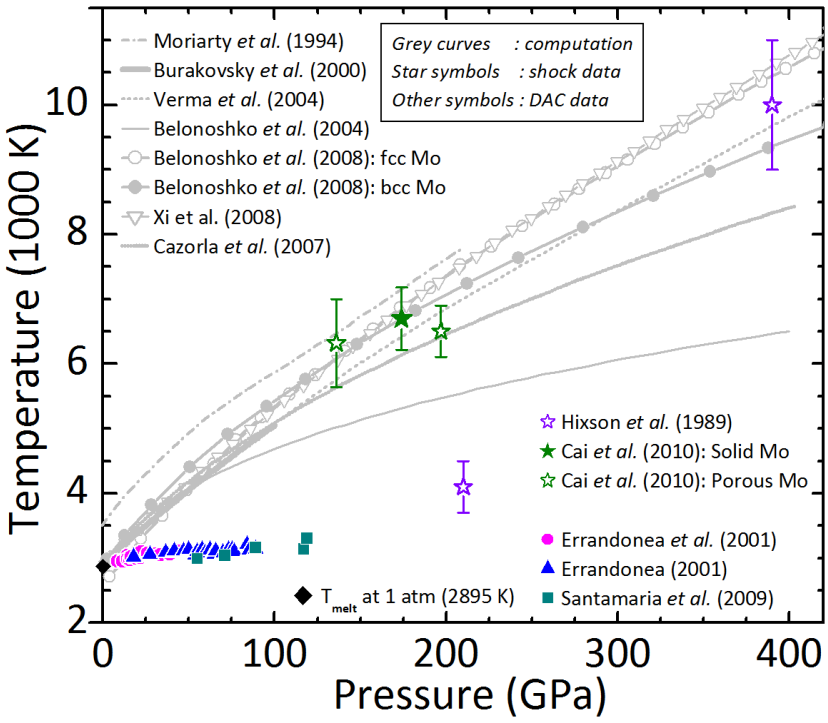

Figure 2.7: **Static and shock data on Mo melting compared with theory.** SHOCK data: (☆[157]): Data at 210 and 390 GPa are interpreted as solid-solid transition and melting, respectively. (☆,★)[158]. STATIC data: 1 atm (◆). Speckle (▲[79]). Quenched texture (●[79]). ADXRD (■[159]). THEORY: MD simulations with multi-ion interatomic potential (—·—·—[160]). Dislocation mediated melting (—[161], - - - -[162], —[163], —▽—[164]). *Ab-initio* MD simulations (—○—, —●—[165]). *Ab-initio* phase coexistence method (·····[166]).

However, the shock-melting measurements[157;158] and numerous calculations[160–167] are in a stark disagreement with the CW LHDAC results[79;159] (Fig. 2.7). At the highest pressure reached in the shock measurements (390 GPa), the extrapolated DAC data is lower by about 6500 K. The computed melting curves vary in their slopes depending on the methods, assumptions, and approximations used for the calculation. Yet, most of these are consistent with the shock data obtained above 120 GPa.

To resolve the discrepancy, the discontinuities in the sound velocity vs. density plot, corresponding to 210 GPa, 4100 K and 390 GPa, 10000 K were linked to 1. phase transition from the ambient bcc phase to hcp or fcc structures and 2. melting from fcc phase, respectively[157;164;165;167–171]. In one report[172], the discontinuities were linked to a phase transition from bcc to icosahedral short range ordered (ISRO) phase and melting from the ISRO phase, respectively. Another study[165] suggested that the reported DAC data represented a phase boundary for a solid-solid transition instead of melting, but so far no such transformations to the hcp or fcc phases have been found in XRD measurements in the DAC up to melting temperatures[159;173–175]. In view of these contrasting reports on melting, Mo was an apt case for applying the flash-heating method.

2.3.3 Experimental

2.3.3.1 Sample preparation and loading

A Re foil (purity 99.9%, Aldrich) was polished, laser cut (Fig. 2.8 a) using a pulsed IR laser (λ: 1064 nm, 100 mW, 6 kHz) and cleaned using acetone / isopropanol to produce disks 50-60 μm in diameter and 8-9 μm thick (Fig. 2.8 b). In case of Mo (purity 99.99%, Aldrich), grains of 5-10 μm diameter were pressed between diamond culets to produce 5-6 μm thick flat disks of nearly circular area having 50-60 μm diameter (Fig. 2.8 c).

For Re, a disk was placed flat on the diamond culet and the cell was loaded with 99.999% purity argon as a pressure transmitting medium, using a gas loader at room temperature and 0.3 GPa. Re gaskets, pre-indented to 35 μm were used in a plate-DAC with conical anvils[60] with culet sizes ranging from 320 to 350 μm. The resulting argon layer, serving as a thermal insulator between the top diamond culet and the sample was about 5-10 μm thick. In some loads, 3-5 μm thick KCl plates were used as a thermal insulator at the bottom of the sample (Fig. 2.9). Similarly, for

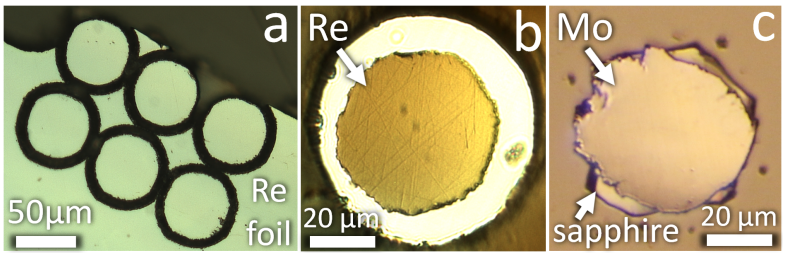

Figure 2.8: **Samples of Re and Mo prepared to load in the DAC.**
a: Laser-cutting of discs from a polished Re foil. b. An isolated, cleaned Re disc placed on a culet and inside a gasket hole. c. Pressed grain of Mo resting on sapphire plate. See text for further description.

the Mo runs, polished 5 µm thick plates of single crystal sapphire were used. Ruby grains, distributed over the anvil surface, were used as the pressure markers (see Appendix C). Pressures measured by the 'ruby flu-

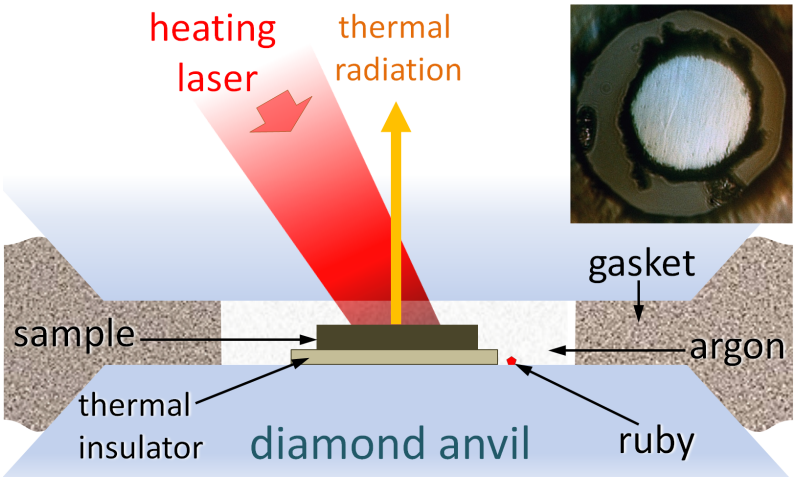

Figure 2.9: **Schematics of a typical laser-heating geometry.**
The sample is a polished laser-cut disc (Re) or a pressed grain (Mo). The thermal insulators at the bottom (sapphire/alkali halide) and at the top (Ar) prevent loss of heat to diamond. Argon serves as an inert, thermally insulating pressure medium. Sample chamber is a hole drilled in a rhenium gasket. Insert is a microphotograph of a polished Re disc (60 µm diameter, 8 µm thick) loaded in argon pressure medium before heating. Ruby serves as a pressure marker.

orescence technique' before and after heating did not differ significantly due to the brief heating events. The thermal pressure is expected to be low due to the small volume ratio of the heated sample portion to surrounding argon with low shear strength[84].

2.3.3.2 Flash-heating procedure

Flash-heating was performed in the following way. First, the laser in CW mode was aligned at an unheated portion of the sample at powers of 1-3 mW using the viewing CCD without IR filters. Then, the power was increased until a hot spot became visible and could be aligned with the mirror-pinhole of the spectrometer (Fig. 2.2). This was typically achieved at about 2000 K, far below the melting temperatures of the refractory metals at 1 atm and not causing any modification of the sample surface. While keeping this alignment, the laser was then defocussed to reduce the temperature variations to less than 100 K across the central area of about 10 μm diameter. Thermal radiation was collected from an area, 3-4 μm in diameter, at the centre of the hot spot.

A command on the GUI (Fig. 2.4) to measure temperature opened the shutter of the spectrometer for 1 second. During this period, no stray light was allowed to enter the spectrometer and the laser was triggered by the function generator to produce a single laser pulse of duration 20 ms, as recorded by the photo diode. The corresponding thermal response was simultaneously recorded by the PMT to ensure that the signal reached a steady state following the laser pulse.

After a flash-heating event, the sample in the DAC was inspected using the collection-optics and the CCD camera, without removing the cell. Another unheated area on the sample was located by adjusting the DAC stage alone, leaving the rest of the alignment untouched for a new flash-heating event at a different temperature. For each new unheated area on the sample, the laser power was increased by about 1 W, producing a temperature increase of about 100 K while ensuring the hot spot alignment with the mirror-pinhole. Typically, one sample disc of diameter 60 μm allowed for 8 - 10 heated spots, while recording both - the temperatures and the respective locations.

The samples were recovered and transferred to a specimen holder for subsequent analysis using SEM and EDS (Appendix D), and the Focused Ion Beam Milling (FIBM) technique (Appendix E).

2.3.4 Analysis and results

2.3.4.1 Experiments at 1 atm

In order to check the accuracy and reproducibility of the flash-heating method to determine melting temperatures, the polished Re and Mo foils were heated at 1 atm, following the flash-heating procedure described earlier. Mo, when heated in air showed high chemical reactivity and sample instability causing unreliable temperature measurements. Heating it in a controlled flow of argon gas avoided this difficulty. Re, unlike Mo, was heated in air as it did not show any chemical reactivity post heating, when checked with the EDS (See Fig. 2.10) .

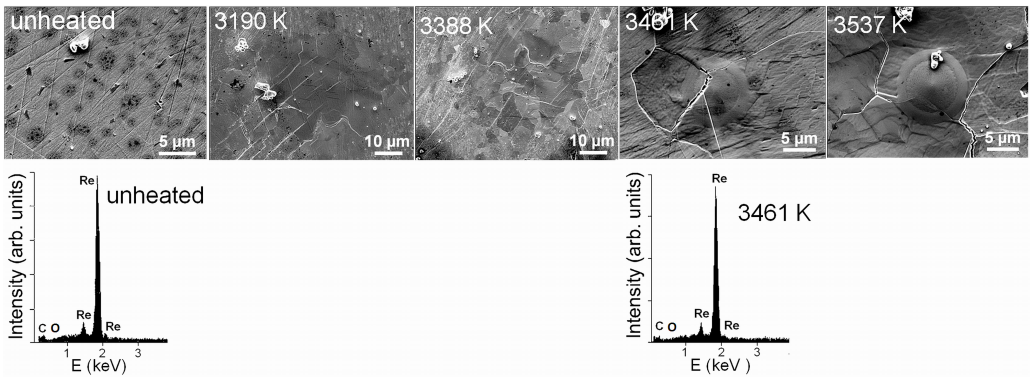

Figure 2.10: **Test of flash-melting at 1 atm on a polished rhenium foil.** Row 1: SEM images of the flash-heated spots on Re at increasing temperatures. A complete restructuring of the surface occurred at and above 3461 K in the form of a round bead-like feature. The known melting temperature of Re at 1 atm is 3453 K. Row 2: EDS spectra collected from an unheated area and the portion heated to 3461 K. When compared, these did not reveal any chemical reaction.

The images of the recovered samples were recorded with SEM (JEOL, JSM). Bead-like, rounded features were clearly and reproducibly observed above the known melting temperature of 3453 K. The EDS spectra were collected from several parts of the heated portions. The EDS performed at 15 keV enabled elemental analysis of material to a depth of about 300 nm for Re and 600 nm for Mo[176]. The instrument JEOL, JSM used has a sensitivity for 0.1-0.2% of oxygen and carbon.

Similar bead formation was observed for Mo above 2870 K, close to the known melting point 2895 K. The observation of reconstruction of the heated portion into a bead-like rounded feature consistent with the known melting points of Re / Mo at 1 atm formed a basis for the criterion of flash-melting, as discussed ahead.

2.3.4.2 Experiments at high pressures

In total, 14 high pressure runs on 14 samples were performed for Re to 47.4 GPa and 4600 K. As an example, Fig. 2.11 shows SEM images of a Re sample recovered from a run at 20 GPa.

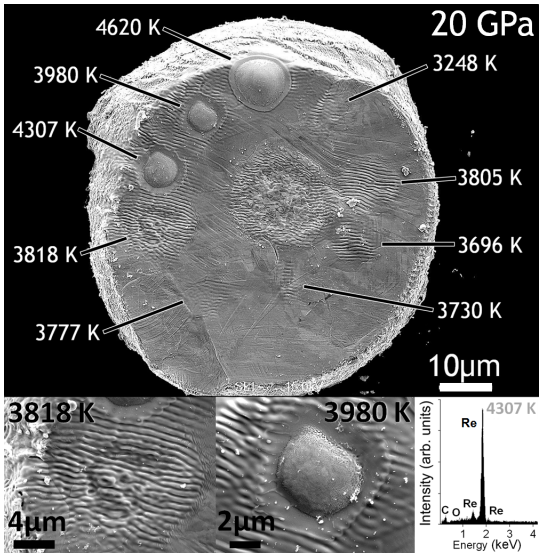

Figure 2.11: **SEM images of flash-heated rhenium disk recovered from 20 GPa.** The laser power was changed for each new heating spot. Drastic textural changes observed at 3818 K and 3980 K correspond to the highest 'solid' and the lowest 'liquid' temperatures, respectively. The wavy patterns follow the direction of incident laser radiation and are likely an effect of temperature quenching. EDS analysis of heated portions indicated no chemical alteration even above melting (4307 K).

The different portions heated at increasing temperatures showed a gradual change in the quenched texture. The first appearance of a round bead-like smooth feature was attributed to melting due to the textural similarities observed at 1 atm. Moreover, at the *P*-*T* conditions of this run at 20 GPa, argon surrounding the heated zone in the sample chamber is already molten [84], offering a relatively free surface to the molten rhenium to extend its volume in the form of a bulge or a crest. At temperatures below melting, the quenched texture still showed the rough features of the solid.

The samples were further analysed for depth profiles of the molten and un-molten portions, using FIBM (Zeiss, Auriga) technique (Fig. 2.12).

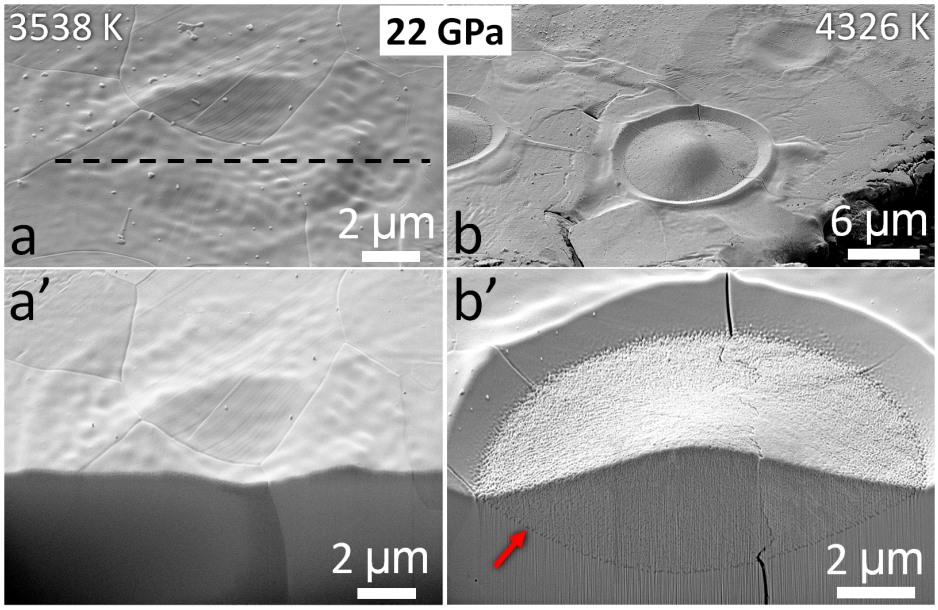

Figure 2.12: **SEM images of flash-heated spots on Re sample recovered from 22 GPa.**
Depth profiles (a', b') were obtained by cutting through the heated portions using the FIBM technique. (a): Spot heated to 3538 K, below melting. (a'): FIB-cut across the dashed line in (a) showing recrystallisation to sub-micrometre depth and no change in textural appearance compared to the unheated portion. (b): Re foil heated to different temperatures at different spots. The spot at the centre was heated to 4326 K, above melting. (b'): FIB-cut of the central spot in (b) shows completely restructured metal with a sharp boundary, several micrometres in depth, between the quenched liquid and the un-molten sample, as indicated by a red arrow.

The top row shows the surface topography of spots heated to 3538 K below melting and to 4326 K above melting. The corresponding depth profiles created using FIBM show contrasting features. While a smooth texture is seen in depth of the un-molten region, the molten portion has a sharp boundary separating the quenched liquid on top and the un-molten solid at the bottom. The extent of the bulge shaped portion in depth as well as above the sample surface is a few micrometres.

Fig. 2.13 shows similar measurements for Mo at 45 GPa. Again, the appearance of smooth bead-like features was attributed to melting due to the similar observations at 1 atm for Mo.

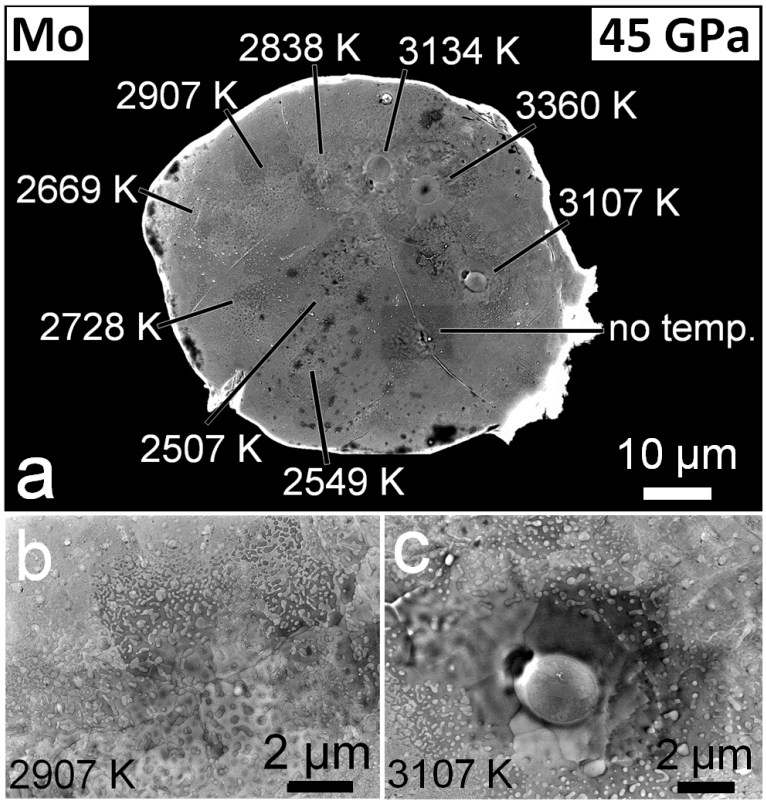

Figure 2.13: **SEM images of flash-heated Mo recovered from 45 GPa.** (a): Spots heated to temperatures below and above melting. (b): A spot heated to 2907 K shows no melt features in contrast to that heated to 3107 K in (c), showing restructuring to a smooth bulge similar in case of Re (Fig. 2.11).

The chemical composition of the unheated and molten portions of the samples were checked routinely using EDS. The analysis yielded the same result before and after heating, indicating no detectable chemical reaction owing to melting.

For each run, the melting temperature is reported as the average of the highest temperature corresponding to a 'solid' observation and the lowest temperature corresponding to a 'liquid' observation. The difference in the two temperatures is the total uncertainty in the melting temperature.

Results for Re and Mo melting are plotted in Fig. 2.14. The melting slope of hcp Re is 3.5 times higher than that for bcc Mo, but is lower than that for the measurements on Re below 10 GPa[155]. Four measurements on Mo yielded melting temperatures in an agreement with the previous

LHDAC reports employing visual observations for melt detection[79] and the ADXRD measurements[159].

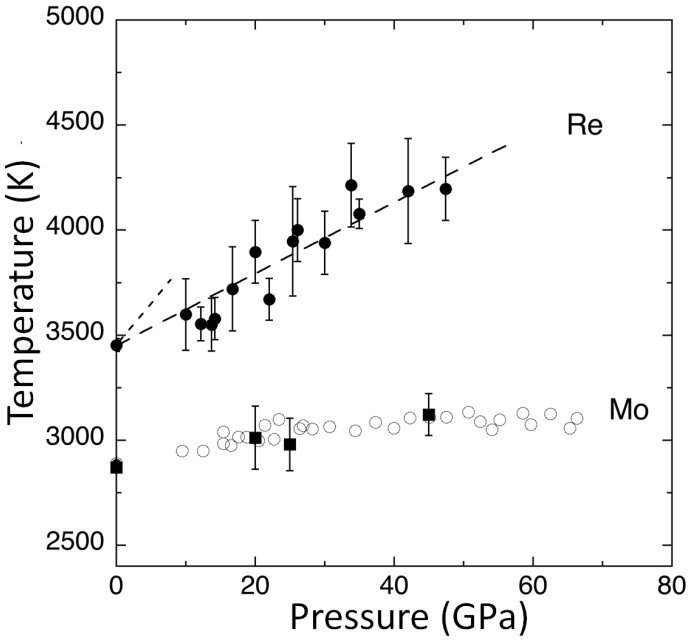

Figure 2.14: **Melting curves of Re and Mo using flash-heating method.** Solid circles and solid squares are the new flash-melting measurements for Re and Mo, respectively. Empty circles represent previous melting data from the LHDAC experiments for Mo by Errandonea *et al.* (2001)[79]. For clarity, the XRD data for Mo by Santamaria *et al.* (2009)[159] consistent with the flat melt slope are omitted here but plotted in Fig. 2.7. The small dashed line represents previous measurements on Re by Vereshchagin *et al.* (1977)[155] using electrical heating in a belt apparatus to 8 GPa. Big dashed line is a guide to an eye for the new data.

The trend that bcc metals generally have melting slopes smaller than the close-packed metals and rare gases was explained[177] as a consequence of the close-packed-like structure of the liquid. Since the packing ratio for bcc (0.68) is lower than that for fcc or hcp (0.74), the volume change upon melting of a bcc solid is expected to be smaller compared to a close-packed solid, thus exhibiting a lower melt-slope. The close-packed nature of liquid Mo and tungsten, which is also a bcc solid, has been confirmed using time resolved ultraviolet photoelectron spectroscopy[178;179].

2.3.5 Summary

The new flash-heating method developed for measuring melting temperatures in the laser-heated diamond cell in well controlled millisecond domain yielded reproducible textural changes below and above melting, while avoiding the notorious difficulties of thermal runaway, sample instability and chemical reactions.

Heating to temperatures close to but below melting only altered the surface to sub-micron levels, whereas melting produced significant structural modifications several micrometres below the surface and a complete restructuring of the surface.

The melting curves of Re and Mo have been measured to 48 GPa, ~4200 K and 45 GPa, ~3100 K, respectively. The extrapolated melting data are in an excellent agreement with the known melting temperatures as well as with those measured by flash-melting, at one atmosphere.

Re (hcp) has a significantly steeper melting slope than bcc Mo. At high pressures, Re becomes the most refractory metal studied, with its melting line crossing that of tungsten at about 20 GPa[79]. Mo melting results support the flat melting curve, a long debated characteristic of the refractory metals with bcc structure.

——o——

Publication based on this chapter:

Flash heating in the diamond cell: Melting curve of rhenium
L. Yang, A. Karandikar and R. Boehler
Review of Scientific Instruments 83, 63905 (2016)
DOI: 10.1063/1.4730595

——o|o——

Chapter 3

Flash-melting of tantalum to 85 GPa

3.1 Introduction

The refractory metal tantalum (Ta) is widely studied by metallurgists to exploit its useful properties at extreme conditions [180–182]. Due to high corrosion resistance, formability, resistance to liquid metals, high conductivity, and favourable alloying nature of tantalum, it is used in cutting-tool industry, in nuclear reactors for fuel-vessels, in crucibles and heat exchangers, in military applications as gun-barrel liners, and in space applications to encapsulate heat sources.

Behaviour of Ta at high P-T conditions is of scientific interest as it is perhaps an extreme case of discrepancies in melt-slopes when comparing not only the computational and experimental reports but also comparing among 1. the simulations using different computational methods and approximations, and 2. the experiments conducted with different melt-criteria, and various methods of melting and temperature measurement.

In Fig. 3.1, data from all the static LHDAC measurements that employed various melt-criteria and spectroscopic measurements of temperature using Planck's function are compared. The fugure also includes the earliest melting study in the Drickamer type piston-cylinder apparatus to 6 GPa, the temperature been measured with the 'two wavelength pyrometry' [185]. The results from CW LHDAC experiments by Errandonea *et al.* using three techniques, namely the laser speckle method to 90 GPa [79], ob-

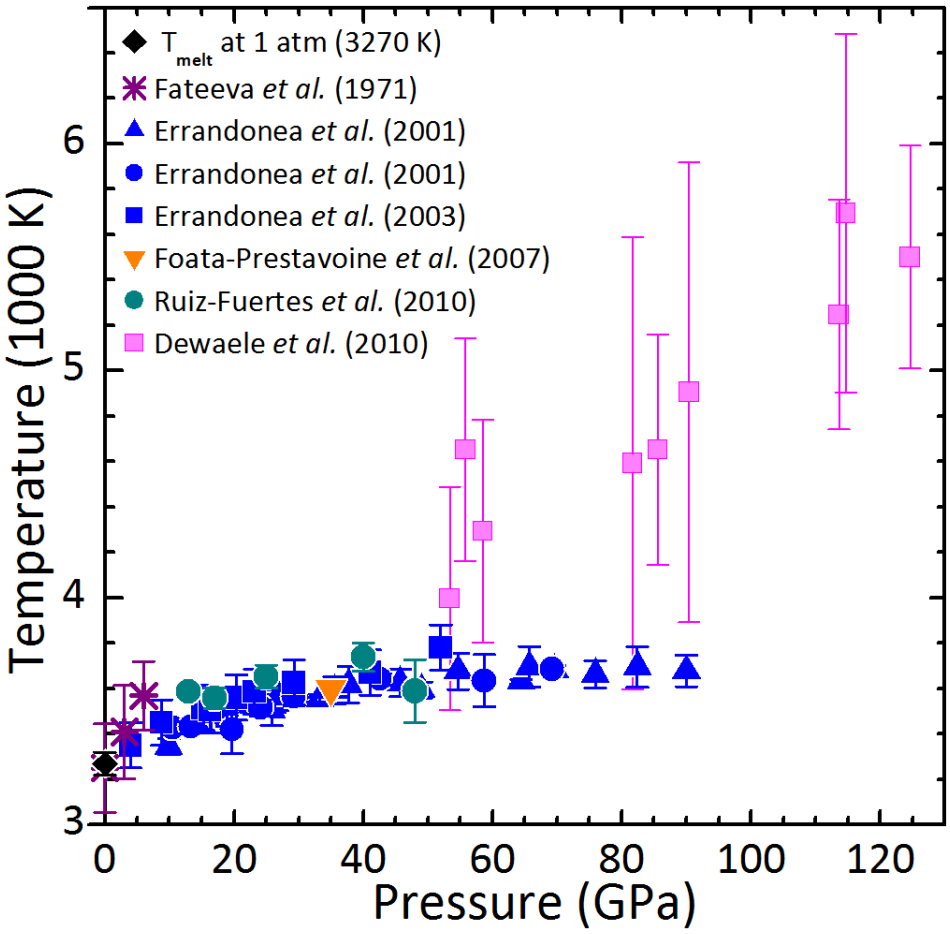

Figure 3.1: **Melting data for Ta from various static methods.** Except the 1 atm data point (◆[183;184]) and the Drickamer piston-cylinder study (✳[185]), all data are from static LHDAC experiments. The symbol-colors represent experimental groups; their shapes represent melt criteria, namely an appearance of a characteristic diffuse ring and/or spots from recrystallisation before melting in the X-ray diffraction (■[186],■[131]), bead formation on samples quenched from high temperature (●[79],●[65]), observing *in-situ* convective motion in the laser-heated spot using visible-laser speckles (▲[79]) and detecting an anomaly in the laser power at melting (▼[132]). The discrepancy between melting temperatures at 125 GPa from the steep and the extrapolated flat melting curves is about 2000 K.

serving modifications in the quenched texture of the heated sample to 69 GPa[79] and synchrotron ADXRD to 52 GPa[186] have consistently produced flat melting slopes ($dT/dP \to 0$). An independent study at 35 GPa[132] reported a discontinuity in the heating-laser power (resulting in a hole in the sample) at a temperature agreeing with the flat slope. In a different approach, Ruiz *et al.*[65] used SEM and optical images to analyse textural differences on recovered Ta samples that were laser-heated at different spots to different temperatures in the DAC. They attributed melting to formation of shiny, bead-like features (Fig. 1.5). Their measurements to 48 GPa agree with the flat melting slope.

However, the recent synchrotron ADXRD measurements in the LH-DAC to 125 GPa[131] reported a relatively steep melting slope, showing a clear discrepancy above 50 GPa with the rest of the measurements. The discrepancy reaches about 2000 K at 125 GPa with respect to the earlier XRD study[186], despite using the same melting criterion.

The early shock induced melting experiments on Ta[137] report a discontinuity in the sound velocity plotted against Hugoniot pressure. The corresponding bounds (7340 K and 10400 K) on the melting temperature were calculated from two Hugoniots considering contributions to heat capacity from the band electrons and from the free electron gas, respectively (Fig. 3.2). More recent optical pyrometry measurements[187] and the simultaneous Hugoniot-temperature measurements[188] reported melting temperatures consistent with this data and also with the steep melting curves calculated from the first principles calculations from ref. [189] and ref. [190], respectively.

Ta melting calculated computationally using the generalised Lindemann law[191], dislocation mediated melting[162;164], vacancy formation enthalpy[190] and *ab-initio* molecular dynamics simulations with different approximations and potentials[132;189;190;192–195] predict steep melting curves but all varying in slope (Fig. 3.2). For instance, the difference in melting points from the two extreme melting slopes is about 2250 K at 125 GPa and about 3950 K at 300 GPa.

To reconcile the flat melting curves measured in the LHDAC with the computational and shock estimates, phase transitions from bcc to other energetically favourable or stable structures before melting were suggested. One study[199] linked the flat melting curve to the presence of frustrated local structures in the liquid. It also inferred a second discontinuity in the longitudinal wave velocity corresponding to melting from

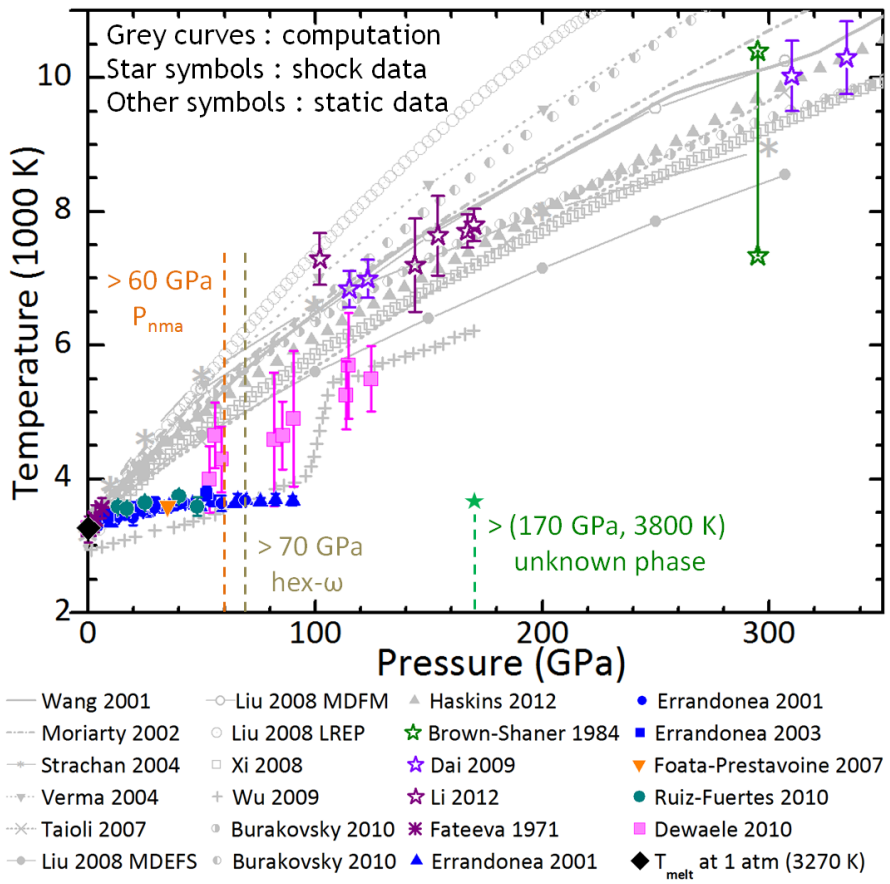

Figure 3.2: **Ta melting curves from static data, shock data, and theory.** For brevity, '*et al.*' is omitted after the first author in above references. *Theory* - generalised Lindemann (—[191]), dislocation mediated (– –▼– –[162]; □[164]), vacancy formation enthalpy (—✱—[190]), quantum atomistic (— · — ·[192]), first principles DFT- GGA-PAW (– –×– –[189]), coexistence phase MD (EFS —●—; FM —○—; LREP ○[193]), *Ab-initio* MD (bcc ◑; hex-ω ◐[194]), DFT MGPT MD (▲[195]). Shear induced plastic phase boundary (+[196]). *Static data* - 1 atm (◆[183;184]), Drickamer piston-cylinder (✱[185]), speckle (▲[79]), bead formation (●[79];●[65]), XRD (■[186];■[131]), laser power anomaly (▼[132]). *Shock data* - T calculated with heat capacity models (☆[137]), T pyrometry (☆[187]), simultaneous Hugoniot-T measurement (☆[188]). Vertical dashed lines indicate predicted phase transition pressures for *Pnma*[197;198], hex-ω[194] and an unknown phase[199].

an unknown phase at around 170 GPa and 3800 K (Fig. 3.2), where the shock Hugoniot[137] would cross the extrapolated flat melting curve.

In another study[196], the flat melting curve represented a phase boundary between the bcc and a shear induced plastic-like phase before reaching the melting temperatures that agreed with the extrapolated shock and XRD measurements. A hexagonal (hex-ω) phase found in the transmission Electron Microscopy (TEM) study on Ta recovered from an explosively shocked state at the peak pressure of 45 GPa and ~550 K[200] was claimed to exist above 70 GPa and at high temperatures[194]. A later study[197] showed the hex-ω to be mechanically and dynamically unstable. It reconfirmed bcc as a stable phase having the lowest enthalpy from 0–1000 GPa and revealed a new orthorhombic *Pnma* structure in 50–1000 GPa having its enthalpy lower than all other candidates viz. fcc, hcp, dhcp, hex-ω, β-Ta and A15. In a supporting study[198], the calculation of shear sound velocity for *Pnma* was found to be in an agreement with the new measurements on shock compressed Ta[201]. Further, at 60 GPa, a kink observed in the longitudinal sound velocity measured as a function of shock pressure and no change in the bulk sound velocity indicated a phase transition. In contrast, in the most recent sound velocity measurement on shock compressed Ta[202] such a kink was absent and it reassured the bcc as the stable phase at those pressures. Moreover, ADXRD measurements in the DAC to 174 GPa[203] at 300 K and to 135 GPa, 5800 K[131] have not reported any phase other than bcc. All these studies with conflicting results underline the complexity in studying Ta melting and obtaining a decisive melting curve.

The only methods for measuring melting temperatures at such high P-T conditions are shock measurements and the LHDAC technique. Problems associated with these techniques are the short time scale and chemical contamination of Ta, respectively. Previous LHDAC studies[65;79] that attributed melting to optical observations of textural changes on the sample surface lacked chemical analysis. Chemical contaminations of Ta during prolonged heating were highly likely in these studies as observed in an earlier study[131] as well as the present work.

The *in-situ* XRD measurements in the LHDAC[131] that reported the only experimentally measured steep melting curve relied on the appearance of a diffuse scattering ring and/or diffraction spots arising from fast recrystallisation[93;131]. The main difficulty in such experiments is to confine and stabilise the melted portion of the sample long enough

to document melting. However, heating durations of even a few seconds near the melting temperature cause sample instabilities and dispersion of melt into the surrounding pressure medium causing large uncertainties in temperature measurements (as discussed in subsection 1.4.1), such as reported in this XRD work. Moreover, the same XRD work reports chemical reactions to be unavoidable with the X-ray acquisitions lasting for a few tens of seconds during CW-heating, in contrast to the earlier XRD study[186] that used the same melt-criterion and reported no chemical reactions.

Since flash-heating of Re and Mo in milliseconds timescale had circumvented the above mentioned difficulties with CW laser-heating, while accurately measuring temperature, Ta was chosen as the next candidate for flash-melting (melting by flash-heating) and extending the analysis further to unambiguously detect the onset of melting. Moreover, the sample preparation and the flash-heating procedure for Ta were appropriately modified to measure its melting to 85 GPa, without any sign of a chemical reaction.

3.2 Experimental

Schematics of the experimental set up used for flash-heating Ta are shown in Fig. 3.3. The set up (Fig. 2.5) used for the Re/Mo melting was improved for an easier synchronisation of the laser modulation and opening of the spectrometer shutter for measuring temperature in a single flash event.

3.2.1 Measurement set-up

A better synchronisation and control over laser-modulation and shutter activity was achieved as follows. A Graphical User Interface (GUI) command for measuring temperature (Fig. 2.4) opened the spectrometer shutter to measure temperature for 40 ms as the exposure time. The shutter controller synchronously triggered a pulse generator (PG) [TENMA - TGP110] which, after a delay of 10 ms, sent a single rectangular pulse of width 20 ms to the laser power controller. An oscilloscope recorded the 20 ms of the laser emission and the corresponding thermal response from the sample, as measured by a photo diode (PD) and a photomultiplier tube (PMT), respectively (Fig. 3.4).

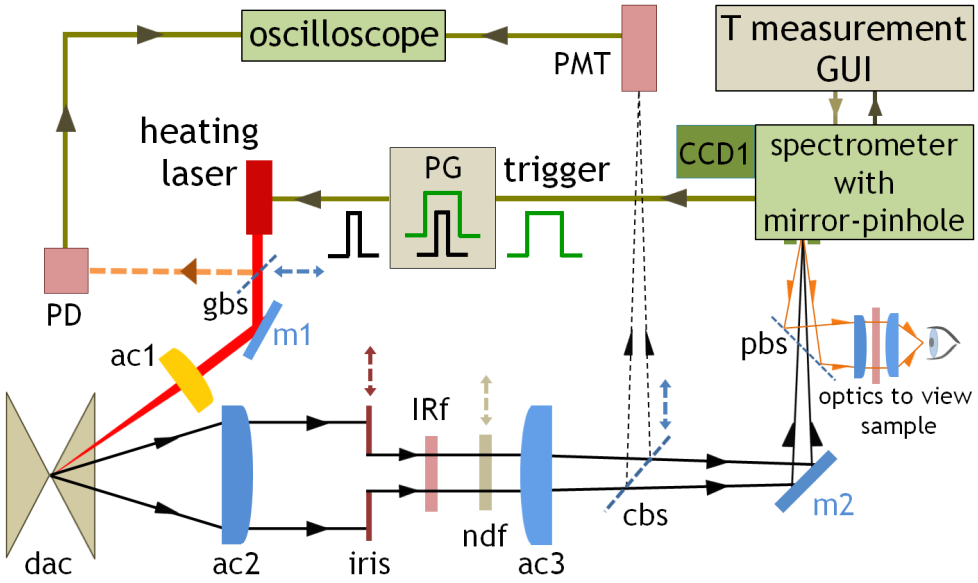

Figure 3.3: **Schematics of experimental set up for single-flash-heating in the LHDAC.**
The components and labels are as described in Fig. 2.5. See text for new additions and further description.

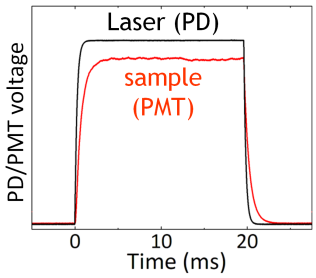

Figure 3.4: **Oscilloscope record of a 20 ms laser pulse and corresponding thermal emission from Ta sample.**

The 20 ms of heating duration, inferred from several trial experiments, was found to be long enough to measure the temperature reliably and short enough to avoid chemical reactions or sample instability. The synchronisation procedure described earlier ensured that the spectrometer recorded thermal emission from the entire 20 ms of the flash-heating event, avoiding any artifact in the spectral intensity arising from the shutter opening and closing activity. The spectral intensity contribution from the rise and fall of the thermal response is less than 1% compared to that of the steady state value[204]. After synchronisation, a hot spot created on the sample was aligned with the mirror-pinhole at the entrance of the spectrometer as described previously (page 40), ex-

cept, due to the extremely reactive nature of Ta, the alignment was done in the flash-mode instead of the CW mode.

3.2.2 Sample preparation

The sample preparation played a significant role in right placement, uniform heating, and an easy recovery of the sample in a successful flash-heating experiment. An ideal sample loading in the DAC required the sample to retain its shape and texture at the desired pressure, and maintain at least 5 μm thick thermal insulation between the sample surface and the facing diamond anvil for efficient heating. The dimensions of samples and sample-chambers were optimised by monitoring their high pressure behaviour in a number of runs. The following techniques of sample preparation were adopted to achieve the desired optimisation.

A. Pressed grain technique: A Ta foil (Alfa Aesar, 99.95% pure) was polished using Al_2O_3 micro-grain sheets. Grains (10-30 μm dia.) scooped from the foil using a tungsten needle were pressed between a pair of diamond anvils to produce about 5 μm thick and 30-50 μm wide samples. However, due to strong adherence of Ta to the diamond surface, such pressed grains were difficult to recover. When recovered intact in a few attempts, carbon contamination was detected in their EDS analysis. On the other hand, pressing Ta grains between anvils made of sapphire or glass produced chemically clean samples but with uneven surfaces. Such samples were found to cause nonuniform heating when laser heated, and hence were discarded. Moreover, the success rate for achieving the right thickness for a given width with a uniform surface was low. Although in general, such a preparation technique enables the quickest loading for many other metals (e.g. Mo, Fe, W), it was not effective for Ta.

B. Laser-cutting: A polished Ta foil (Alfa Aesar 99.95% pure) was cut using a pulsed IR laser (λ: 1064 nm, 100 mW, 6 kHz) to produce disks 25-45 μm in diameter and 5-8 μm thick, as depicted in Fig. 3.5. The recovered discs were cleaned using acetone and isopropanol. These discs were chemically pure as inferred from the EDS analysis (Fig. 3.6 e). For the presence of carbon (C) and oxygen (O) in negligible amounts, see a discussion at the end of the subsubsection 3.3.1 (page 70).

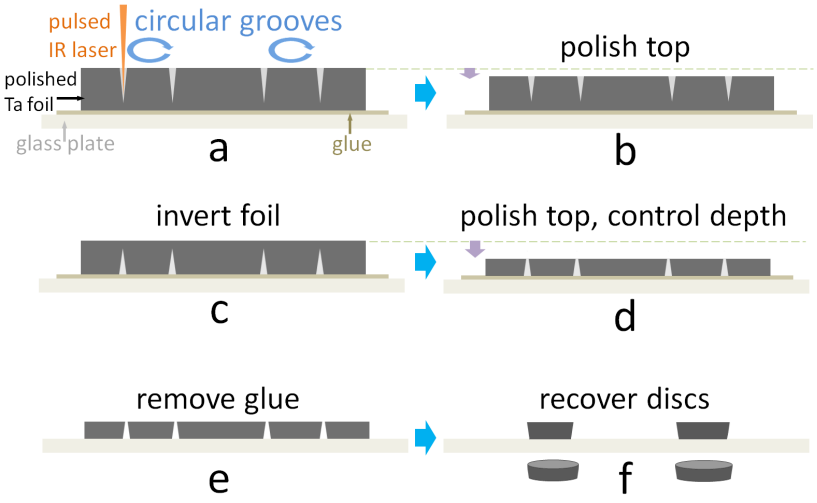

Figure 3.5: **Schematics of laser-cutting procedure to prepare Ta discs.** Procedure : (a) With a pulsed IR laser create circular grooves on a polished Ta foil, with appropriate diameters and having a depth larger than the desired final thickness of the sample. (b) Polish the top to remove dirt and an oxidation layer. (c) Remove the glue, invert the foil and reglue. (d) Polish the foil to reach the final desired thickness. (e) Remove the glue. (f) Separate, recover and clean the discs using acetone and isopropanol.

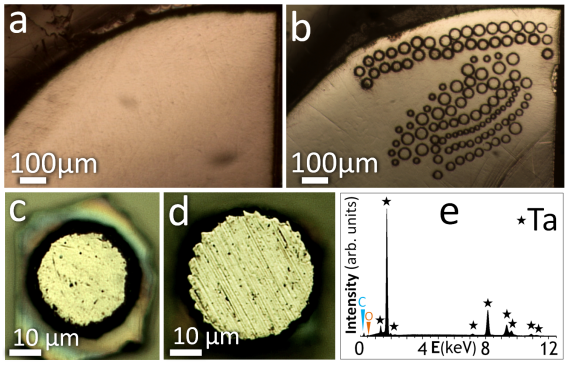

Figure 3.6: **Microphotographs (a-d) of Ta discs in production.** (a) A polished Ta foil (≈50 µm thick) glued to a glass plate. (b) Circular grooves cut in the foil using a pulsed IR laser, as depicted in Fig. 3.5 (b). (c),(d) Recovered and cleaned Ta discs (5-8 µm thick). (e) A representative EDS spectrum of these recovered discs showing the chemical purity of Ta.

C. Focused Ion Beam Milling (FIBM) technique: To ensure the melting data to be independent of sample preparation techniques, melting measurements on Ta bricks produced using the FIBM technique were performed. The procedure was similar to that depicted in Fig. 3.5, except that (i) the focussed ion beam of gallium replaced the pulsed IR laser, (ii) the foil was mounted on a metallic holder using an electrically conductive glue in step (a), and (iii) a brick-shaped sample was preferred over a circular disc due to a technical convenience (Fig. 3.7).

Although the milling process allows the best control over the sample dimensions with the least structural damage, it is at least 10 times slower than the laser cutting.

Therefore, the Ta discs prepared by the laser-cutting technique were used for measuring the melting curve reported in this work. Supporting melting measurements were carried out on the Ta bricks prepared using FIBM (see subsubsection 3.3.2.4).

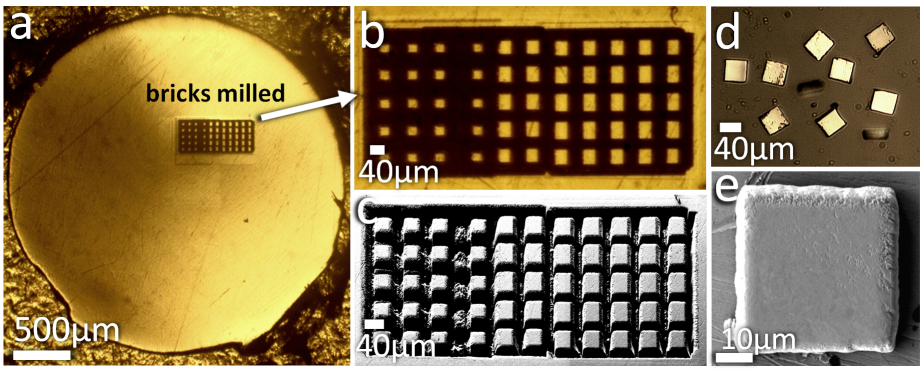

Figure 3.7: **Microphotographs (a, b, d) and SEM images (c, e) of Ta bricks in production.**
(a) A polished Ta foil (≈50 µm thick) with bricks milled out using the FIBM technique. (b),(c) Close-ups of milled Ta bricks before recovering. (d) Recovered and cleaned Ta bricks. (e) Close up of a single brick.

3.2.3 Sample loading in the DAC

In a typical DAC loading, a polished piece of single crystal sapphire (3-5 µm thick, 40-60 µm wide) was placed flat on the diamond culet with the Ta disc placed flat on top of it. Re gaskets, pre-indented to 35 µm were

used in a plate-DAC[60] with culet sizes ranging from 250 to 300 μm. The cells were loaded with 99.999% pure argon as a pressure transmitting medium, using a gas loader at 0.3 GPa and room temperature.

Upon reaching the desired experimental pressure, a 5-8 μm thick layer of argon served as a thermal insulation from the top diamond. Ruby grains (2-3 μm size) placed close to the sample served as the pressure markers. Before measuring the pressure, the sample chambers were annealed with a defocussed CW heating-laser operated at low powers to relax the deviatoric stresses in the argon medium, and above 50 GPa, Raman signal from the diamond culet was used as an additional pressure marker[205] (see Appendix C) due to broadening of ruby peaks. Pressures measured before and after flash-heating did not differ more than 2 GPa.

3.2.4 Experimental procedure

Microphotographs of a Ta sample (disc) were recorded before loading and after pressurising it to the desired pressure in the DAC. For optical alignment, the laser power was adjusted to create a hot spot on the sample at temperatures below the melting temperature of Ta at 1 atm to avoid any modification of the sample. Further, the laser-focus was adjusted to obtain a temperature gradient of < 10 K over the central area of the hot spot 3 μm in diameter, from which the temperatures were measured with the calibrated CCD spectrometer. The laser power was then set to reach a desired approximate temperature, inferred from many pilot runs. The sample was heated in a single event of 20 ms (flash), while recording the temperature. Microphotographs of the sample were recorded after this event and after sample recovery.

The recovered sample was then analysed using SEM (JEOL-JSM-6500F and ZEISS-AURIGA-40) for surface texture and FIBM (ZEISS-AURIGA-40) for depth-profiling, measuring the extent of melt, if any. Chemical analysis of Ta was done using EDS (JEOL-JSM-6500F) on the heated portions on the surface and in the interior exposed by FIBM.

This procedure was repeated with new samples at a given pressure until a temperature range was covered spanning about 400 K below and above a temperature at which a first smooth textured modification appeared in the heated area. As a melt-criterion, observation of the first textural modification represented the lower bound (onset) for the melting

temperature, while restructuring of bulk material to several micrometres in depth represented an upper bound. Flash-heating runs were carried out at 20, 22, 32, 35, 50, 65 and 85 GPa.

Unlike in case of Re/Mo, Ta discs were heated with a single flash per sample. Ta discs allowing multiple fresh areas for heating were found to get distorted due to pressure gradients in the sample chamber. With smaller discs, less number of fresh areas was available for heating and at times, textural features appearing at two adjacent flash-heated areas would overlap, complicating the textural analysis. Heating with a single flash at the centre of a disc avoided these problems. It also allowed for greater defocussing of the laser beam, thereby reducing temperature gradients across the area from which the temperature was measured. Moreover, the disc shape provided a reference for easy centring of the hot spot and the mirror pinhole for temperature measurement.

3.3 Analysis and results

3.3.1 Experiments at 1 atm

To test the accuracy and reproducibility of measurements with the described melt-criterion, a 30 μm thick polished Ta foil was flash-heated to different temperatures at different locations on it in argon gas flow at 1 atm, below and above the known melting point of 3270 K[183;184]. The argon environment prevented any detectable chemical reaction upon heating for all temperatures, as checked in the EDS, in stark contrast to experiments in air.

In Fig. 3.8, the first row (a) shows a sequence of microphotographs of different unheated locations on the Ta foil. These, after flash-heating at increasing temperatures, are shown in the second row (b). The third row (c) shows SEM images of the same areas as in row (b), magnified 3 times.

For further analysis and comparison, the heated and unheated areas probed using SEM, FIBM, and EDS are presented in Fig. 3.9. In the first row, a sequence of SEM images selected from Fig. 3.8 (row c), and an image of an unheated area is shown. In the second row the corresponding depth profiles created using FIBM by cutting across the modifications

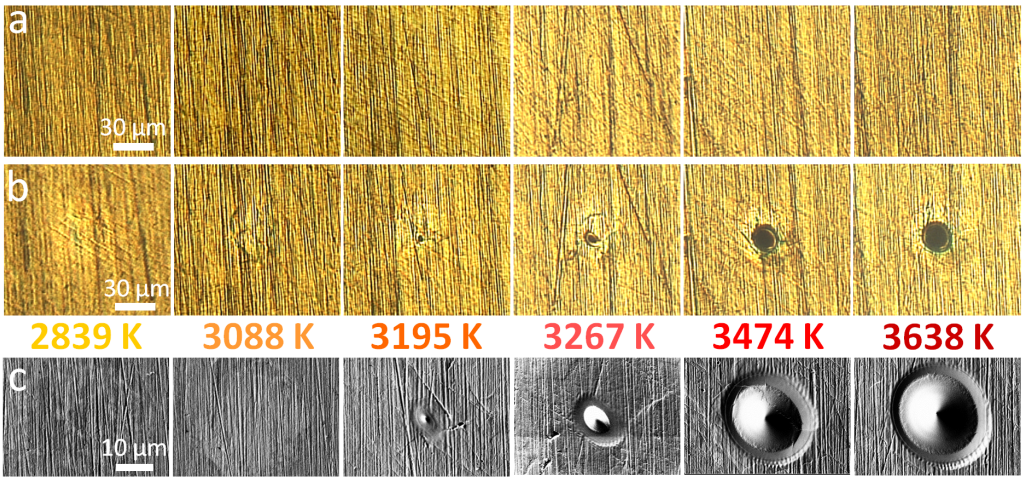

Figure 3.8: **Optical (row a, b) and SEM (row c) images of flash-heated Ta at increasing temperatures at 1 atm.**
The scales shown are for the respective rows. See text for further description.

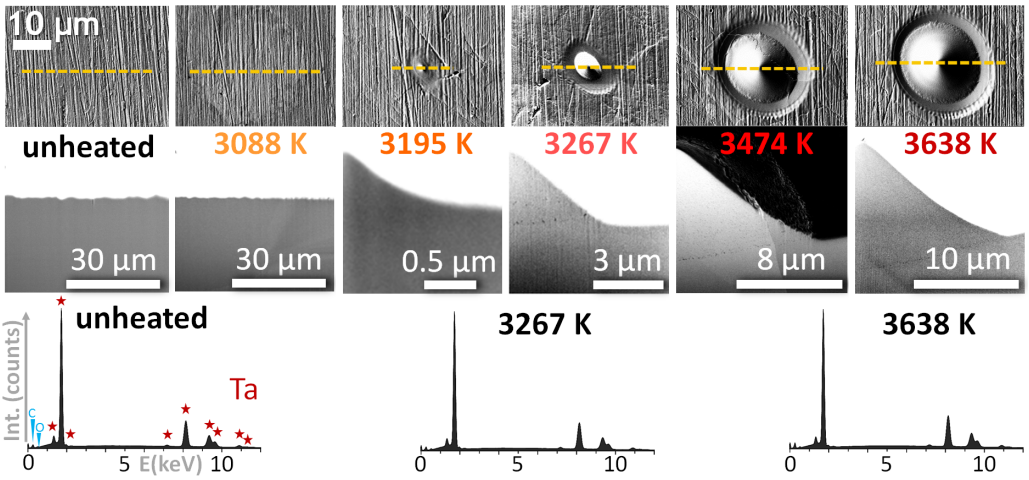

Figure 3.9: **SEM images of a Ta foil, flash-heated in argon flow at 1 atm as probed by SEM (row 1), FIBM (row 2) and EDS (row 3).**
See text for further description.

seen on the surface are seen. For clarity, only the right halves of full cross-sections of the profiles are shown in SEM images.

At 3195 K, the first surface modification in the form of a bulge was recorded. The depth profile at 3267 K shows a complete re-texturing of the heated portion separated by a boundary extending about 3 µm deep. With increasing temperature, the boundary of the bulge extended both, laterally and in depth. The third row displays representative EDS spectra for the runs at 300 K (unheated), 3267 K and 3638 K. These were collected from several parts of the displayed areas, and portions exposed in depth after FIBM. No evidence of a chemical reaction was found at these temperatures which span about 600 K across the known melting point. From above observations, the onset of melting is concluded to be at 3195 K ± 90 K (90 = (3267 - 3088)/2), but the amount of melt is too small to be visible in the depth profile compared to that for 3267 K.

For a closer inspection of textural differences among the rough solid surface, the quenched molten portion, and the boundary separating those, SEM images of an independent flash-melting event at 1 atm, 3430 K are shown in Fig. 3.10.

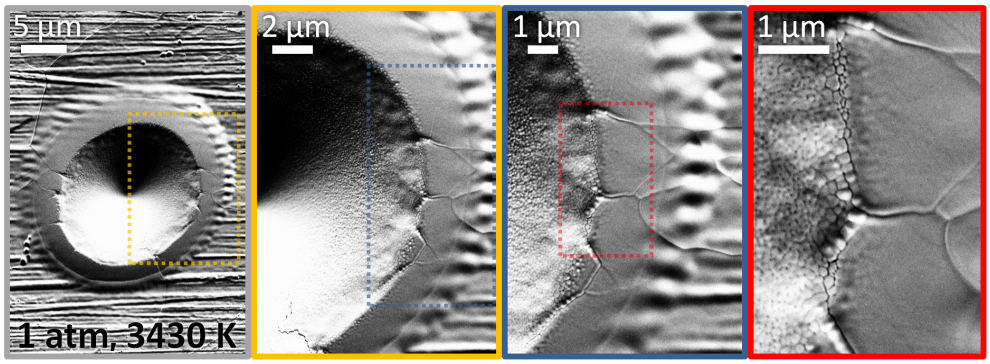

Figure 3.10: **SEM images of melt-features on Ta foil quenched from 3430 K at 1 atm.**
Areas enclosed in the dotted, colored rectangles are magnified in the successive images from left to right.

To find the source of the negligible carbon (C) and oxygen (O) detected in the unheated and heated/molten samples, a separate comparative EDS study was conducted with the instrument calibrated using a standard Ta specimen. The higher the energy of the incident electrons, the more is the depth and volume of the sample probed and at 25 keV, the incident electron beam probes a depth of about 800 nm for Ta[176].

By measuring and comparing the spectral intensities for a fixed electron current (1 nA) at 5, 15 and 25 keV, the source of the C and O was found to be only on the surface and not in the bulk of the material. The EDS instrument used has a sensitivity for 0.1-0.2% of C and O.

3.3.2 Experiments at high pressures

Out of the total of 71 runs carried out at high pressures, 42 are reported here (Fig. 3.18). The discarded runs include the test runs to optimise the laser power, laser defocussing, and flash-heating duration, along with a few experimental runs having unsatisfactory Planck-fits resulting from a hot spot being misaligned with the collection optics, or from a suspected chemical impurity.

3.3.2.1 35 GPa

In Fig. 3.11 microphotographs of Ta discs for two separate runs (a1 → a4 and b1 → b4) at 35 GPa are shown.

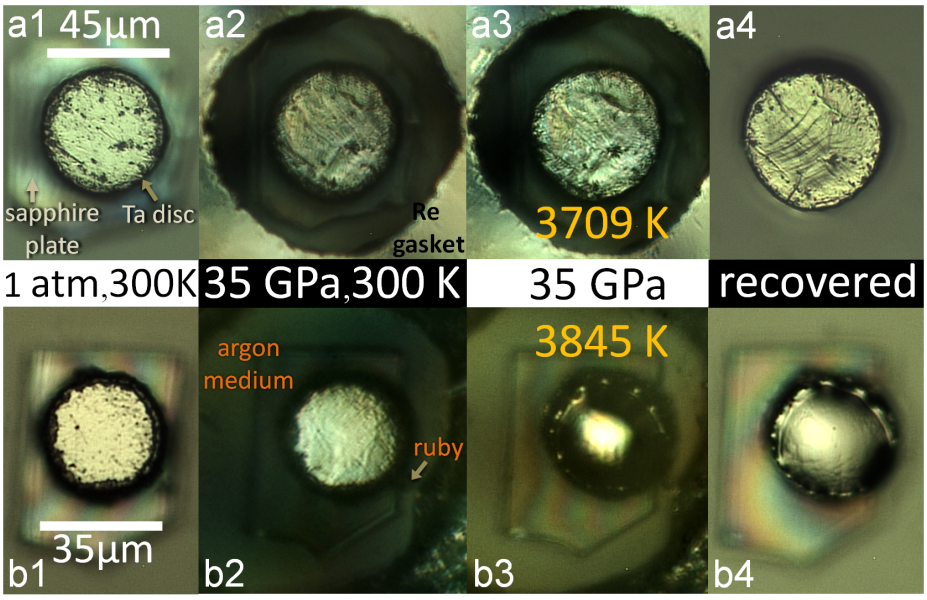

Figure 3.11: **Microphotographs of Ta discs at different stages in two separate flash-heating runs at 35 GPa.**
Scale bars are for the respective rows. See text for further description.

Images a1, b1 are of identically prepared Ta discs placed on thin sapphire plates at 1 atm before loading. a2, b2 show the discs pressurised to 35 GPa in argon medium in the DAC, before heating. The result of flash-heating these discs to 3709 K and 3845 K is shown in a3 and b3, respectively. Formation of a shiny smooth circular bulge was observed in b3, in contrast to the unaltered texture in a3. The textures remained intact upon recovering the samples to ambient conditions (a4, b4).

The recovered samples were further analysed using SEM as shown in Fig. 3.12 a, b, respectively. To compare the features of the un-molten and the molten areas in a and b, the respective depth profiles created across the heated areas (dashed lines) using FIBM are shown in a', b'.

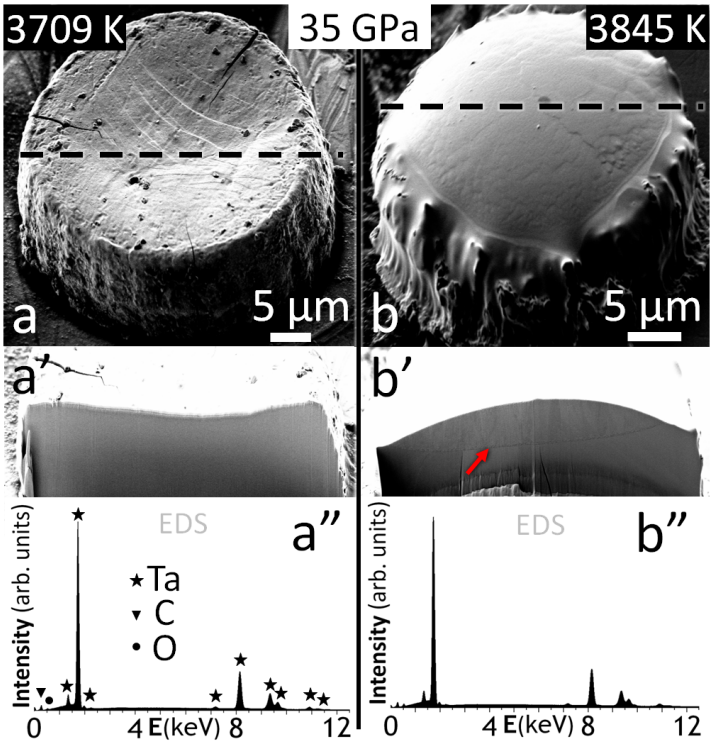

Figure 3.12: **SEM images (row 1, 2) of Ta discs flash-heated to different temperatures, recovered from two separate runs at 35 GPa and probed using SEM, FIBM and EDS (row 3) techniques.**
Red arrow indicates a boundary separating the quenched melt above and the unaltered solid below it. See text for further description. Scale bars are for the respective vertical panels displaying the two separate runs.

The surface textures for these temperatures differ significantly and the melt features are similar to the tests carried out at 1 atm (Fig. 3.9). In contrast to the unaltered texture several micrometres in depth at 3709 K (Fig. 3.12 a'), the profile at 3845 K (Fig. 3.12 b') shows a clear boundary, indicated by a red arrow, separating the quenched textured liquid from the smooth un-molten solid. Also, the concave portion around the centre of the disc seen in a, a' due to the pressure gradient is in strong contrast to the increased, convex volume of the quenched molten portion in b, b'. Polishing of discs during the sample preparation did not lead to any curved surface, as checked in the SEM. The respective EDS spectra at 25 keV revealed no chemical reaction across the melting transition, as inferred by comparing a" and b".

3.3.2.2 50 GPa

As another example, flash-heating runs at 50 GPa are presented Fig. 3.13 and Fig. 3.14.

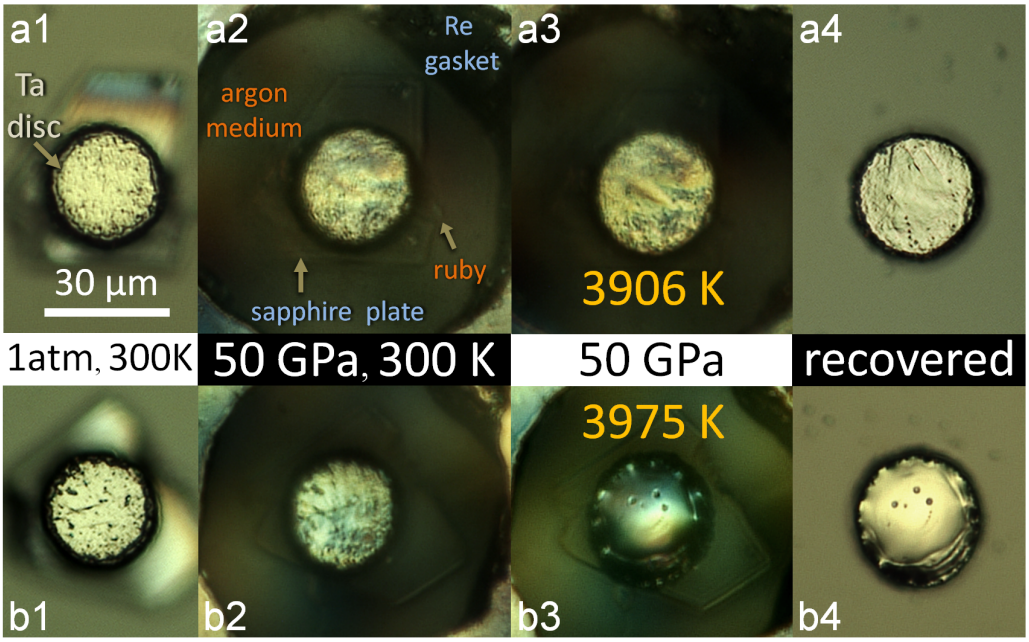

Figure 3.13: **Microphotographs of Ta discs at different stages in two separate flash-heating runs (row 1, 2) at 50 GPa.**
Scale shown is for the entire figure. See text for further description.

Fig. 3.13 shows microphotographs of Ta discs for two separate runs (a1 → a4 and b1 → b4) at 50 GPa. Identically prepared Ta discs placed on thin sapphire plates at 1 atm (a1, b1) were pressurised to 50 GPa in the DAC (a2, b2). The discs after flash-heating (a3, b3) show that at 3906 K there is no textural change whereas at 3975 K a shiny bulge is formed. The convex, shiny, and smooth melt features (b4) contrasting the unaltered rough features (a4) are retained upon recovery to ambient conditions.

The recovered samples (Fig. 3.13 a4, b4) were further analysed using SEM, FIBM and EDS probes. The results are presented in the left and the right panel of Fig. 3.14, respectively.

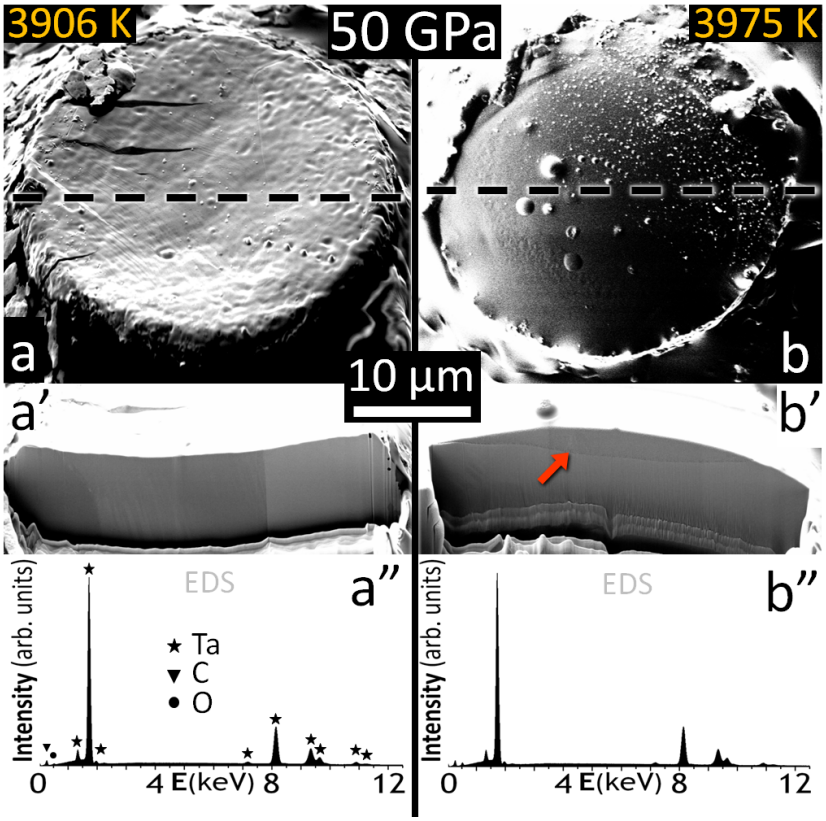

Figure 3.14: **SEM images (row 1, 2) of Ta discs flash-heated to different temperatures, recovered from two separate runs at 50 GPa and probed using SEM, FIBM and EDS (row 3) techniques.**
Red arrow indicates a quenched melt-solid boundary. See text for further description.

The samples in SEM images a, b are cut across the black dashed lines using FIBM and are shown in a' and b', respectively. As found at 35 GPa, the depression at the central portion of the sample before melting and the bulged molten volume above the sample surface after melting are evident for 50 GPa as well. A red arrow in b' shows a sharp boundary separating the quenched melt above and the un-molten solid below it, whereas the texture in a' is unaltered throughout the depth, indicating no melting. The EDS spectra collected from the heated areas compared in a" and b" show no chemical alterations upon melting.

For clarity, the FIBM cross-sections at 35 and 50 GPa discussed so far are shown together in Fig. 3.15. The depth of melt features is seen extended to 4.5 μm for 35 GPa (a) and to 2.5 μm for 50 GPa (b).

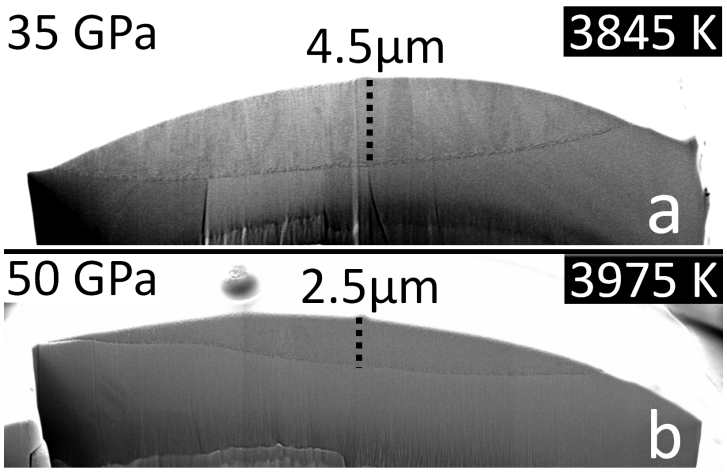

Figure 3.15: **SEM images of FIBM cross-sections of Ta showing the extent of molten portions in samples recovered from 35 GPa, 3845 K and 50 GPa, 3975 K.**

3.3.2.3 85 GPa

Due to technical difficulties like breaking of diamonds upon release of pressure and subsequent loss of samples, only two data points could be obtained at 85 GPa. In these two separate runs on different samples, no textural changes were observed for the one flash-heated to 3731 K, whereas a smooth bulge was observed at 4318 K for the other (Fig. 3.16). Upon recvery, this bulge was found to be less than a micrometer in depth and hence, 4318 K was assigned as the onset or the lower bound on the melting temperature.

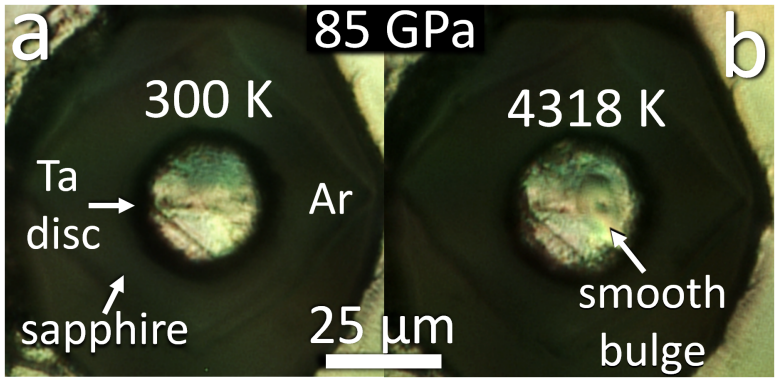

Figure 3.16: **Microphotographs of a Ta disc before and after flash-heating at 85 GPa.**
a: Ta disc in argon medium before heating, b: A small smooth bulge was observed on the same Ta disc after flash-heating to 4318 K.

At pressures above 85 GPa, smaller culet sizes, smaller sample chambers and higher pressure gradients constrained the sample dimensions to less than 20 µm in diameter and thinner than 5 µm. Such small samples were not only difficult to prepare by laser-cutting and to handle, but these also created difficulties in aligning the centre of the laser hot spot with the mirror-pinhole of the spectrometer to measure temperatures.

In addition, a slight imperfection in centring the sample with respect to the sample chamber distorted the sample shape and surface while pressurising to such high pressures, resulting in nonuniform heating and unreliable temperature measurements. Results of such experiments were discarded.

3.3.2.4 Ta brick-melting

To check if the sample preparation using laser-cutting had any effect on melting temperatures, flash-heating test runs were carried out on bricks of Ta (10-50 µm wide, 6-9 µm thick) prepared using FIBM (Fig. 3.7).

At the typical energy (30 keV) of the incident gallium ions for milling, the damage to the structure of Ta bulk is limited to nanometres[206] below the milled surface. Melting data for both cutting processes were in a mutual agreement, making the melting curve independent of the sam-

ple preparation technique. An example of flash-melting of a Ta brick is shown in Fig 3.17.

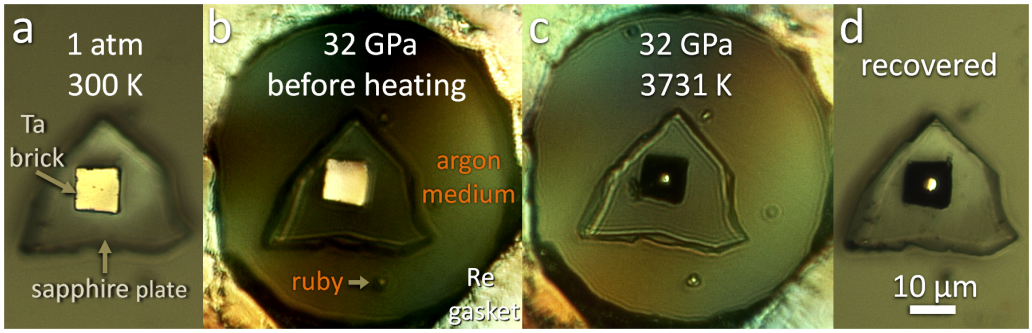

Figure 3.17: **Microphotographs of flash-melting of a Ta brick, prepared by FIBM.**
Images a, b: The yellowish shine on the polished Ta brick is due to optical illumination. Images c, d: After flash-heating, the same illuminated portion got reduced to a spot due to bulged up molten portion on the brick similar to the discs recovered in Fig 3.11 and Fig 3.13.

Again, for pressures above 85 GPa, constraints on the sample size made the alignment for temperature measurement difficult.

The data for Ta melting was thus limited to 85 GPa as the sample preparation, handling and recovery, and accurate measurements of temperature became an exceedingly challenging task with a further increase in pressure. Analysis using SEM and EDS was performed for all 42 runs carried out on Ta discs from 20 to 85 GPa and FIBM was done whenever depth profiling was required.

3.3.3 Results

Flash-heating data for Ta discs is plotted in Fig. 3.18. Each data point represents P-T conditions of a separate run on a fresh and identically prepared Ta sample.

The P-T conditions of flash-heating leading to no textural modifications on samples were designated as 'solid' data (◇), those resulting in melt features to several micrometres in depth are 'molten' data (●). The

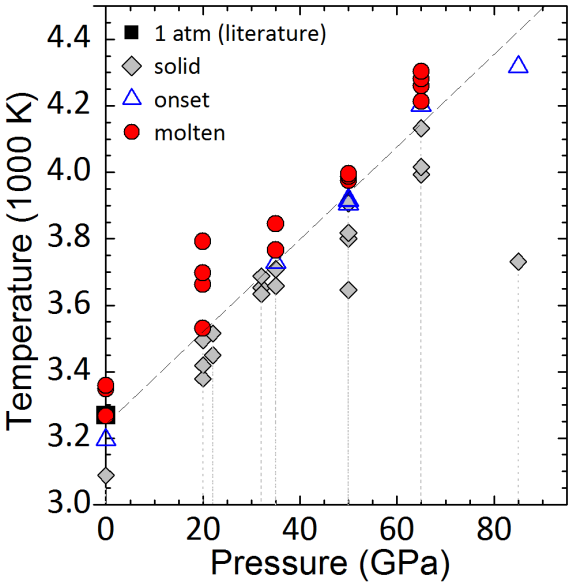

Figure 3.18:
Single-flash-heating data on Ta discs in the DAC. Dashed line is a guide to an eye. See text for further description.

conditions for which textural modifications were only on the sample surface, similar to that at 3195 K in Fig. 3.9, were designated as the 'onset' of melting (△), as these represent lower bounds for 'molten' data, consistent with the observations at 1 atm.

3.4 Discussion

In this work, a melting point is reported as the temperature corresponding to an 'onset' with an uncertainty equal to the difference between the lowest temperature for a 'molten' and the highest temperature for a 'solid' data point (Fig. 3.19). The highest uncertainty for the high pressure data is less than ±80 K, which is less than 4%. The uncertainty for the melting temperature at 85 GPa is not calculated due to insufficient number of runs (see subsection 3.3.2.3) but inferred to be within ±100 K from the runs at lower pressures.

Ta melting temperatures obtained from flash-heating are compared with selective earlier static data in Fig. 3.19 and with all experimental and computational melting curves of Ta in Fig. 3.20.

The melt-slopes are obtained by fitting Simon-Glatzel equation[23] to the data presented in Fig. 3.19. For flash-heating data, the melt-slope at 1 atm, 3270 K, is 13.9 GPa/K, which is close to but lower than that for

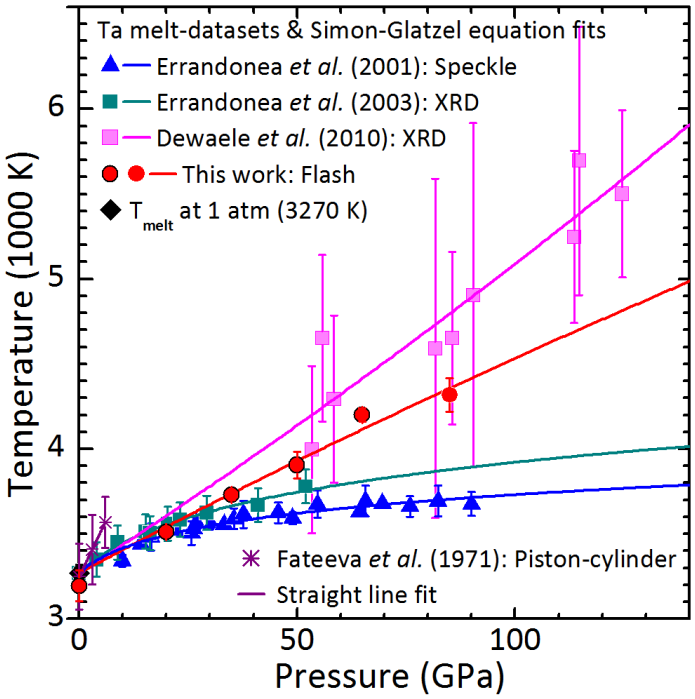

Figure 3.19: **Flash-melting data on Ta compared with previous static melting data.** The symbol-size (● = 125 K) is bigger than error-bars for some of the flash-melting data. The data point at 85 GPa (●) is the onset of melting with uncertainty inferred from data at lower pressure. See text for further description.

Dewaele *et al.* (16.5 GPa/K) and much lower than the lowest slope (34.3 GPa/K) for Liu *et al.* (2008)[193] among the computed curves. For a detailed quantitative analysis and a comparison with other data at ambient and high pressure, see Appendix F. The following discussion comprises the qualitative nature of the melting curves.

The data obtained by means of visual observation, namely the speckle method[79] and the melt-quench method[65;79] result in similar slopes at high pressure and hence, data from the speckle method is considered as a representative for comparison. From Fig. 3.19, it is evident that the flash-melt slope at high pressure is steeper than that obtained from the speckle method. The speckle method attributes the onset of melting to a motion of laser-speckles due to textural changes of the sample surface during melting. It has been used for identifying melting of materials from a variety of classes[78–86]. Yet, the data from it underestimated the melting temperature e.g. by 500 K at 85 GPa (Fig. 3.20), even though the FIBM profiles of flash-heated Ta allowed to identify the onsets unambiguously. Such a large discrepancy cannot be explained by experimental uncertainties. Since none of these reports of 'visual observation' present

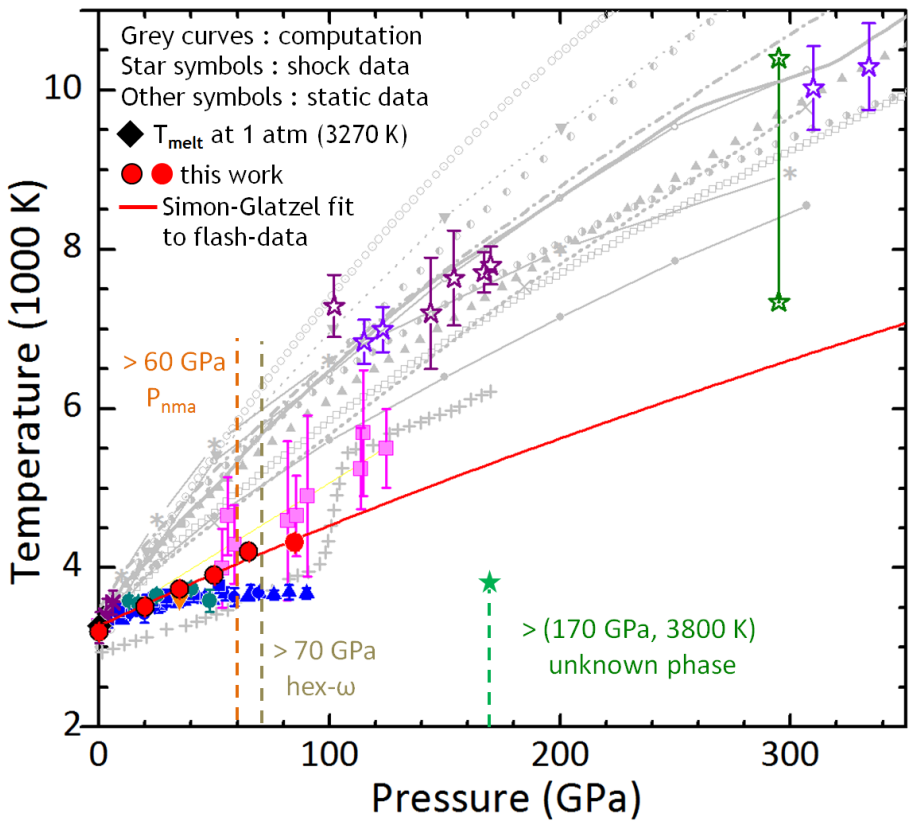

Figure 3.20: **Flash-melting of Ta compared with static data, shock data and computation.**
The symbols, relevant details and references are described in Fig. 3.2, Fig. 3.19 and in section 3.1. For flash-melting data, the symbol-size (● = 200 K) is bigger than the uncertainty for any of the melting temperature.

any chemical analysis of the heated samples, the discrepancy could be due to chemical contamination caused by long heating durations in these studies as observed in the recent XRD report[131].

Regarding the difference between the flash-melting results and the ADXRD measurements in the double sided LHDAC by Dewaele *et al.*[131] reporting a steeper melting curve, the following explanation can be offered. In these XRD measurements, which are carried out on about 5 μm thick samples and probed by an X-ray beam of 2×3 μm^2, the melting cri-

terion was the appearance of a diffuse scattering ring and/or spots due to fast recrystallisation in the diffraction pattern. As evident from the FIBM profiles, the melt is extended to more than 2 μm in depth of the laser heated portion (Fig. 3.15). It suggests that at these temperatures, in a 5 μm thick sample heated from both sides, such a large proportion of liquid compared to solid within the X-ray beam should have indicated melting. Therefore, the overestimation of the melting temperature in the XRD report could be due to a misalignment between the hot spot and the X-ray beam and/or misalignment of the spectrometer with the hot spot due to poor optical resolution[64].

In case of a perfect alignment, these measurements underline the possibility of overestimation of the melting temperature due to a small volume of melt compared to the un-molten portion within the X-ray beam, as discussed in the subsection 1.4.1. In contrast to such measurements, flash-heating demonstrated a robust and accurate temperature measurement of the onset and further melting without a sign of chemical contamination. As a result, there is about an order of magnitude improvement in the error-bars compared to the XRD study with the steeper slope[131].

In the earlier XRD measurements by Errandonea *et al.*[186] reporting a flat melting curve, the heating durations were longer compared to the above mentioned XRD study. So the discrepancy could be due to a combined effect of a misalignment and chemical contamination.

Compared to the melt-slopes from computational results and shock data, the present melt-slope is distinctly lower. However, unlike earlier results, a clear evidence of melting and the new level of precision in measuring melting temperatures for Ta, flash-melting data put unprecedented constraints on its melting slope, calling for a reevaluation of theoretical, LHDAC, and shock compression approaches to determine melting at high pressures.

The flash-melting slope starts deviating from the slopes of other static methods above 50 GPa, where the *Pnma* and hex-ω structures are predicted (Fig. 3.20). Although, obtaining any information about structure is beyond the scope of the method presented here, a relevant structural analysis is possible using the Transmission Electron Microscopy (TEM) performed on FIBM cross-sections of the heated areas of a recovered Ta sample.

3.5 Summary and further study

Flash-heating in the milliseconds regime combined with SEM, FIBM and EDS analysis on the recovered samples produced significantly more accurate data up to 85 GPa than previous melting experiments with melting temperatures bracketed within ±100 K. The textural modifications are very reproducible and unambiguous, and chemical contaminations are carefully monitored for the first time to ensure sample purity.

In contrast to previous melting measurement on tantalum using XRD which showed large uncertainties, the present melting curve cannot be reconciled with shock measurements and theoretical predictions.

The present work solves two major problems in melting experiments on tantalum: detection of the onset of melting and chemical contamination.

For further analysis, performing TEM on the cross-sections of the flash-heated tantalum recovered from different temperatures at a fixed pressure may provide the necessary structural information in resolving the phase transitions predicted by theories at the high P-T conditions.

Moreover, for determining the structure of material during a melting transition, flash-heating in milliseconds time-scale combined with *in-situ* synchrotron XRD measurements are now possible with fast X-ray detectors (Pilatus), provided the sample is well confined and perfectly aligned during melting.

With the new precision, flash-melting of tantalum presented here is a definite step ahead in resolving the long standing controversy about melting temperatures of tantalum as well as other metals at high pressures.

——o——

Publication based on this chapter:

Flash melting of tantalum in a diamond cell to 85 GPa
A. Karandikar and R. Boehler
Physical Review B 93, 054107 (2016)
DOI: 10.1103/PhysRevB.93.054107

——o|o——

Chapter 4

Summary, scope, limitations & outlook

4.1 Summary

A new 'laser flash-heating' method has been developed for measuring melting temperatures above 2000 K in a diamond anvil cell at gigapascals of pressure. It overcomes the general difficulties in detecting an onset of melting in a diamond anvil cell. It also circumvents the notorious experimental difficulties associated with the long heating durations of the CW laser-heating and the short timescales in the pulsed laser-heating and shock-compression experiments.

In this method, the duration of heating a sample is tuned to avoid chemical reactions of the sample with the diamond anvils and the surrounding pressure medium, while maintaining the accuracy of the temperature measurements. The absence of chemical reactions is confirmed by the EDS technique.

Melt detection is now unambiguous from the analysis of textures on the surface and in depth of the recovered samples using the SEM and FIBM techniques, respectively.

Using this method, the following has been achieved.

1. The melting curve of hcp-Re has been measured to 48 GPa, 4200 K for the first time. It has a significantly steeper slope than those observed for other transition metals like W and Mo with bcc structures. Above 20

GPa, Re becomes the most refractory metal surpassing W.

2. The melting curve of bcc-Mo has been measured to 45 GPa, 3100 K. It agrees with previous melt-slopes approaching zero value with pressure as reported in the LHDAC experiments using ADXRD and visual observation techniques for inferring the onset of melting. Flash-heating experiments at pressures higher than 50 GPa are required to further corroborate the flat melt-slope and resolve the long standing controversy about melting of Mo.

3. The melting curve of bcc-Ta has been measured to 85 GPa, 4300 K. Unlike in previous experiments using ADXRD and visual observation as probes, it has been tightly bracketed with an unambiguous detection of the onset of melting, without any chemical reaction. The present melting curve cannot be reconciled with shock measurements and theoretical predictions, and the precision of measurements calls for a reevaluation of theoretical, shock compression, and other DAC approaches to determine melting at high pressures. A further analysis with TEM technique for investigating the structure of the heated portion below and above melting temperatures of Ta may benefit in resolving various phase transitions predicted to explain the vast discrepancies in the reported melt-slopes.

When extrapolated to one atmosphere pressure, all the measured flash-melting curves agree with the known melting points.

4.2 Scope of the method

1. Flash-heating preformed in a DAC in the milliseconds time-scale bridges the gap between static and shock measurements on melting at high P-T conditions. It avoids sample instability, chemical reactions, is reproducible and brackets the melting temperatures within ±100 K.

2. It allows further analysis and characterisation of the recovered samples using the SEM, FIBM, EDS and TEM techniques.

3. It can be adapted to routine synchrotron XRD measurements with fast and sensitive X-ray detectors, provided the sample is well confined and well aligned during a temperature measurement.

4. It can be adapted to measure melting temperatures of nonmetals by using a CO_2 laser (λ: 10.6 μm) and modulating its power with a timescale to that used for heating metals.

4.3 Limitations of the method

It is challenging to prepare identical samples, especially from soft metals, that maintain their texture and shape as the pressure increases.

At each pressure many flash-heating runs are required and each run requires a fresh sample. A large enough number of identical samples needs to be prepared.

The flash-melting data are limited by the pressure at which the sample dimensions are required to be less than 25 μm wide and 5 μm thick to avoid distortions caused by steep pressure gradients in the sample chamber. With smaller sizes, the optical alignment of the hot-spot on the sample required for accurate temperature measurements becomes exceedingly difficult.

The sample analysis is conducted *ex-situ* using SEM, EDS and FIBM techniques, which is more time consuming than the previous methods of detecting melting, namely the speckle method, the melt-quench method and the XRD, or the *in-situ* probes like Raman spectroscopy.

Probing the structure of a sample just before it melts is beyond the scope of SEM, EDS and FIBM techniques. To obtain any structural information, a cross-section of the relevant portion of the sample prepared by FIBM needs to be analysed using TEM.

This method is not applicable to substances such as solid forms of gases and liquids that cannot be recovered at ambient conditions for SEM or EDS analysis.

4.4 Outlook

The ultimate goal in measuring melting temperatures at high pressures is to be able to measure the X-ray structure factors across the transition from solid to liquid state. However, so far, the efforts have been limited by the experimental difficulties associated with melting in the LHDAC, the most notorious being the increasing sample instability with temperature. The sample and the melt is required to be confined during and above melting long enough to collect a significant amount of signal from XRD and thermal radiation.

With recent advances in the X-ray detector technology, the Pilatus detectors (DECTRIS®) acquire diffraction signals in a few milliseconds,

unlike the routinely used X-ray CCDs which require a few seconds of exposure. This allows the desired drastic reduction in the heating duration from seconds to milliseconds, bringing XRD measurements in the regime of flash-heating timescale.

It is also required that the entire sample within the X-ray beam melts together. Otherwise, the X-ray diffraction signal from the un-molten solid dominates the X-ray scattering signal from the relatively small amount of melt. A typical synchrotron X-ray beam being a few micrometres in extent, the limitation in aligning it with the micron-sized samples with the optics and the laser hot spot dictates the sample size to be < 10 μm.

The single sided flash-heating runs on refractory metals have now unambiguously demonstrated the extent of melting to be a few micrometres at a temperature just above the melting temperature, and that melting is reached within tens of milliseconds. This gives a crucial information that assures melting of the entire sample within the X-ray beam with double sided laser-heating of the typical 10 μm thick sample. It also underlines the stringent requirements on the precise control of laser power and time in such experiments.

Recently, a novel encapsulation of single crystal sapphire that confines the melt for studying melting of metals has been successfully tested in a synchrotron X-ray Absorption study of iron-melting at megabar pressures using a CW-LHDAC[63] at the European Synchrotron Radiation Facility (ESRF), France.

Until such an encapsulation becomes a part of the routine tool for measuring structure factors in long durations of heating, the flash-heating method with the SEM, EDS, FIBM and TEM analysis promises accurate, reproducible, robust and chemically clean data on melting.

—o— ● —o—

Appendices

Appendix A

Diamond anvil cell

The work presented in this thesis was carried out using a plate type diamond anvil cell (DAC)[60]. The interior and photos of the cell are displayed in Fig. A.1, while the generic features are described in subsection 1.3.2.

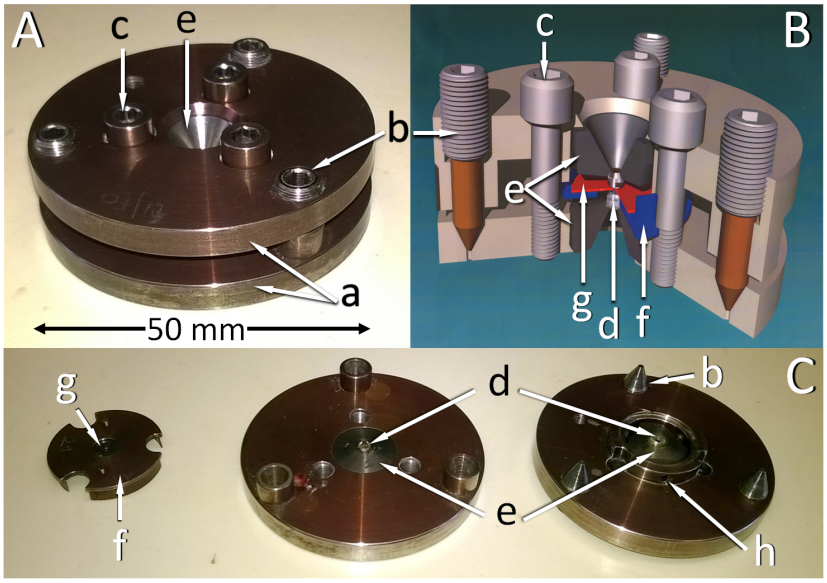

Figure A.1: **Photographs and interior of the diamond anvil cell**
A: Photo of a closed cell. B: Computer generated drawing of the interior of a closed cell (Courtesy R. Boehler). C: Photo of an open cell. The top and bottom plates in A and B are respectively seen in the middle and to the extreme right in C. See text for description.

In fig. A.1, a: Maraging steel plates (DIN 2709, HRC 55), 50 mm diameter, 5 mm thick. b: Screws (M6/0.5 mm) for adjusting tilt of the plates and maintaining a safe distance between the diamonds. c: Screws (DIN 2709, HRC 55, fine thread M5/0.35 mm) for bending the plates to advance diamonds towards each other and generate pressure. d: Polished diamonds with a conical base. e: Tungsten carbide seats that support diamonds. The upper seat is press-fitted in the plate. f: Gasket holder. g: Metallic gasket with a hole drilled in it and fixed to the gasket holder by means of screws. h: Set screws (M2.5) for lateral alignment of diamond seat.

These cells are designed for a quick and sturdy alignment of diamonds, simple loading of samples and an easy operation. A gasket with a hole, serving as a sample chamber, is fixed to the gasket holder by screws. To position the gasket on the culet accurately and reproducibly, the gasket holder is pressed onto the ring around the WC seat in the bottom plate (extreme right in C). Turning the inner screws (c) simultaneously and equally bends the plates, brings the diamonds closer, and pressurises the chamber. The screws advance by 350 μm upon one full turn. The external gear mechanism to turn the screws is shown in Fig. A.2. The fine pitch of the inner screws allows a precise pressure control.

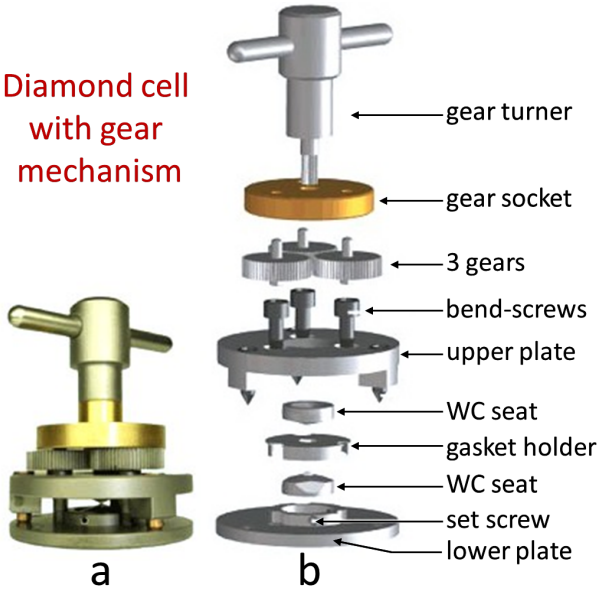

Figure A.2: **Gear mechanism for the diamond anvil cell.** a: Gears ready to turn to pressurise the closed cell. b: Exploded view showing components of the cell and gear mechanism. Images adapted from http://www.almax-easylab.com

——o——

Appendix B

Planck's radiation law and temperature measurement

The Planck function[207] P_v for energy radiated per unit volume per unit wavelength by a blackbody in thermal equilibrium is

$$P_v(\lambda, T) = 8\pi hc\ \lambda^{-5} / (e^{hc/\lambda K_B T} - 1) \quad \text{where,}$$

T: equilibrium temperature [K], λ: wavelength [m],
h: Planck's constant (6.026×10^{-34} Js), c: speed of light in vacuum (3×10^{8} m/s), K_B: Boltzmann's constant (1.38×10^{-23} J/K)

For a real (grey) body at an equilibrium temperature T, it takes the form

$$I_v\ (\lambda, T) = \epsilon(\lambda, T)\ P_v(\lambda, T), \quad \text{where,}$$

ϵ: emissivity. Emissivity is the ratio of radiation emitted from a real body to the radiation from a black body at the same temperature in thermal equilibrium[208]. ϵ is 1 for a black body and between 0 and 1 for a grey body.

In a laser-heating set up, the thermal radiation is collected from a heated sample surface by the set up optics, and is derived from P_v as

$$I_s\ (\lambda, T) = f(opt)\ \epsilon(\lambda, T)\ 2\pi hc^2\ \lambda^{-5} / (e^{hc/\lambda K_B T} - 1) \quad \text{where,}$$

I_s = Energy radiated per unit surface area per unit wavelength at T.
f(opt) = optical transfer function of the optics set up for collecting thermal radiation.

In a simplified form -

$$I_s(\lambda, T) = \text{f(opt)}\, \epsilon(\lambda, T)\, c_1\, \lambda^{-5} / (e^{c_2/\lambda T} - 1) \quad \text{where,}$$

c_1 (= 340.76×10^{-18} J/m^{2}s) and c_2 (= 13.1×10^{-3} m.K) are constants.

The above expression is used to calculate the unknown temperature T as follows:

I_s measured for each λ: The spectral range used for collecting the incandescent light emitted by a hot sample is selected considering the sensitivity of the detector, the anticipated temperature, and the laser excitation wavelength. In the infrared region, Raman effect from the laser excitation (typically 1070 nm) and a nonlinear behaviour of emissivity complicate the spectra[142]. Collecting spectra in the 'visible' range of the electromagnetic radiation is more practical due to a following reason. The most commonly used silicon CCD detectors are sensitive in the 400–900 nm range in which the spectral intensity for temperatures 2000–7000 K is sufficient for curve-fitting using the Planck's equation. Hence, a grating and a spectrometer are chosen to disperse collected light in that range. For temperatures below 2000 K, an InGaAs detector having sensitivity in 1000–1600 nm is more appropriate.

$\epsilon(\lambda, T)$: The wavelength dependence of emissivity (ϵ) is known only for a limited number of materials in vacuum or at ambient pressure, and at selective temperatures[209–211]. At a given temperature, ϵ shows a near linear dependence on wavelength for a few metals and at higher temperatures, the dependence assumes higher values keeping the trend same[211]. However, this behaviour is not universal, and is seldom explored experimentally at high P-T conditions, e.g. emissivity of tungsten[209] decreases nonlinearly in the range (400 - 900) nm, and keeping the same functional form of the dependence, the emissivity decreases in value with increasing temperature. The dependence of emissivity on texture of the emitter at high P-T conditions is also little explored.

Therefore, to simplify the calculations, at high P-T conditions, ϵ is assumed to be 1, which typically results in an overestimation of temperatures[142]. The required corrections depend on the temperature and are estimated in the discussion on accuracy ahead.

f(opt): The optical elements and their alignment in the set up has a crucial effect on the temperature measurement[142]. To measure temperatures with a given optical set up, the optical transfer function (flatfield) for *that* optical set up needs to be calculated before the final measurement.

The incandescent spectrum $C_{T_{ref}}$ emitted by a calibration lamp at a known temperature T_{ref} is measured with the optics to be used later in the experiment. The intensity of $C_{T_{ref}}$ is mathematically divided by the intensity calculated from Planck equation at the T_{ref} in the same wavelength range. The resulting quotient is the $f(opt)$. The raw spectrum collected in an experimental run at an unknown temperature T is divided by the $f(opt)$ to produce a corrected spectrum. This spectrum is further fitted with the Planck function to extract T.

For the work carried out in this thesis, the temperature calibration was done using a tungsten ribbon lamp (Osram Wi17/G) traceable to the Physikalische-Technische Bundesanstalt. The accuracy of the calibration has been tested by measuring melting temperatures of platinum[75] and tungsten[142] within 10 K of the known values 3680 K and 2045 K, respectively, at 1 atm.

With the same optics used in above calibration, a custom made calibration lamp (Osram) with a tungsten filament having a single loop has been calibrated for temperature. This lamp is convenient to handle for a routine operation. When operated at a constant current of 450 mA, it reaches 2157 K, the reference temperature (T_{ref}) used in the calibration. The quality of the Planck-fit yields a precision of ±5 K, independent of pressure, temperature or material.

Accuracy of temperature measurement

1. The accuracy of temperatures measured upon calibrating the optical set up with the tungsten ribbon lamp was independently checked with a custom made blackbody source[212], with its temperature being measured with a thermocouple. Maintaining the blackbody temperature at 970 K, as recorded by the thermocouple, its temperature measured using

the optical set up calibrated with the tungsten lamp was 970±5 K. Above 1000 K, the heat radiated by the blackbody distorts optical elements of the set up causing an increase in uncertainty in the measurement.

2. Although the temperature is calibrated with a tungsten lamp, i.e. a tungsten filament enclosed in a glass envelope, temperatures measured in a DAC experiment are always through a diamond anvil that causes dispersion of the radiation emitted by the sample. In a test conducted[213] to assess the effect a diamond window, the temperatures measured with and without the diamond window were found to be within ±5 K. The effect of dispersion is further reduced by employing optics with a low numerical aperture, as used in the experiments presented in this thesis.

3. Compared to above uncertainties, the systematic error due to wavelength dependence of ϵ of the material being heated is higher. Assuming the wavelength dependence of ϵ of the heated sample to be same as that for tungsten[209], which is a reasonable assumption in case of some metals, the maximum deviation from a true temperature is calculated as follows.

For a given temperature, generate a theoretical blackbody spectrum in the wavelength range of the measurement. Multiply the spectrum by the known analytical form of the wavelength dependence of ϵ for tungsten[209]. Fit this spectrum with the Planck's equation to extract temperature T_1.

Carry out a similar calculation but with a reversed sign of the functional form of the wavelength dependence of ϵ for tungsten and extract temperature T_2.

The difference T_1-T_2 is the maximum systematic error in the measured temperature.

Such an exercise yields temperature corrections of about -100 K at 3000 K and about -350 K at 5000 K[214;215].

In summary, compounding the errors arising from calibration, fitting process, and presence of a diamond anvil, the temperatures reported in this thesis are accurate within ±20 K. Assuming a wavelength dependence of emissivity same as that for tungsten, temperatures are systematically overestimated at the worst by about 3% and 7% at 3000 K and at 5000 K, respectively.

——o——

Appendix C

Pressure measurement in a diamond anvil cell

In the laser-heated diamond anvil cell (LHDAC) experiments presented in this thesis, the pressure gauges/markers used to measure pressure in the sample chamber were ruby and diamond.

Ruby: Ruby crystals 2-3 μm in size are chemically inert, easy to load in a DAC, and do not interfere with the temperature measurement when placed close to the sample. Ruby (Al_2O_3:Cr^{3+}) emits a characteristic fluorescence spectrum (intensity vs. wavelength) consisting of two intense peaks at 694.2 nm (R1) and 692.8 nm (R2). With increasing pressure, a shift in the wavelength of R1 towards higher wavelengths is used as a pressure indicator[216].

The pressure dependence of the shift at 300 K has been calibrated using known phase transition pressures of organic liquids to 4 GPa[216;217], by fitting Decker equation of state (EOS)[218–220] to compression data on NaCl to 19.5 GPa[221]; which was later extended to 29.1 GPa[222], and using shock-EOS for simultaneous XRD measurements of volumes of metals Cu, Mo, Ag, and Pd to 100 GPa[223]. The ruby pressure scale has been further revised and tested for accuracy by different methods using various pressure media[224–233].

However, for elevated temperatures, use of ruby is limited due to several drawbacks[234;235]: 1. The peakwidth of R1 broadens and the peaks R1-R2 become unresolved above about 550 K, 2. Signal to noise (background) ratio for fluorescence drops drastically and almost diminishes

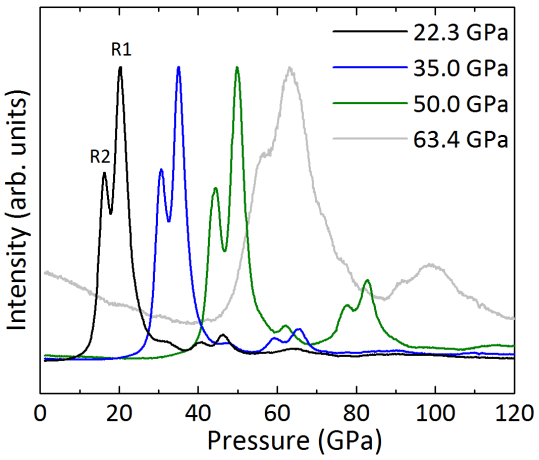

Figure C.1: **Shift of fluorescence peaks of ruby with pressure.**
The fluorescence was excited by a 473 nm laser (Laserglow Technologies, LRS-473-KM-100-10). Spectra were recorded for 0.5 s by a CCD (Pixis 100, Princeton Instruments) with a spectrometer (Jobin Yvon HR320) having 1200 l/mm grating. The intensities in each spectrum have been normalised with the respective highest intensity.

above 800 K, 3. R1 shift with temperature is large, 4. P-T dependencies of the R1 shift may not be independent of each other and are found to systematically underestimate pressures at high P-T conditions.

Since, for the laser-heating experiments presented in this thesis the pressure was measured *ex-situ* before and after heating in argon medium at 300 K, ruby was reliably used as a pressure marker with the following equation[236] that has been obtained from measurements using argon pressure medium.

$$P = (1904/B)\,((1 + \Delta\lambda/\lambda_o)^B - 1) \quad \text{where,}$$

P: pressure (GPa), λ_o = wavelength of R1 at 1 atm = 694.2 nm, $\Delta\lambda$ is the shift in R1 value from 694.2 nm. B = 7.665 and 5 for quasi-hydrostatic and non-hydrostatic conditions, respectively. For the work presented in this thesis, pressures were calculated using B = 7.665.

Diamond: For melting experiments on tantalum to 85 GPa presented in this thesis, diamond was used as a pressure marker in addition to ruby as the R1 peak was found to get considerably broadened above 50 GPa (Fig. C.1). At 1 atm, the first order Raman spectrum collected from the centre of the diamond culet shows a sharp peak at 1334 cm^{-1}. With in-

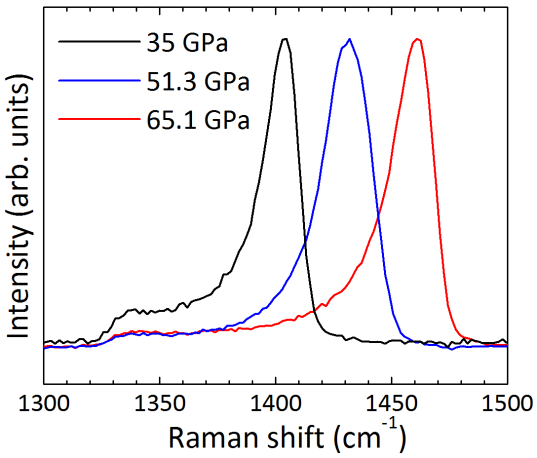

Figure C.2: **Shift of Raman-edge of diamond with pressure.** The Raman scattering was excited by a 671 nm laser (Laserglow LRS-0671-TSM-00100-10). Spectra were recorded for 1 s by a CCD (Pixis 100, Princeton Instruments) with a spectrometer (Jobin Yvon HR320) having 1200 l/mm grating. The intensities in each spectrum have been normalised with the respective highest intensity.

creasing pressure, the peak gets broadened and an edge is developed at the higher frequency end. The edge becomes prominent in intensity and its position shifts towards higher wavenumbers due to increasing normal stress at the culet [237] (Fig. C.2).

This shift has been calibrated up to 250 GPa [205], and later extended to 310 GPa [238] with the pressure derived from EOS of platinum. The calibration yields the following quadratic equation [205] that is used to calculate pressure from the frequency of this Raman edge:

$$P = 66.9 - 0.5281\nu + (3.585 \times 10^{-4})\nu^2 \quad \text{where,}$$

P: pressure (GPa), ν: the frequency (cm^{-1}) of the Raman edge for diamond.

——o——

Appendix D

SEM and EDS techniques

In Scanning Electron Microscopy (SEM), an energetic electron beam is used to scan a sample nondestructively to produce images with high spatial resolution, down to nanometre scale.

The limitations of an optical microscope, namely its ability to spatially resolve objects below the micrometre range and a small depth of field are overcome in SEM by focussing electrons of an appropriate energy at a long working distance by electromagnetic lenses[239].

Principle of operation[176;240;241]: A beam of electrons, accelerated and focussed onto a sample interacts with the sample atoms in a variety of ways.

In an inelastic interaction, an incident (primary) electron (PE) transfers a part of its energy to ionise an atom from the target and free an electron. If this electron has sufficient energy to come out of the surface, it is emitted as a secondary electron (SE). In another interaction, a PE passing close to a positively charged nucleus of an atom can be deflected all the way and gets sent back towards the direction it came in from. The deflection could be from a single nucleus or multiple nuclei (see Fig. D.1). Such an electron, when emitted from the surface, is called a back-scattered electron (BSE). As its energy is close to that of a PE, the interaction is treated as an elastic scattering process.

The penetration depth of a PE is larger for its higher energy and is smaller for a target with a high atomic number (Z). The number of SEs emitted per PE strongly depends on their energy, the target material, the surface structure, and the angle of incidence. The BSE emission also de-

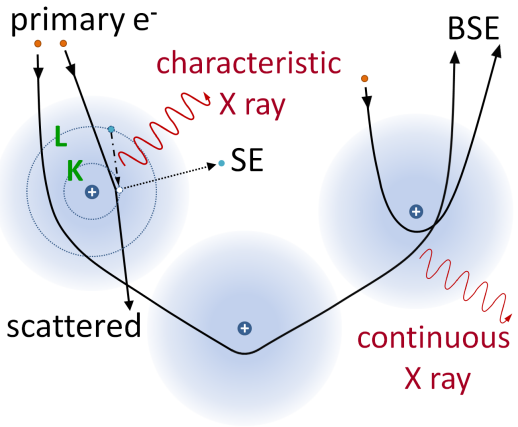

Figure D.1: **Incident electrons interacting with target atoms.** Diffused blue circles: target atoms with nuclei at their centres. Solid line: path of an incident e^-. Dotted arrow: path of a secondary e^- (SE). Dotted circles: K, L shells of an atom. Circles with white and blue interiors: e^- vacancy in K and an e^- in L shell, respectively. BSE: backscattered e^-. See text for description.

pends on the Z of the target atom. The SE and BSE signals are detected by appropriate detectors and are precessed further to produce an image of the target area. While the SE imaging captures topographic features, the BSE images exhibit elemental contrast (Z contrast) in the target.

Instrument specifications[241]**:** For the work presented in this thesis, two SEM instruments were used. A JEOL-JSM-6500F machine and a Zeiss-AURIGA-40 machine are both located at the Carnegie Institution of Washington, Washington DC (USA). While JEOL is exclusively used for SEM and Energy Dispersive X-ray Spectroscopy (EDS), the AURIGA machine is a Focused Ion Beam (FIB) facility coupled with SEM and EDS probes.

The schematics of the Zeiss-AURIGA-40 machine are discussed in Appendix E. Here, the generic features of a JEOL machine are depicted in Fig. D.2. A tungsten needle emitting electrons due to 'Field Emission' effect is the source of electrons. A high extractor voltage extracts and accelerates those towards an electromagnetic condenser lens. The lens focusses and directs the beam to an objective lens which further focusses it on the sample. Electromagnetic coils situated near the objective lens deflect the electron beam to raster-scan the target area for imaging.

The sample needs to be electrically conducting and must be mounted on a conducting, grounded stage to carry away any charge piled up on the sample due to irradiation. Electrically insulating samples are either coated with graphite, or metals like gold and iridium. Copper or carbon

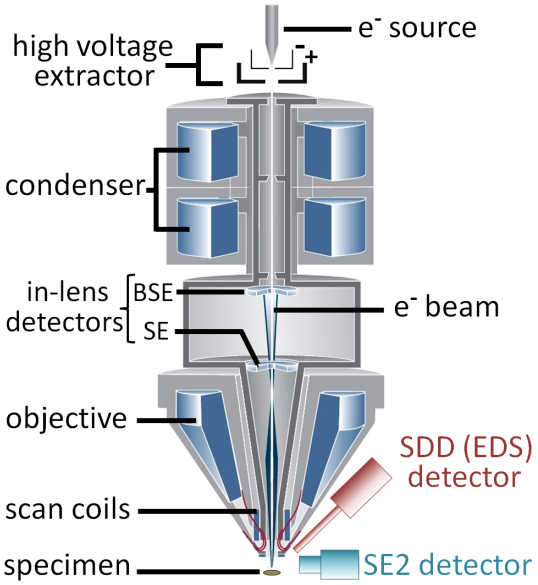

Figure D.2: **Schematics of a typical SEM column.** The figure is adapted from ref. [242]. See text for description.

tapes fixed on the sample also serve the purpose. The instrument is calibrated at a working distance of 10 mm and for 1 nA electron current at the electron energies 5, 15, 20, 25 keV. The vacuum in the sample chamber is maintained better than 5×10^{-4} Pa.

To produce images, the SE and BSE are detected by 'SE2' (also in-lens SE) and 'BSE' detectors, respectively. SE2, situated in the sample chamber, attracts SEs and sends those to a scintillator to produce photons. These photons are carried further by a lightguide to a photomultiplier tube that converts those to an amplified electrical signal for imaging. The 'In-lens' detectors are annular scintillators that are located behind the objective lens. 'BSE' detector collects BSEs and works on the same principle as that of the SE2 detector. The other interactions of PE with the sample include continuous and characteristic X-ray emission, Auger-electron emission and cathodoluminescence. Only the X-ray emission process relevant to this thesis will be discussed in the EDS part of this appendix. The entire instrument operation, from positioning the sample to imaging in the SE or BSE mode, is controlled by a software interface provided by the JEOL. The spatial resolution is 1.5 nm at 15 keV and the maximum magnification is 400,000×.

EDS: The Energy Dispersive X-ray Spectroscopy uses X-ray radiation emitted from the interactions of energetic electrons with a sample to identify the constituent elements, and quantify their relative proportion in the composition [243].

The EDS probe and the SEM instrument with which it is coupled have the same source of electrons. The two together reveal complementary information about topography and composition of a sample.

Principle of operation [240;243]: An energetic primary electron entering a sample interacts inelastically with an atom and transfers a part of its energy to free an electron from one of its shell. As an instance, as depicted in Fig. D.1, an electron from the K shell is knocked off creating a vacancy. An electron from an outer shell, say L, gets de-excited to fill this vacancy and energy equal to the difference in the two shell-energies is released as an X-ray. It is known as an X-ray emission edge, and denoted as K_α in the example. 'K' (, L, M, ...) indicates the shell from which the electron was freed and α (, β, γ, ...) indicates the higher shell-number from which another electron made a transition to K. e.g. L_α, L_β indicate vacancies created in the L shell and subsequently filled by electrons from M and N shells, respectively. Since the values of the shell-energies are element specific, the measured X-ray intensity is dispersed in energy to identify the element.

Unlike SEM, which fathoms a few nanometres below a surface, the EDS probe can sample a volume extending to micrometres in depth to collect the X-ray signal (see Fig. D.3).

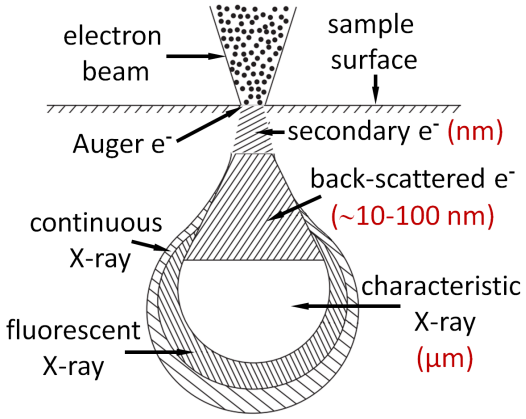

Figure D.3: **Spatial extent of interactions of an electron beam with a sample in SEM-EDS.** Higher the energy of the beam, more is the extent. SEM uses secondary and back-scattered e^-, EDS uses X-rays. Image is adapted from ref. [240].

EDS detector and signal processing[244;245]**:** Both JEOL-JSM-6500F and Zeiss-AURIGA-40 machines use thermoelectrically (Peltier) cooled 'Silicon Drift Detector' (SDD) from the Oxford Instruments.

The working mechanism of the detector involves 3 steps:
(a) Signal detection: An X-ray photon enters a silicon crystal, ionises its atoms to produce electrons. The higher energy X-rays produce higher amount of ionisation and a larger electronic signal. A preamplifier converts the electronic charge to appropriate voltage steps in time. *(b) Pulse processing:* The voltage step is measured and identified appropriately with the energy of each X-ray photon. *(c) Analyse and display:* The intensity measured is distributed over energy for displaying the spectrum. The shaping of peaks and the noise suppression is done digitally.

The 'AZtec' software interface controlled all the operations, namely selecting an area on the sample, setting acquisition parameters, displaying a corrected spectrum with identified energy levels of elements present in the sample (Fig. D.4).

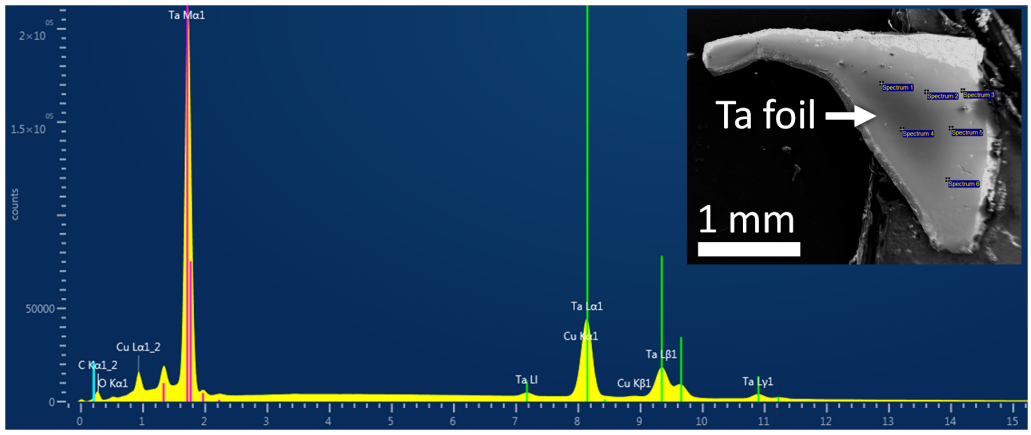

Figure D.4: **A typical EDS spectrum displayed by AZtec software.** The inset is an SEM image of a polished tantalum piece. The EDS spectrum was measured at 15 keV with a Silicon Drift Detector from locations marked as (+) on the sample. AZtec displays X-ray intensity (Y axis, counts) measured against energy (X axis, keV). The positions of pink and green lines indicate X-ray energies of M and L series for Ta, respectively. The copper peaks belong to an impurity. JEOL has a sensitivity for 0.1-0.2% of oxygen and carbon.

An accurate quantitative analysis of the spectrum is possible when the energy and current used are those for which the system has been calibrated, preferably, using the same elements of interest.

Example of SEM and EDS analysis

A Ta disc recovered from a flash-heating run conducted in argon pressure medium at 22 GPa, 3696 K is analysed for its topographic features and presence of chemical species using JEOL at as shown in Fig. D.5.

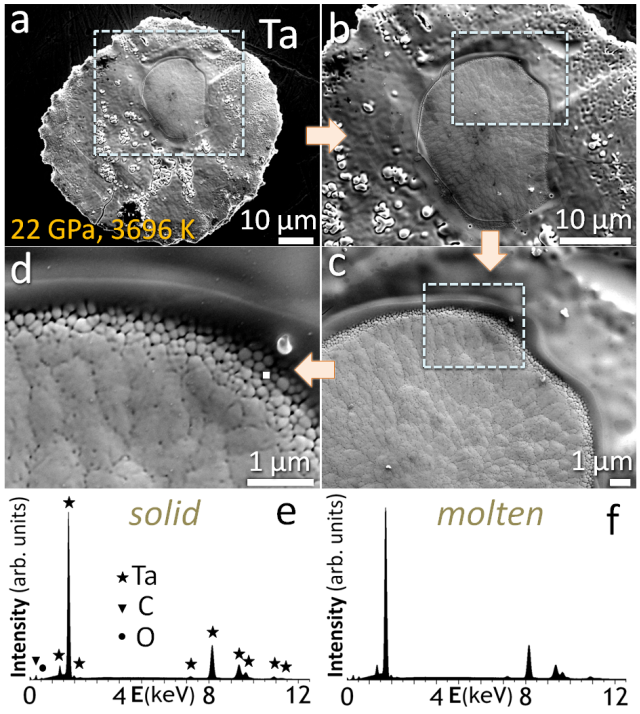

Figure D.5: **SEM images of flash-heated Ta using JEOL-JSM machine.** Area inside the dashed rectangle is magnified in the successive images. (a) Ta disc recovered from flash-heating in the DAC. (b) The heated region zoomed to compare its features with the unheated portion. (c) Outside the heated region, the rough solid texture turned smooth, most likely due to surface melting. (d) Ta restructured as grains in submicron sizes upon quenching from 3696 K. (e, f) Representative EDS spectra collected from different locations on the un-molten and molten portion, respectively. SEM and EDS are conducted at 5 keV and 15 keV, respectively.

To inspect the heated portion in detail, the view in (a) is successively magnified through (b) and (c) to about 20 times as shown in (d). The quenched liquid restructured in the form of grains of about 50-100 nm in dimension are distinctly seen in (d), in contrast to the textured rough features of the solid portion in (b) around the melt. The EDS spectra collected from the un-molten and molten portions do not differ in positions of peaks or in their relative intensities, confirming absence of any chemical alteration upon melting.

For studying melting in a diamond cell, an analysis using SEM and EDS together is a key requirement for characterising melting. These can be used to collect information from the un-molten and molten portions selectively. In contrast, in a routine X-ray diffraction technique, the X-ray beam penetrates through the thickness of the sample and generates a weak signal of diffuse scattering from a small portion of liquid, which is difficult to detect in presence of the strong diffracted signal from solid portions.

Still, drawing inferences from topographical features imaged by the SEM alone may not be sufficient for studying melting, as it could only be a surface phenomenon. To confirm melting of the bulk, the extent of melt in the depth of material needs to be imaged, which is beyond the scope of SEM. However, it is made possible by using the Focused Ion Beam Milling (see Appendix E), coupled with SEM and EDS.

Thus, the three probes - SEM, EDS and FIBM combined constitute a robust analysis of the solid-liquid transition.

——o——

Appendix E

Focused Ion Beam Technique

The Focused Ion Beam (FIB) instrument provides precision machining at sub-micrometre scale and imaging of materials at high spatial resolution on a single work platform. Locating a specific site on a sample, the FIB can remove material away or deposit another material on or simply image it, down to sub-micrometres [206;246].

Principle of operation [247;248]: An energetic beam of ions focussed onto a sample strikes the surface and loses its energy to the atoms of the sample through a variety of interactions before coming to rest.

In the inelastic type of interactions, an incident primary ion (PI) transfers its kinetic energy and momentum to the target atoms causing ionisation and subsequent emission of secondary electrons (SE), secondary ions (SI) and neutral atoms. In the elastic interactions, the target atoms get displaced from their original sites causing a damage to the sample. If the energy transferred exceeds a threshold value, the displaced atom creates defects, like a pair of interstitial atom-vacancy. The displaced atom may further knock off the neighboring atoms, depending on its recoil energy. This typically causes a cascade of independent collisions among sample atoms (see Fig. E.1). A backscattering of the PIs also takes place and its flux varies with the angle of incidence.

The effect of 'sputtering' or 'knocking the atoms off to escape the surface', caused by the PIs is used for removing the target material in a systematic and predefined pattern and is called FIB milling (FIBM). The SEs and SIs are detected by appropriate detectors located in the chamber and are processed further to produce an image of the target area.

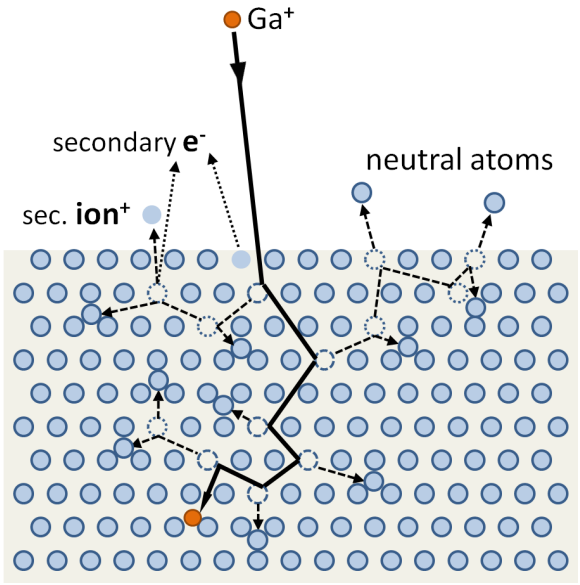

Figure E.1: **Cascade of collisions triggered by a gallium ion in the FIB technique.** Solid line: path of a Ga ion. Dashed line: path of a recoiled atom. Dotted arrow: path of a secondary electron emitted. Dashed and dotted circles: atoms recoiled by primary and secondary collision, respectively.

However, FIB imaging has a lower resolution compared to SEM imaging, because an ion beam is not as tightly focussed as an electron beam. Moreover, using FIB to image an area can cause material removal even at the lowest beam currents, which is detrimental for a sensitive sample. Hence, coupling FIBM with SEM in the same chamber facilitates machining and nondestructive imaging of the sample together.

Instrument specifications[242]**:** For the work presented in this thesis, the Zeiss-AURIGA-40 machine located at the Carnegie Institution of Washington, Washington DC, USA was used. It is coupled with SEM and EDS (Oxford Instruments) probes for efficient cut-image-analyse procedure. The instrument components are schematically shown in Fig. E.2.

Atoms from a Gallium (Ga) metal source are ionised and extracted by a high voltage 'Field Emission' process. A 2 μA beam energised to 30 keV is shaped by an electrostatic condenser lens, is corrected for aberrations / astigmatism, and focussed by an objective lens on to the sample. An aperture selects the desired probe current (1 pA - 50 nA). The sample is mounted on an electrically conducting, grounded stage. An insulating sample is either coated with graphite, gold or iridium, or it is fixed with copper / carbon conducting tapes. The stage is tilted by 54° with respect to the horizontal plane to make the sample surface perpendicular to the

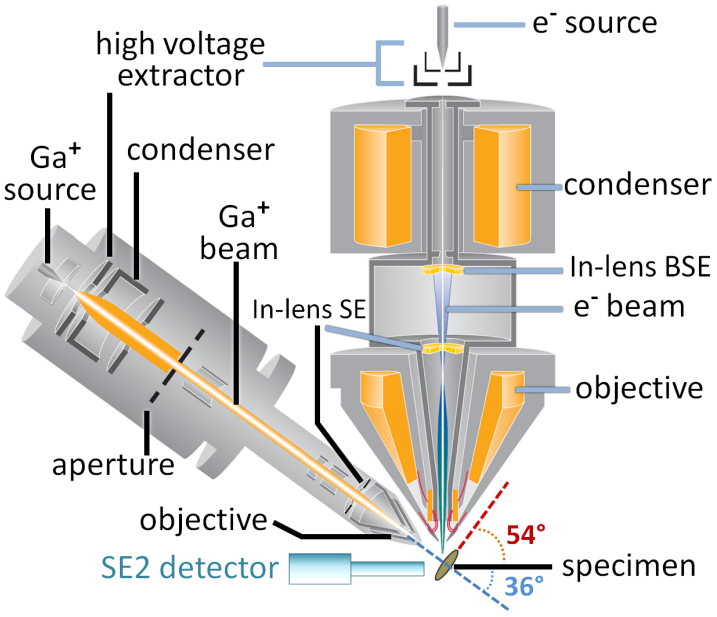

Figure E.2: **Schematics of FIB - SEM columns**
The FIB column is on the left, tilted by 54° with respect to the SEM (vertical) column. The figure is adapted from ref. [242]. See text for more description.

incident Ga ion beam. The working distance i.e. the distance between the target surface and the tip of the FIB column is 5 mm. The system vacuum is maintained better than 5×10^{-5} mbar.

The entire operation, from positioning of the sample to performing the FIBM operation and imaging is controlled by a 'smartSEM' software interface. It facilitates choosing a pattern for milling, its orientation, the order in which the material is to be removed, and selecting an appropriate current depending on the nature of the target.

The instrument is calibrated for a range of currents, namely 50, 120, 240, 600 pA and 2, 4, 16 nA. The milling current is chosen depending on the interaction cross-section of Ga with the target atom and the finesse required in the material removal. During milling, the emitted SEs are collected by the SE detectors and are processed further to produce an image of the scanned area.

In the FIB mode, a detector 'SE2' collects the SEs and sends those to a scintillator to produce photons. These photons are further guided

by a lightguide to a photomultiplier tube that converts the light to an electrical signal for imaging. An additional 'In lens' annular scintillator located inside the FIB column works on the same principle as the SE2 detector and collects the backscattered electrons in addition to SEs.

The SEM machine, operated typically at 5 keV, provides a complementary image of the same area being scanned by FIB but viewed at 36° with respect to the sample surface. It is used for inspecting the depth profiles created using FIBM. In the SEM imaging mode, the ion beam is blanked, the electron beam is active and SEs are detected and synchronised to the SEM scan. In the FIB imaging mode, the electron beam is blanked, the ion beam is active and the SE signal is detected and synchronised to the FIB scan.

The EDS probe is also coupled with this FIB facility and is used only when the SEM mode is active. The EDS probe is described in Appendix D.

FIBM operation to create cross-sections: an example of Ta

Typically, a sample is placed on a graphite or a copper tape coated with a conducting glue. However, when the unheated Ta samples (25-50 μm wide, 5-8 μm thick) were mounted that way, contributions from carbon and copper at the standard 15 keV energy of the incident electron beam were detected in the EDS spectra of Ta.

To eliminate such contributions from the substrate, Ta samples recovered from flash-heating runs were placed flat on a 100 μm thick polished Ta foil, which was fixed on a copper/aluminum stub using a conducting glue. The samples were originally prepared from the same Ta foil. A conducting silver paste spread in a minute amount around a Ta sample prevented the sample from moving and silver was not detected in EDS.

A 30 keV Ga^+ beam was used at 50 and 120 pA for fine milling (spot size ~30 nm) and at 4 nA for coarse milling (spot size ~300 nm). In Fig. E.3, FIBM operation is shown for creating depth profiles of a flash-melted Ta sample recovered from 35 GPa, 3845 K at different stages of milling.

The FIB and the SEM imaging together reveal textural features on the sample surface and in the depth. FIBM can further be used to cut, thin down and prepare a cross-section for Transmission Electron Microscopy (TEM)[206], which reveals structural information about solid and the melt, quenched from the high temperatures and recovered at 1 atm.

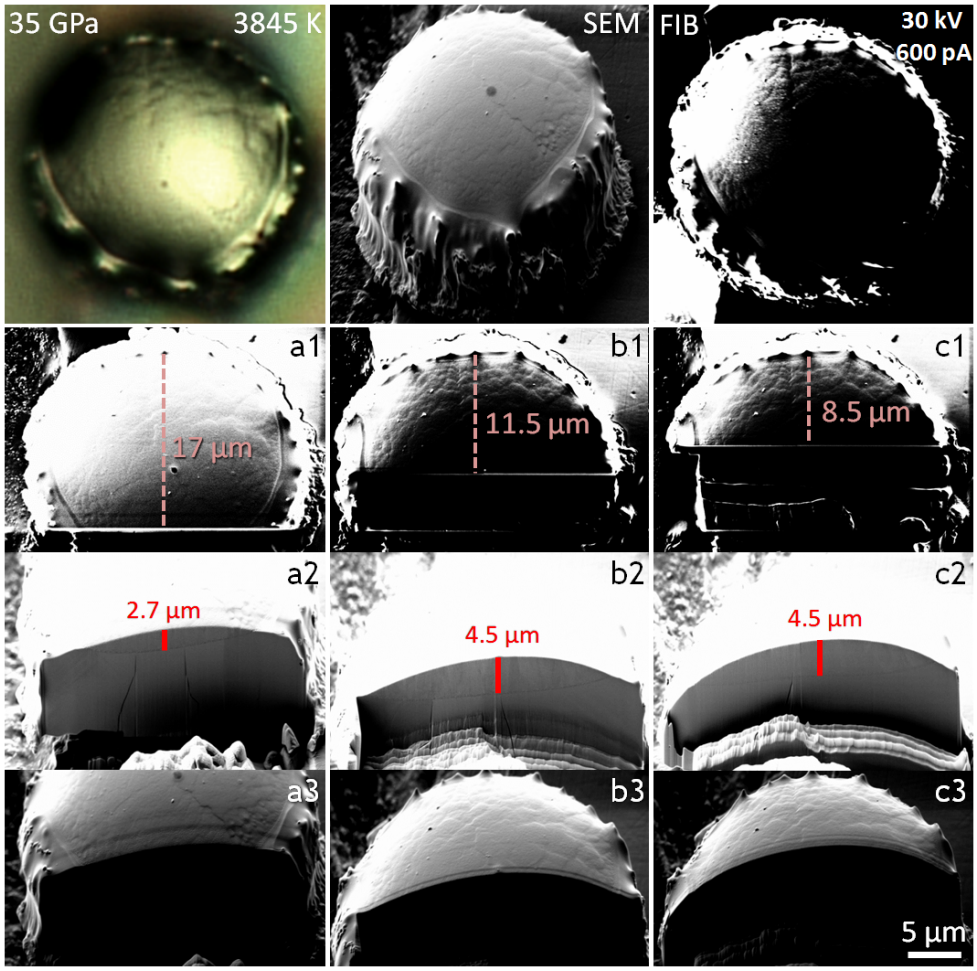

Figure E.3: **FIB milling process creating depth profiles of a Ta sample.** *Row* 1: Optical, SEM and FIB images of a flash-melted Ta disc recovered from 35 GPa and 3845 K. *Row* 2: FIB images at various stages of gradual cutting across the disc. The dashed line measures an extent of the unmilled sample. *Row* 3: SEM images of depth profiles created in row 2 and viewed at 36° with respect to the plane of the sample surface. Extent of boundaries separating the quenched melt and solid are shown with red bars. *Row* 4: SEM images of the same depth profiles in row 3, with the contrast adjusted for inspecting the surface rather than the depth profiles.

——o——

Appendix F

Quantitative analysis of melting curves

Simon-Glatzel equation

Different datasets on Ta melting are quantitatively compared by calculating pressure derivatives of the respective melting curves obtained by fitting the datasets with the empirical Simon-Glatzel (SG) equation[23]:

$$T = T_o\,(1 + (P - P_o)/a)^{1/c} \quad \text{where,}$$

T: melting temperature at pressure P. P_o, T_o: pressure and temperature of a fixed point, respectively. The fixed point can either be a triple point or the melting point at zero pressure. a: a parameter related to the internal pressure. c: a material specific constant determined experimentally.

Melt-slopes thus obtained for flash-melting and selective earlier static data are plotted in Fig. F.1. The SG equation parameters with melting temperatures and melt-slopes at 1 atm and at 295 GPa for selected static and computational studies are presented in Fig. F.2 and in Table F.1. The pressure of 295 GPa is chosen to compare the respective slopes and melting temperatures at the P-T conditions of the early shock data[137] (295 GPa, 8870±1530 K), and quantify the discrepancies. The selected data are from the early piston-cylinder experiments[185], and various LHDAC experiments[79;131;186] which have large discrepancies in their melt-slopes, including the data from flash-melting.

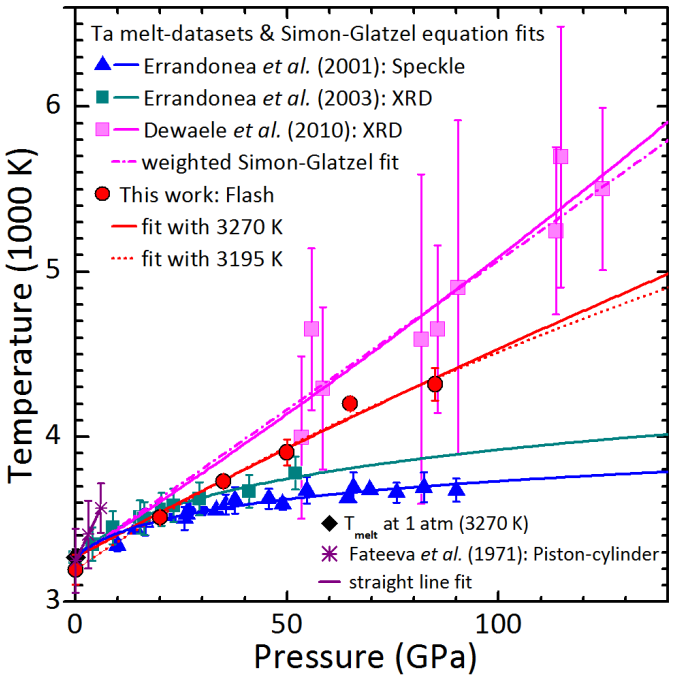

Figure F.1: **Ta melt-slopes from selective static data.** References for data: ✳[185], ▲[79], ■[186], ■[131]. The SG equation fits are extrapolated to cover the entire pressure range. See text for description.

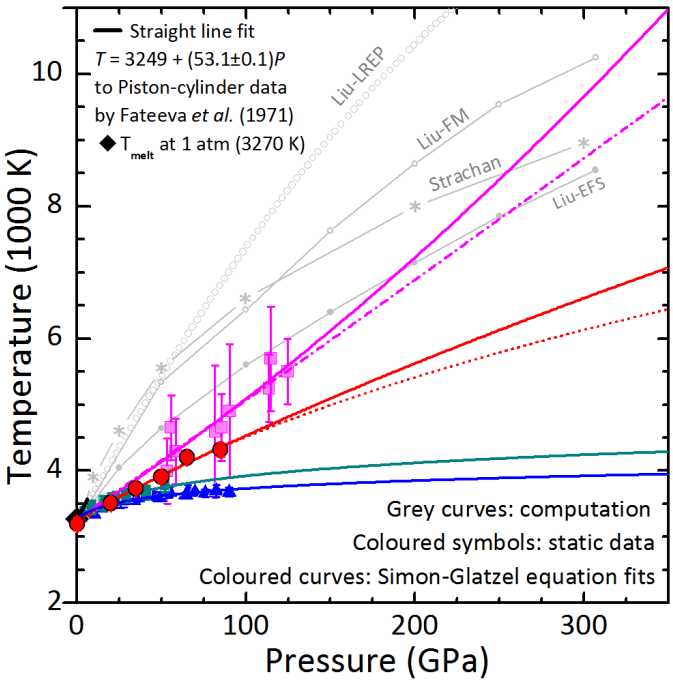

Figure F.2: **Ta melt-slopes from selective static data and computation.** The coloured curves, symbols and respective references are described in Fig. F.1. Computational curves: Coexistence phase MD simulation (LREP ○; FM —○—; EFS —●—)[193]. Vacancy formation enthalpy (—✳—)[190]. See text for more description.

Reference (Year)	1 atm T_{melt} K	1 atm $\frac{dT}{dP}$ K/GPa	295 GPa T_{melt} K	295 GPa $\frac{dT}{dP}$ K/GPa	SG equation parameters a (GPa), c
Errandonea *et al.* (2001)[79]	3270	23.5	3918	0.6	6.5±1.9, 21.3±2.6
(2003)[186]	3270	24.9	4235	1.0	9.9±2.1, 13.3±1.6
Dewaele *et al.* (2010)[131]	3270	16.5	9539	25.7	336.4±560.3, 0.6±0.9
	3270	17.8	8641	18.5	190.3±555.8, 1.0±2.3
This work (2016)[249]	3270	13.9	6567	9.5	151.7±124.3, 1.6±1.1
	3195	17.6	6101	6.6	72.4±34.1, 2.5±0.9
Strachan *et al.* (2004)[190]	3154	100.5	8932	8.7	9.1±0.4, 3.4±0.1
Liu *et al.* (2008)[193]					
MDEFS	3225	34.3	8381	11.5	43.7±2.7, 2.1±0.1
MDFM	3200	55.1	10134	14.6	26.7±2.9, 2.2±0.1
MDLREP*	3240	46.7	12362	15.1	c_1: 46.7±0, c_2: 0.1±0
Fateeva *et al.* (1971)[185]	3249	53.1			$m^{\star\star}$: 53.1±0.1

Table F.1: **Comparison of selected melt-slopes for Ta.**
The second entry for Dewaele *et al.* is a result of fitting a weighted Simon-Glatzel (SG) equation, the weight being an inverse of the total uncertainty in the melting temerature. * The parameters c_1, c_2 are obtained by fitting a polynomial $T = T_{melt} + c_1P + c_2P^2$, as a proper fit was not obtained using the SG equation. ** The slope obtained by fitting a straight line $T = T_{melt} + mP$ as the SG equation could not be fitted.

The computational studies are selected to represent the extreme ends of the entire range of slopes and melting temperatures, namely 1. Strachan[190]: the highest slope at 1 atm but the lowest slope at 295 GPa[190], 2. Liu-MDLREP[193]: the highest slope and temperature at 295 GPa, 3. Liu-MDEFS[193]: the lowest slope at 1 atm and the lowest temperature at 295 GPa. The curve Liu-MDFM[193] is the closest representation of all the shock data shown in Fig. 3.2. The shock data is not presented here to avoid cluttering of symbols.

Observations

1. The melt-slope for the data by Dewaele *et al.* is found to be rising with pressure in contrast to the behaviour of all other data and theory. Moreover, the errors in a, c are larger than the parameters themselves. To check if the large uncertainties in the data played any role in this behaviour, a weighted SG equation was fitted, with weight being inversely proportional to the uncertainty. Although the parameter values and the slope changed drastically, the variation of slope with pressure was still positive with no reduction in errors. Fitting with a second order polynomial $T = T_{melt} + c_1P + c_2P^2$ also resulted in a rising slope. Moreover, fitting with a thermodynamically derived generalised form of the SG equation, namely the Kechin equation[250] $T = T_o\ (1 + (P - P_o)/a_1)^{a_2}e^{-a_3(P - P_o)}$, where a_1, a_2, a_3 are fitting parameters, did not result in the expected behaviour.

2. For the flash-melting dataset, two fits are presented. One for T_o = 3270 K, the known melting temperature at 1 atm and the second for T_o = 3195 K, the melting temperature obtained in this work at 1 atm. The relative errors in a and c are drastically reduced for the latter. However, the overall uncertainty in the parameters is still 35-50%, in spite of the tight bracketing of the data.

3. For the data by Errandonea *et al.*, the melt-slopes at higher pressures approached near zero values but at 1 atm yielded the highest values among the selected DAC studies.

4. The data by Fateeva *et al.* was fitted with a straight line as it could not be fitted with the SG equation, perhaps due to insufficient data.

Discussion

Although empirical in nature, the SG equation was derived by Salter[251] and Gilvarry[252] from the Grüneisen equation of state[10] and the Lindemann melting formula. They showed[253] that

$$c = (6\gamma_{m_o} + 1)/(6\gamma_{m_o} - 2) \quad \text{where,}$$

c: SG equation parameter. γ_{m_o}: Grüneisen parameter[§] corresponding to the melting temperature at 1 atm. Moreover, comparing[254] the SG equation in differential form with the Clausius-Clapeyron equation, one obtains

$$c\, a = H/\delta V \quad \text{where,}$$

H: heat of fusion, and δV: volume difference between the solid and liquid phases at melting. Thus, if H and δV are measured, values of a and c are constrained as per the above equation, allowing more reliable evaluation of c and subsequently, that of γ. However, since no measurements on δV are available for tantalum even at 1 atm, in this work, the fitting parameters a and c are left unconstrained. This could perhaps lead to the unreasonable nature of melt-slopes and large errors in the parameters for the data by Dewaele and to some extent for the flash-melting data.

An overall assessment of this exercise suggests that an alternate independent description of the data is required. The Grüneisen parameter relates thermal expansion of a material to its bulk modulus, and is an important entity in reducing[255] the P-V shock data for comparing with static studies at 300 K. Since the SG equation allows to calculate γ, it is reasonable to compare γ obtained from alternate independent formulations, especially those involving the bulk modulus. One such formulation is discussed ahead. In Table F.2, γ_{m_o} evaluated from the SG equation for different datasets are listed for further quantitative analysis and the evaluated δV are documented for any future verification by measurements.

[§] $\gamma = V \frac{\partial P}{\partial E}\big|_V = \frac{\alpha_v B_T}{\rho C_P} = \frac{\alpha_v B_S}{\rho C_V}$ where V: volume at pressure P. E: internal energy. α_v: coefficient of volume thermal expansion. B_T, B_S: isothermal and adiabatic bulk modulus, resp. C_P, C_V: Specific heat capacities at constant P and V, resp. ρ: density.

Gilvarry-Vaidya-Rajagopal (GVR) equation

The Grüneisen parameter γ can be evaluated independently from the dependence of melting temperature on the isothermal compression of the material. An empirical equation by Kraut and Kennedy[25;26] relates normalised melting temperatures to isothermal compressions at 300 K as

$T/T_o = 1 + c\,(\Delta V/\,V_o)$ where,

$\Delta V/\,V_o$: isothermal compression. V_o: volume at 1 atm, 300 K. $\Delta V = V - V_o$, V: volume at pressures above 1 atm, and at 300 K. T, T_o: melting temperatures expressed in °C at pressures corresponding to volumes V and V_o, respectively. c: material specific constant.

This empirical relation was later derived by Gilvarry[11] and independently by Vaidya and Raja Gopal[256] in a more useful form that allowed to calculate γ. For isothermal compressions less than 0.4, they derived the following relation from the Lindemann's equation and volume dependence of γ.

$T/T_o = 1 + s\left|\Delta V/\,V_o\right|$ where,

T, T_o: melting temperatures expressed in K at pressures corresponding to volumes V and V_o at 1 atm, respectively. $s = 2(\gamma_o - (1/3))$, γ_o = Grüneisen parameter at 1 atm, 300 K. Thus, γ_o can be obtained from a plot T/T_o vs. $\Delta V/V_o$ by fitting a straight line with intercept 1 and learning the slope s.

In this work, to calculate ΔV over the pressure range covering all datasets, Ta volumes at different pressures at 300 K are obtained by fitting the P-V data from Cynn *et al*. (1999)[203] using the 3rd order Birch Murnaghan EOS. To obtain P-V relation, Cynn's XRD work is preferred over other studies because 1. it covers the highest pressure range (1 atm – 174 GPa), 2. the bulk modulus B_o = 195 GPa calculated at 1 atm using the 3^{rd} order Birch-Murnaghan equation is in an excellent agreement with that obtained from ultrasonic measurements (194 GPa)[257] and from the reduced shock wave data (194 GPa)[258], 3. further refinements[232;259] using advanced experimental probes and Vinet equation of state are within the calculated uncertainties of their results.

Discussion

A plot of T/T_o vs. $\Delta V/V_o$ for the selected datasets with T_o = 3270 K is shown in Fig. F.3. The GVR equation is applicable here as the data is well within the compression of 0.4. The respective slopes and γ_o calculated are listed in Table F.2 for comparing with γ_{m_o} obtained from the SG equation.

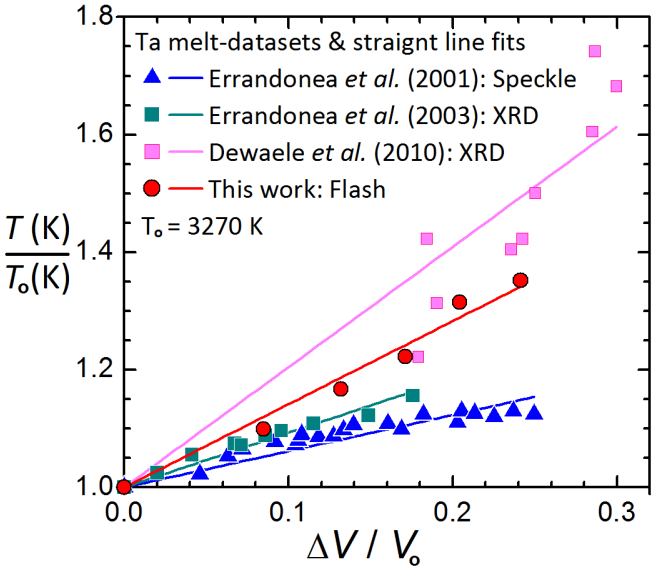

Figure F.3: **Selective LH-DAC data on Ta fitted with GVR equation.** References for data: ▲[79], ■[186], ■[131]. See text for description.

Cynn calculated γ_o = 1.639 using the following values: B_s = 196 GPa[257], C_p = 0.14 J/g/K[260], ρ = 16.65 g/cc using molar volume = 10.865 cc/mol[260], and $\alpha_v = 1.95 \times 10^{-5}$/K[260]. Most of the theoretical calculations available on Ta use this value for either deriving other entities or for comparison. However, in the older literature, a variation from 0.31 (from shock data) to 1.82 (from C_v) has been reported[261].

In Grüneisen's theory[10], γ is assumed to be independent of temperature. However, later theoretical and experimental investigations[262–264] at constant pressure revealed a temperature dependence in some cases. For Ta, computational studies[189;265] have shown 13-27% decrease in γ from values (> 2) at 300 K to values (> 1.7) at 3270 K. However, these values at 300 K are substantially higher compared to those obtained from various measurement based evaluations[266] of γ ranging from 1.39 to 1.80. As measurements on the relevant entities, e.g. C_p, C_v, α_v at 3270 K are

unavailable, value of γ is not known, preventing any verification. With pressure, γ is shown[189;192;265;267] to decrease but again, there is a large variation in its value and the functional form.

In Table F.2, a comparison of γ evaluated at 300 K and at 3270 K from two independent equations shows that for the data by Errandonea *et al.*, γ decreases by 44% and 54% with temperature with values too low compared to the standard value (1.64). In case of Dewaele *et al.*, the unreliability in c, as discussed earlier, is manifested with a negative and therefore, an unacceptable value of γ_{m_o}. However, the value of γ_o obtained from the GVR equation is close the standard value.

	SG	GVR	γ_{m_o}	γ_o	$\delta V = \frac{H}{ac}$
Reference	c	s	$\frac{2c+1}{6(c-1)}$	$\frac{s}{2}+\frac{1}{3}$	(cc/mol)
Errandonea *et al.*					
(2001)[79]	21.3±2.6	0.62±0.02	0.36±0.00	0.64 ±0.01	0.266
(2003)[186]	13.3±1.6	0.93±0.03	0.37±0.01	0.80±0.02	0.279
Dewaele *et al.*					
(2010)[131]	90.6±0.9	2.05±0.12	-0.92±0.6	1.36±0.06	0.181
This work					
3270 K	1.6±1.1	1.25±0.06	1.17±0.65	0.96±0.03	0.151
3195 K	2.5±0.9	1.41±0.05	0.67±0.31	1.04±0.03	0.202

Table F.2: **Grüneisen parameters and volume change at melting evaluated from Simon-Glatzel (SG) and Gilvarry-Vaidya-Raja Gopal (GVR) equations.**
s: slope of a straight line fitted to melt-data plotted as normalised temperatures $T(\mathrm{K})/T_o(\mathrm{K})$ vs. isothermal compression $\Delta V/V_o$ at 300 K as shown in Fig. F.3. γ_{m_o}: evaluated at melting temperature at 1 atm. γ_o: evaluated at 300 K, 1 atm. δV: volume change at melting. H: latent heat of fusion at 1 atm = 36.57 kJ/mol[268;269].

For the flash-data, γ_{m_o} values are much lower than 1.64. Contrary to the theoretical investigations[189;265], γ_{m_o} and γ_o values are consistent

with each other within the uncertainty, supporting the original assumption by Grüneisen. If γ indeed depends on temperature, it suggests an inadequate description of the data by SG or GVR equations.

In summary, the Grüneisen parameters obtained from the Simon-Glatzel equation and the Gilvarry-Vaidya-Raja Gopal equation are not consistent with the accepted value. A likely explanation is that these equations do not provide satisfactory descriptions of the melt-data for Ta, suggesting a need for a better theoretical formulation to explain the same.

Relevance of a melt-slope and its relation to compressibility

A theory of melting predicts the slope $\frac{dT}{dP}$ at a given pressure in terms of certain physical quantities, which are required to be measured in order to validate the theory. A part of validation is to measure the melting temperatures directly as a function of pressure. Due to extreme difficulties in measuring the relevant physical quantities at high P-T conditions, relatively easier measurements at ambient conditions are preferred for comparison. A melt-slope at 1 atm ($\frac{dT}{dP}\big|_{P=0}$) thus becomes useful.

Since $\frac{dT}{dP}\big|_{P=0}$ is obtained by fitting an appropriate equation to the LH-DAC data and differentiate it with respect to pressure, melting behaviour of materials in the higher pressure regime contributes to it. Although a solid-solid phase transition with pressure is many times manifested as a change in the melt-slope, within a given phase, the gradual change in the slope is likely related to the compressibility[§] of the material.

The relation between a melt-slope and compressibility has been explored mainly by Gilvarry[252;253] and Stacey[270]. By combining the laws by Lindemann and Grüneisen[†] with Clapeyron equation, Gilvarry derived[252;271] an expression relating a melt-slope to compressibility as follows.

[§]Compressibility C = 1/bulk modulus = $-\frac{1}{V}\frac{dV}{dP}$

[†]Grüneisen law: Ratio of the thermal expansion coefficient to the specific heat at constant volume is a constant at all temperatures for isotropic metals.

$\frac{1}{T_{m_o}} \left.\frac{dT_m}{dP}\right|_{P=0} = 2(\gamma_{m_o} - \frac{1}{3}) \frac{C_{m_o}}{q_{m_o}}$ where,

All the quantities are either measured or evaluated at the melting temperature and at zero pressure, as indicated by suffix m and o, respectively. T_m: melting temperature at pressure P. γ: Grüneisen parameter. C: compressibility. q: $(1 + \gamma C_v T \frac{\delta V}{H V})^{-1}$ where, C_v: heat capacity at constant volume, δV: volume change at melting, H: latent heat of fusion. A similar equation was derived by Stacey. With appropriate assumptions and approximations, $q \to 1$ and the above equation reduces to the well known differential form of Lindemann's equation.

Thus, the factor $2(\gamma_{m_o} - \frac{1}{3})/q_{m_o}$ dictates the dependence of a normalised melt slope on compressibility at the conditions of melting. As all the quantities on the right hand side of the equation are a function of temperature and are difficult to measure at melting, an experimental verification of the above equation is difficult as well. However, with a hope that exploring this dependence at 1 atm, 300 K be instructive and may lead to an insight in the behaviour of materials regarding compressibility and melt-slopes, a study on selected metals is carried out as follows.

To investigate if there is any systematic dependence of melt-slopes on the compressibility, melt-slopes for selected metals were obtained by fitting the SG equation to the available LHDAC melt-data. The compressibility values at 1 atm and 300 K were obtained from a standard reference of Materials Handbook[268] and were checked for consistency either with other handbooks or with the respective values of isothermal bulk moduli obtained from a P-V equation of state.

Selective metals, their phases at melting, pressure ranges in which data is available, ambient melting temperatures, melt slopes and compressibility are presented in Table F.3. Metals with an unresolved high discrepancy in their ambient melt slopes obtained from different datasets are excluded, e.g. Pt[272;273], Ni[79;81;274;275]. For Ta, although many datasets exist, only the two yielding the extreme slopes are presented. Metals, for which melt-slopes from different datasets differ negligibly, are represented by one of the datasets, e.g. for Co, melt-slopes from Lazor *et al.* (1994)[274] and Errandonea *et al.* (2001)[79] are represented by the slope from Lazor *et al.* For metals having difference phases at 300 K and at melting, compressibility at 300 K is nevertheless used, e.g. at ambient conditions, Co, Fe, Ti have hcp, bcc (α), and hcp phases, respectively but

these melt from fcc, bcc, bcc phases, respectively.

When these melt slopes were normalised with ambient melting temperatures and plotted against the individual compressibility at ambient conditions (Fig. F.4), certain systematics emerged.

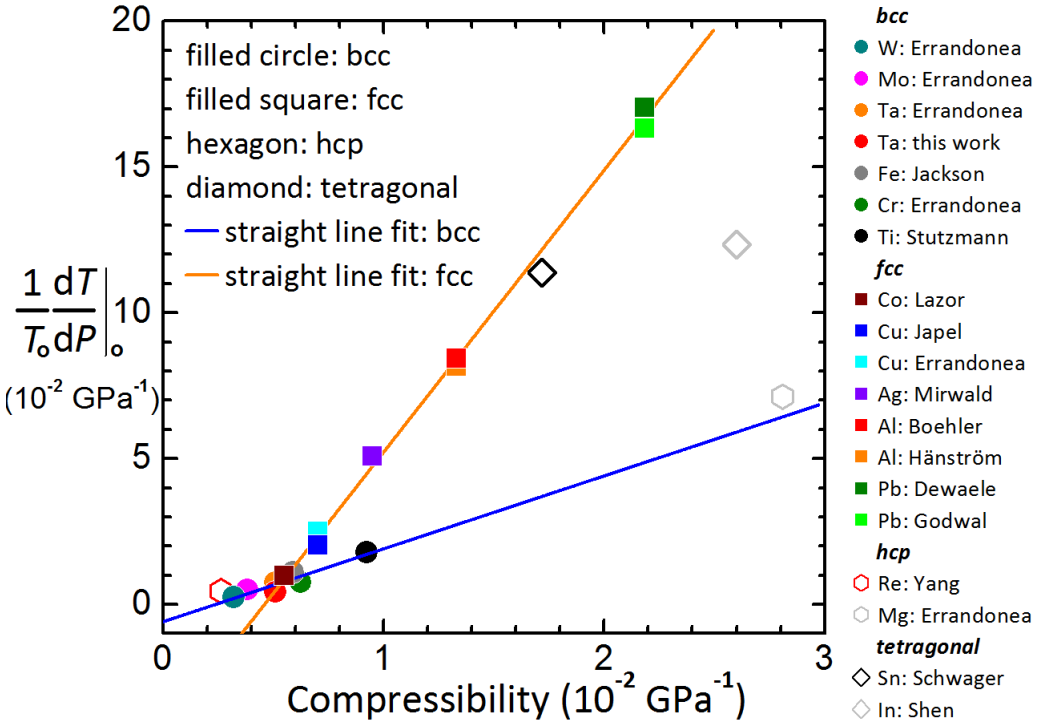

Figure F.4: **Plot of normalised melt-slopes vs. compressibility for 15 metals.**
C_o: Isothermal compressibility at zero pressure and 300 K. T_o: Melting temperature at 1 atm. $\frac{dT}{dP}\Big|_{P=0}$: Melt-slope at zero pressure. For metals that melt from bcc or fcc phases, a linear correlation between the normalised slope and compressibility seems to exist. The references for data are specified in Table F.3. See text for more description.

Observations

1. For metals that melt from fcc or bcc phases, a linear correlation appears to exist between the normalised slope and compressibility. The

	Phase at T_m	P range GPa	C_o GPa^{-1}	T_o K	$\frac{dT}{dP}\big\|_{P=0}$ K/GPa	Reference
Re	hcp	10-47.4	0.264	3458	15.80	Yang *et al.* (2012)[204]
W	bcc	11.8-91.1	0.321	3687	8.89	Errandonea *et al.* (2001)[79]
Mo	bcc	8.5-89.1	0.383	2870	21.13	Errandonea *et al.* (2001)[79]
Ta	bcc	4-52	0.509	3270	24.87	Errandonea *et al.* (2003)[186]
	”	20-85	”	”	13.91	This work (2016)[249]
Co	fcc	9.7-99.7	0.551	1765	17.61	Lazor *et al.* (1994)[274]
Fe[§]	bcc	20-82	0.589	1808	19.81	Jackson *et al.* (2013)[62]
Cr	bcc	7.3-63.2	0.624	2162	19.77	Errandonea *et al.* (2001)[79]
Cu	fcc	16.4-98	0.702	1358	27.62	Japel *et al.* (2005)[81]
	”	7.4-47.7	”	”	33.83	Errandonea *et al.* (2013)[273]
Ti	bcc	47-75.8	0.923	1941	34.75	Stutzmann *et al.* (2015)[276]
Ag	fcc	0.5-6	0.949	1235	63.98	Mirwald *et al.* (1979)[277]
Al	fcc	27.5-77	1.330	935	76.40	Boehler *et al.* (1997)[117]
	”	12.1-49.3	”	”	78.90	Hänström *et al.* (2000)[116]
Sn	tetra[†]	16.8-37	1.718	505	57.51	Schwager *et al.* (2010)[83]
Pb	fcc	9.5-97.4	2.183	601	102.44	Godwal *et al.* (1990)[278]
	”	28.5-80.6	”	”	98.08	Dewaele *et al.* (2007)[93]
In	tetra[†]	1.1-2.6	2.600	430	53.06	Shen *et al.* (2001)[91]
Mg	hcp	4.0-45	2.809	922	65.72	Errandonea *et al.* (2001)[80]

Table F.3: **Compressibility and melt-slopes for selected elements.** T_o: melting temperature at 1 atm[268;269]. C_o: compressibility at 1 atm, calculated from bulk modulus[268;269]. $\frac{dT}{dP}\big|_{P=0}$: obtained by fitting the SG equation to the LHDAC melt-data in the P range from the cited reference. Phase at T_m: phase from which a metal melts at temperature T_m at pressures from 1 atm to the extreme of the P range. [§] Fe is an exception as it melts from bcc phase at 1 atm but it melts from fcc phase in the P range of the dataset listed. [†] Tetragonal. See text for more discussion.

straight line fitted to bcc metals has slope 2.50±0.45 with -0.0059±0.0027 as the intercept. For fcc metals, the slope is 9.67±0.21 and the intercept -0.0445±0.0030.

2. For metals that melt from hcp, drawing an inference is not possible as data only for Re and Mg is available. If a linear correlation is speculated for hcp metals, an interesting observation is noteworthy. Co and Ti are plotted as fcc and bcc metals, respectively as those are the phases at melting. However, both metals have hcp structure at 300 K. Co undergoes hcp → fcc transition at about 695 K[279] while Ti undergoes hcp → bcc transition at about 1150 K[280]. As the compressibility at 300 K is plotted, which is related to hcp phase rather than the phases at melting, Re, Co, Ti and Mg together seem to share a liner correlation.

3. For metals that melt from tetragonal phase, drawing an inference is not possible as data only for Sn and In is available. The data for In is from an externally heated DAC and not from a laser heated DAC, It is nevertheless plotted for the purpose of documentation. Moreover, the slope for In may not be reliable as only three melting points are reported[91] within 1.1 to 2.6 GPa, which is too short a pressure range for a reliable curve fitting. Interestingly, an observation similar to that for Co and Ti can be noted for Sn as well. Although Sn melts from tetragonal (white, β) phase, it is in diamond cubic (gray, α) phase below 291 K[280], which is close to 300 K. The diamond cubic structure is also visualised as two interpenetrating fcc unit cells. This could be related to Sn being very close to the straight line fit to fcc metals on the plot.

4. Although a large dispersion in melt-slopes exists for Fe, a recent dataset[62] yielding a melt-slope close to some of the earlier data is plotted for the purpose of documentation. Fe, at 1 atm, undergoes a sequence of transitions bcc (α) → fcc (γ) → bcc (δ) with temperature and melts from bcc (δ) phase[280]. Hence, it is listed as bcc in Table F.3. However, it melts from fcc phase from about 5 GPa to 100 GPa, including the pressure range of the dataset presented here. There is no change in slope at the bcc → fcc transition with pressure. Interestingly, Fe is located close to the intercept of the two straight lines fitted to fcc and bcc metals.

Assessment

The linear correlation between the normalised melt-slope and compressibility obtained in this investigation would have been numerically useful if the intercepts of straight lines were close to zero. Then, the slopes would directly yield the factor $2(\gamma_{m_0} - \frac{1}{3})/q_{m_0}$ and one could obtain q knowing the Grüneisen parameter at ambient condition or vice versa. If these values agreed with the available values in literature, the applicability of the Gilvarry equation at ambient temperature would be validated.

The current investigation is therefore limited to a qualitative analysis describing the trend of the correlation. Knowing the compressibility of a metal at the ambient conditions, which is often evaluated from the P-V data, the melt-slope at ambient pressure can be approximately predicted for new melting temperature measurements on fcc and bcc metals. It would also be instructive to study the behaviour of nonmetals with bcc and fcc phases at melting in order to probe any contribution of the metallic nature in the present investigation.

——o——

Bibliography

[1] P. Bridgman, *Water, in the liquid and five solid forms, under pressure*, Proceedings of the American Academy of Arts and Sciences **47**, 441 (1912). Cited on 13.

[2] J. Davis, in *ASM speciality handbook: Heat-resistant materials*, edited by J. Davis (ASM International, 1997), chap. 1, pp. 3–30, ISBN 978-0-87-170596-9. Cited on 13.

[3] Y. Wei, M. Fraenz, E. Dubinin, J. Woch, H. Lühr, W. Wan, Q. Zong, T. Zhang, Z. Pu, S. Fu, et al., *Enhanced atmospheric oxygen outflow on Earth and Mars driven by a corotating interaction region*, Journal of Geophysical Research: Space Physics **117**, A03208 (2012). Cited on 13.

[4] F. Busse, in *Encyclopedia of solid Earth geophysics*, edited by H. Gupta (Springer, 2011), pp. 394–401, ISBN 978-90-481-8701-0. Cited on 13.

[5] R. Boehler, *High-pressure experiments and the phase diagram of lower mantle and core materials*, Reviews of Geophysics **38**, 221 (2000). Cited on 13, 17, 29, 32, and 35.

[6] B. Fagley, in *Practical chemical thermodynamics for geoscientists*, edited by B. J. Fagley and R. Osborne (Academic Press, 2013), chap. 7, pp. 225–286, 1st ed., ISBN 978-0-12-251100-4. Cited on 14.

[7] H. Callen, *Thermodynamics and an introduction to thermostatistics* (John Wiley & Sons, Inc., 2005), 2nd ed., ISBN 9812-53-185-8. Cited on 14.

[8] D. Heinz and R. Jeanloz, *Measurement of the melting curve of $Mg_{0.9}Fe_{0.1}SiO_3$ at lower mantle conditions and its geophysical implications*, Journal of Geophysical Research **92**, 11437 (1987). Cited on 14, 21, 34, and 39.

[9] F. Lindemann, *Über die Berechnung molekularer Eigenfrequenzen*, Physikalische Zeitschrift **11**, 609 (1910). Cited on 14.

[10] E. Grüneisen, *Theorie des festen Zustandes einatomiger Elemente*, Annalen der Physik **344**, 257 (1912). Cited on 14, 117, and 119.

[11] J. Gilvarry, *Lindemann and Grüneisen laws and a melting law at high pressure*, Physical Review Letters **16**, 1089 (1966). Cited on 14 and 118.

[12] W. Braunbek, *Zur Gitterdynamik des Schmelzvorganges*, Zeitschrift für Physik **38**, 549 (1926). Cited on 14.

[13] N. Raschevsky, *Zur Theorie der Schmelzwärmen*, Zeitschrift für Physik **40**, 214 (1927). Cited on 14.

[14] K. Herzfeld and M. Mayer, *On the theory of fusion*, Physical Review **46**, 995 (1934). Cited on 14.

[15] J. Lennard-Jones and A. Devonshire, *Critical and co-operative phenomena III - A theory of melting and the structure of liquids*, Proceedings of the National Academy of Sciences of the United States of America **169**, 317 (1938). Cited on 14.

[16] W. Bragg and E. Williams, *Effect of thermal agitation on atomic arrangement in alloys*, Proceedings of the Royal Society of London A **145**, 699 (1934). Cited on 14.

[17] W. Bragg and E. Williams, *The effect of thermal agitation on atomic arrangement in alloys-II*, Proceedings of the Royal Society of London A **151**, 540 (1935). Cited on 14.

[18] L. Brillouin, *On thermal dependence of elasticity in solids*, Physical Review **54**, 916 (1938). Cited on 14.

[19] M. Born, *Thermodynamics of crystals and melting*, The Journal of Chemical Physics **7**, 591 (1939). Cited on 15 and 26.

[20] A. Lazicki, Y. Fei, and R. Hemley, *High-pressure differential thermal analysis measurements of the melting curve of lithium*, Solid State Communications **150**, 625 (2010). Cited on 15.

[21] E. Clapeyron, *Memoir on the motive power of heat*, Journal de l'Ecole Royale Polytechnique **14**, 153 (1834). Cited on 16.

[22] R. Clausius, *On the moving force of heat, and the laws regarding the nature of heat itself which are deducible therefrom*, Philosophical Magzine and Journal of Science **2**, 1 (1851). Cited on 16.

[23] F. Simon and G. Glatzel, *Bemerkungen zur Schmelzdruckkurve*, Zeitschrift für anorganische und allgemeine Chemie **178**, 309 (1929). Cited on 16, 78, and 113.

[24] F. Simon, *On the range of stability of the fluid state*, Transactions of the Faraday Society **33**, 65 (1937). Cited on 16.

[25] E. Kraut and G. Kennedy, *New melting law at high pressures*, Physical Review Letters **609**, 608 (1966). Cited on 16 and 118.

[26] E. Kraut and G. Kennedy, *New melting law at high pressures*, Physical Review **151**, 668 (1966). Cited on 16 and 118.

[27] S. Mizushima, *Dislocation model of liquid structure*, J. Phys. Soc. Jpn **15**, 70 (1960). Cited on 16.

[28] J. Poirier, *Dislocation-mediated melting of iron and the temperature of the Earths core*, Geophysical Journal of Royal Astronomical Society **85**, 315 (1986). Cited on 16.

[29] B. Joos, in *Dislocations in solids*, edited by F. Nabarro and M. Duesberry (Elsevier, 1996), pp. 505–587. Cited on 16.

[30] C. Guillaume, E. Gregoryanz, O. Degtyareva, M. McMahon, M. Hanfland, S. Evans, M. Guthrie, S. Sinogeikin, and H. Mao, *Cold melting and solid structures of dense lithium*, Nature Physics **7**, 211 (2011). Cited on 16.

[31] W. Nellis, *Dynamic compression of materials: Metallization of fluid hydrogen at high pressures*, Reports on Progress in Physics **69**, 1479 (2006). Cited on 16, 27, 28, and 35.

[32] T. Kunimoto and T. Irifune, *Pressure generation to 125 GPa using a 6-8-2 type multianvil apparatus with nano-polycrystalline diamond anvils*, Journal of Physics: Conference Series **215**, 012190 (2010). Cited on 17.

[33] K. Hirose, Y. Fei, Y. Ma, and H. Mao, *The fate of subducted basaltic crust in the Earth's lower mantle*, Nature **397**, 53 (1999). Cited on 17.

[34] D. Frost, B. Poe, R. Trønnes, C. Liebske, A. Duba, and D. Rubie, *A new large-volume multianvil system*, Physics of the Earth and Planetary Interiors **143-144**, 507 (2004). Cited on 17.

[35] J. Xu, J. Yen, Y. Wang, and E. Huang, *Ultrahigh pressures in gem anvil cells*, High Pressure Research **15**, 127 (1996). Cited on 17.

[36] K. Furuno, A. Onodera, and S. Kume, *Sapphire-anvil cell for high pressure research*, Japanese Journal of Applied Physics **25**, L646 (1986). Cited on 17.

[37] J. Xu and H. Mao, *Moissanite: A window for high-pressure experiments*, Science (New York, N.Y.) **290**, 783 (2000). Cited on 17.

[38] J. Xu, H. Mao, R. Hemley, and E. Hines, *The moissanite anvil cell: a new tool for high-pressure research*, Journal of Physics: Condensed Matter **14**, 11543 (2002). Cited on 17.

[39] D. Schiferl, *Temperature compensated high-temperature/high-pressure Merrill-Bassett diamond anvil cell*, Review of Scientific Instruments **58**, 1316 (1987). Cited on 17.

[40] N. Dubrovinskaia and L. Dubrovinsky, *Whole-cell heater for the diamond anvil cell*, Review of Scientific Instruments **74**, 3433 (2003). Cited on 17.

[41] M. Moore, D. Sorensen, and R. DeVries, *A simple heating device for diamond anvil high pressure cells*, Review of Scientific Instruments **41**, 1665 (1970). Cited on 17.

[42] L. Dubrovinsky, S. Saxena, F. Tutti, S. Rekhi, and T. Le Bihan, *In-situ X-ray study of the thermal expansion of iron at multimegabar pressure*, High Temperatures - High Pressures **31**, 553 (1999). Cited on 17.

[43] S. Pasternak, G. Aquilanti, S. Pascarelli, R. Poloni, B. Canny, M. Coulet, and L. Zhang, *A diamond anvil cell with resistive heating for high pressure and high temperature X-ray diffraction and absorption studies*, Review of Scientific Instruments **79**, 085103 (2008). Cited on 17.

[44] Z. Du, L. Miyagi, G. Amulele, and K. K. M. Lee, *Efficient graphite ring heater suitable for diamond-anvil cells to 1300 K*, Review of Scientific Instruments **84**, 024502 (2013). Cited on 17.

[45] Z. Jenei, H. Cynn, K. Visbeck, and W. Evans, *High-temperature experiments using a resistively heated high-pressure membrane diamond anvil cell*, Review of Scientific Instruments **84**, 095114 (2013). Cited on 17.

[46] L. Liu and W. Bassett, *The melting of iron up to 200 kbar*, Journal of Geophysical Research **80**, 3777 (1975). Cited on 17 and 19.

[47] R. Boehler, M. Nicol, C. Zha, and M. Johnson, *Resistance heating of Fe and W in diamond-anvil cell*, Physica B+C **139140**, 916 (1986). Cited on 17.

[48] A. Goncharov and J. Crowhurst, *Raman spectroscopy under extreme conditions*, Journal of Low Temperature Physics **139**, 727 (2005). Cited on 17.

[49] C. Zha and W. Bassett, *Internal resistive heating in diamond anvil cell for in situ X-ray diffraction and Raman scattering*, Review of Scientific Instruments **74**, 1255 (2003). Cited on 17.

[50] S. Weir, D. Jackson, S. Falabella, G. Samudrala, and Y. Vohra, *An electrical microheater technique for high-pressure and high-temperature diamond anvil cell experiments*, Review of Scientific Instruments **80**, 013905 (2009). Cited on 17 and 19.

[51] S. Tateno, K. Hirose, Y. Ohishi, and Y. Tatsumi, *The structure of iron in Earth's inner core*, Science **330**, 359 (2010). Cited on 17.

[52] L. Benedetti and P. Loubeyre, *Temperature gradients, wavelength dependent emissivity, and accuracy of high and very-high temperatures*

measured in the laser-heated diamond cell, High Temperature-High Pressure **24**, 423 (2004). Cited on 17.

[53] J. Lin, M. Santoro, V. Struzhkin, H. Mao, and R. Hemley, *In situ high pressure-temperature Raman spectroscopy technique with laser-heated diamond anvil cells*, Review of Scientific Instruments **75**, 3302 (2004). Cited on 17.

[54] A. Goncharov, *Raman spectroscopy at high pressures*, International Journal of Spectroscopy **2012**, 617528 (2012). Cited on 17, 26, and 27.

[55] A. Polian, *Brillouin scattering at high pressure: An overview*, Journal of Raman Spectroscopy **34**, 633 (2003). Cited on 17 and 26.

[56] S. Sinogeikin, J. Bass, and T. Katsura, *Single-crystal elasticity of ringwoodite to high pressures and high temperatures : implications for 520 km seismic discontinuity*, Physics of the Earth and Planetary Interiors **136**, 41 (2003). Cited on 17.

[57] S. Sinogeikin, J. Bass, V. Prakapenka, D. Lakshtanov, G. Shen, C. Sanchez-Valle, and M. Rivers, *Brillouin spectrometer interfaced with synchrotron radiation for simultaneous X-ray density and acoustic velocity measurements*, Review of Scientific Instruments **77**, 103905 (2006). Cited on 17.

[58] L. Ming and W. Bassett, *Laser heating in the diamond anvil press up to 2000 °C sustained and 3000 °C pulsed at pressures up to 260 kbars*, Review of Scientific Instruments **45**, 1115 (1974). Cited on 18.

[59] R. Boehler and K. De Hantsetters, *New anvil designs in diamond-cells*, High Pressure Research **24**, 391 (2004). Cited on 18.

[60] R. Boehler, *New diamond cell for single-crystal X-ray diffraction*, Review of Scientific Instruments **77**, 115103 (2006). Cited on 18, 19, 37, 47, 67, and 89.

[61] A. Campbell, *Measurement of temperature distributions across laser heated samples by multispectral imaging radiometry*, Review of scientific instruments **79**, 015108 (2008). Cited on 18.

[62] J. Jackson, W. Sturhahn, M. Lerche, J. Zhao, T. Toellner, E. Alp, S. Sinogeikin, J. Bass, C. Murphy, and J. Wicks, *Melting of compressed iron by monitoring atomic dynamics*, Earth and Planetary Science Letters **362**, 143 (2013). Cited on 18, 25, 30, 34, 124, and 125.

[63] G. Aquilanti, A. Trapananti, A. Karandikar, I. Kantor, C. Marini, O. Mathon, S. Pascarelli, and R. Boehler, *Melting of iron determined by X-ray absorption spectroscopy to 100 GPa*, Proceedings of the National Academy of Sciences **112**, 12042 (2015). Cited on 18, 24, 25, 30, and 86.

[64] R. Boehler, H. Musshoff, R. Ditz, G. Aquilanti, and A. Trapananti, *Portable laser-heating stand for synchrotron applications*, Review of Scientific Instruments **80**, 045103 (2009). Cited on 18, 24, 25, 40, 41, and 81.

[65] J. Ruiz-Fuertes, A. Karandikar, R. Boehler, and D. Errandonea, *Microscopic evidence of a flat melting curve of tantalum*, Physics of the Earth and Planetary Interiors **181**, 69 (2010). Cited on 18, 22, 23, 34, 58, 59, 60, 61, and 79.

[66] Z. Du and K. K. M. Lee, *High-pressure melting of MgO from (Mg, Fe)O solid solutions*, Geophysical Research Letters **41**, 1 (2014). Cited on 18.

[67] R. Boehler, *The phase diagram of iron to 430 kbar*, Geophysical Research Letters **13**, 1153 (1986). Cited on 19 and 20.

[68] S. Weir, M. Lipp, S. Falabella, G. Samudrala, and Y. Vohra, *High pressure melting curve of tin measured using an internal resistive heating technique to 45 GPa*, Journal of Applied Physics **111**, 123539 (2012). Cited on 20.

[69] A. Rosenfeld and M. Stott, *Change in resistivity of simple metals on melting*, Physical Review B **42**, 3406 (1990). Cited on 20.

[70] C. Zha and R. Boehler, *Melting of sodium and potassium in a diamond anvil cell*, Physical Review B **31**, 3199 (1985). Cited on 20.

[71] C. Zha, R. Boehler, D. Young, and M. Ross, *The argon melting curve to very high pressures*, The Journal of Chemical Physics **85**, 1034 (1986). Cited on 20.

[72] V. Diatschenko, C. Chu, D. Liebenberg, D. Young, M. Ross, and R. Mills, *Melting curves of molecular hydrogen and molecular deuterium under high pressures between 20 and 373 K*, Physical Review B **32**, 381 (1985). Cited on 20.

[73] F. Datchi and P. Loubeyre, *Extended and accurate determination of the melting curves of argon, helium, ice, (H_2O), and hydrogen (H_2)*, Physical Review B **61**, 6535 (2000). Cited on 20.

[74] R. Boehler, *Melting and thermal expansion of iron in uniformly laser-heated diamond anvil cells*, High Pressure Research **5**, 702 (1990). Cited on 21.

[75] R. Boehler, N. von Bargen, and A. Chopelas, *Melting, thermal expansion, and phase transitions of iron at high pressures*, Journal of Geophysical Research **95**, 21731 (1990). Cited on 21, 30, and 93.

[76] R. Boehler, *Melting of the Fe-FeO and the Fe-FeS systems at high pressure: Constraints on core temperatures*, Earth and Planetary Science Letters **111**, 217 (1992). Cited on 21.

[77] R. Boehler, *Fe-FeS eutectic temperatures to 620 kbar*, Physics of the Earth and Planetary Interiors **96**, 181 (1996). Cited on 21 and 34.

[78] A. Zerr and R. Boehler, *Melting of (Mg, Fe)SiO_3-Perovskite to 625 Kilobars: Indication of a High Melting Temperature in the Lower Mantle*, Science **262**, 553 (1993). Cited on 21, 22, and 79.

[79] D. Errandonea, B. Schwager, R. Ditz, C. Gessmann, R. Boehler, and M. Ross, *Systematics of transition-metal melting*, Physical Review B **63**, 132104 (2001). Cited on 21, 30, 34, 46, 47, 54, 55, 57, 58, 59, 60, 61, 79, 113, 114, 115, 119, 120, 122, and 124.

[80] D. Errandonea, R. Boehler, and M. Ross, *Melting of the alkaline-earth metals to 80 GPa*, Physical Review B **65**, 012108 (2001). Cited on 21, 79, and 124.

[81] S. Japel, B. Schwager, R. Boehler, and M. Ross, *Melting of copper and nickel at high pressure: The role of d electrons*, Physical Review Letters **95**, 167801 (2005). Cited on 21, 29, 79, 122, and 124.

[82] M. Ross, R. Boehler, and D. Errandonea, *Melting of transition metals at high pressure and the influence of liquid frustration: The late metals Cu, Ni, and Fe*, Physical Review B **76**, 184117 (2007). Cited on 21 and 79.

[83] B. Schwager, M. Ross, S. Japel, and R. Boehler, *Melting of Sn at high pressure: comparisons with Pb*, The Journal of chemical physics **133**, 084501 (2010). Cited on 21, 79, and 124.

[84] R. Boehler, M. Ross, P. Söderlind, and D. B. Boercker, *High-pressure melting curves of argon, krypton, and xenon: Deviation from corresponding states theory*, Physical Review Letters **86**, 5731 (2001). Cited on 21, 49, 51, and 79.

[85] R. Boehler, M. Ross, and D. Boercker, *Melting of LiF and NaCl to 1 Mbar: Systematics of ionic solids at extreme conditions*, Physical Review Letters **78**, 4589 (1997). Cited on 21, 22, 28, and 79.

[86] B. Schwager and R. Boehler, *H_2O: another ice phase and its melting curve*, High Pressure Research **28**, 431 (2008). Cited on 21, 40, and 79.

[87] A. Zerr, G. Serghiou, and R. Boehler, *Melting of $CaSiO_3$ perovskite to 430 kbar and first in-situ measurements of lower mantle eutectic temperatures.*, Geophysical Research Letters **24**, 909 (1997). Cited on 22.

[88] A. Zerr and R. Boehler, *Solidus of Earth's deep mantle*, Science **281**, 243 (1998). Cited on 22.

[89] C. Yoo, J. Akella, A. Campbell, H. Mao, and R. Hemley, *Phase diagram of iron by in situ X-ray diffraction: Implications for Earth's core*, Science **270**, 1473 (1995). Cited on 23.

[90] G. Shen, H. Mao, R. Hemley, T. Duffy, and M. Rivers, *Melting and crystal structure of iron at high pressures and temperatures*, Geophysical Research Letters **25**, 373 (1998). Cited on 23 and 30.

[91] G. Shen, N. Sata, M. Rivers, and S. Sutton, *Melting of indium at high pressure determined by monochromatic X-ray diffraction in an*

externally-heated diamond anvil cell, Applied Physics Letters **78**, 3208 (2001). Cited on 23, 24, 124, and 125.

[92] G. Shen, V. Prakapenka, M. Rivers, and S. Sutton, *Structure of liquid iron at pressures up to 58 GPa*, Physical Review Letters **92**, 185701 (2004). Cited on 24.

[93] A. Dewaele, M. Mezouar, N. Guignot, and P. Loubeyre, *Melting of lead under high pressure studied using second-scale time-resolved X-ray diffraction*, Physical Review B **76**, 144106 (2007). Cited on 24, 33, 61, and 124.

[94] W. Sturhahn, E. Alp, T. Toellner, and P. Hession, *Introduction to nuclear resonant scattering with synchrotron radiation*, Hyperfine Interactions **113**, 47 (1998). Cited on 25.

[95] M. Ahart, A. Karandikar, S. Gramsch, R. Boehler, and R. Hemley, *High P-T Brillouin scatttering study of H_2O melting to 26 GPa*, High Pressure Research **34**, 327 (2014). Cited on 26.

[96] T. Devine and F. Adar, in *Characterization of materials*, edited by E. Kaufmann (John Wiley & Sons, Inc., 2012), pp. 1067–1104, 2nd ed., ISBN 978-1-118-11074-4. Cited on 26.

[97] P. Richet, B. Mysen, and D. Andrault, *Melting and premelting of silicates: Raman spectroscopy and X-ray diffraction of Li_2SiO_3 and Na_2SiO_3*, Physics and chemistry of minerals **23**, 157 (1996). Cited on 26.

[98] A. Zinn, D. Schiferl, and M. Nicol, *Raman spectroscopy and melting of nitrogen between 290 and 900 K and 2.3 and 18 GPa*, The Journal of Chemical Physics **87**, 1267 (1987). Cited on 26.

[99] A. Goncharov and J. Crowhurst, *Raman spectroscopy of hot compressed hydrogen and nitrogen: Implications for the intramolecular potential*, Physical Review Letters **96**, 055504 (2006). Cited on 26.

[100] A. Goncharov, J. Crowhurst, V. Struzhkin, and R. Hemley, *Triple point on the melting curve and polymorphism of nitrogen at high pressure*, Physical Review Letters **101**, 095502 (2008). Cited on 26.

[101] E. Gregoryanz, A. Goncharov, K. Matsuishi, H. Mao, and R. Hemley, *Raman spectroscopy of hot dense hydrogen*, Physical review letters **90**, 175701 (2003). Cited on 26.

[102] M. Eremets and I. Trojan, *Evidence of maximum in the melting curve of hydrogen at megabar pressures*, JETP Letters **89**, 174 (2009). Cited on 26.

[103] J. Lin, B. Militzer, V. Struzhkin, E. Gregoryanz, R. Hemley, and H. Mao, *High pressure-temperature Raman measurements of H_2O melting to 22 GPa and 900 K*, The Journal of Chemical Physics **121**, 8423 (2004). Cited on 27.

[104] A. Goncharov, N. Goldman, L. Fried, J. Crowhurst, I. Kuo, C. Mundy, and J. Zaug, *Dynamic ionization of water under extreme conditions*, Physical Review Letters **94**, 125508 (2005). Cited on 27.

[105] A. Goncharov and J. Crowhurst, *Pulsed laser Raman spectroscopy in the laser-heated diamond anvil cell*, Review of Scientific Instruments **76**, 063905 (2005). Cited on 27.

[106] H. Mao and R. Hemley, *Optical transitions in diamond at ultrahigh pressures*, Nature **351**, 721 (1991). Cited on 27.

[107] T. Ahrens, in *Geophysics - Laboratory measurements*, edited by C. Sammis and T. Henyey (Academic Press, Inc., 1987), chap. 6, pp. 185–235, ISBN 0-12-475966-1. Cited on 27.

[108] J. Forbes, in *Shock wave compression of condensed matter - A primer*, edited by J. Forbes (Springer Berlin Heidelberg, 2012), chap. 4, pp. 59–100, ISBN 978-3-642-32534-2. Cited on 27.

[109] G. Lyzenga and T. Ahrens, *Multiwavelength optical pyrometer for shock compression experiments*, Review of Scientific Instruments **50**, 1421 (1979). Cited on 28.

[110] J. Shaner, J. Brown, and R. McQueen, *Melting of metals above 100 GPa*, in *High pressure in science and technology*, edited by C. Homan, R. MacCrone, and E. Whalley (North-Holland, 1984), vol. 22, pp. 137–141. Cited on 28 and 29.

[111] R. Boehler, M. Ross, and D. Boercker, *High-pressure melting curves of alkali halides*, Physical review B **53**, 556 (1996). Cited on 28.

[112] J. Akins, S. Luo, P. Asimow, and T. Ahrens, *Shock-induced melting of $MgSiO_3$ perovskite and implications for melts in Earth's lowermost mantle*, Geophysical Research Letters **31**, L14612 (2004). Cited on 28.

[113] G. Lyzenga and T. Ahrens, *Shock temperatures of SiO_2 and their geophysical implications*, Journal of Geophysical Research **88**, 2431 (1983). Cited on 28.

[114] A. Jayaraman, W. Klement Jr., R. Newton, and G. Kennedy, *Fusion curves and polymorphic transitions of the group III elements - aluminum, gallium, indium and thallium - at high pressures*, Journal of Physics and Chemistry of Solids **24**, 7 (1963). Cited on 29.

[115] D. Errandonea, *The melting curve of ten metals up to 12 GPa and 1600 K*, Journal of Applied Physics **108**, 033517 (2010). Cited on 29.

[116] A. Hänström and P. Lazor, *High pressure melting and equation of state of aluminium*, Journal of Alloys and Compounds **305**, 209 (2000). Cited on 29 and 124.

[117] R. Boehler and M. Ross, *Melting curve of aluminum in a diamond cell to 0.8 Mbar: implications for iron*, Earth and Planetary Science Letters **153**, 223 (1997). Cited on 29 and 124.

[118] J. Akella and G. Kennedy, *Melting of gold, silver, and copper proposal for a new high-pressure calibration scale*, Journal of Geophysical Research **76**, 4969 (1971). Cited on 29.

[119] H. Brand, D. Dobson, L. Vočadlo, and I. Wood, *Melting curve of copper measured to 16 GPa using a multi-anvil press*, High Pressure Research **26**, 185 (2006). Cited on 29.

[120] D. Hayes, R. Hixson, and R. McQueen, *High pressure elastic properties, solid-liquid phase boundary and liquid equation of state from release wave measurements in shock-loaded copper*, AIP Conference Proceedings **505**, 483 (2000). Cited on 29.

[121] R. Boehler, *Temperatures in the Earth's core from melting point measurements of iron at high static pressures*, Nature **363**, 534 (1993). Cited on 28 and 30.

[122] T. Ahrens, *Phase diagram of iron, revised-core temperatures*, Geophysical Research Letters **29**, 2 (2002). Cited on 29 and 30.

[123] Q. Williams, R. Jeanloz, J. Bass, B. Svendsen, and T. Ahrens, *The melting curve of iron to 250 Gigapascals: A constraint on the temperature at Earth's center*, Science **236**, 181 (1987). Cited on 30 and 39.

[124] Y. Ma, M. Somayazulu, G. Shen, H. Mao, J. Shu, and R. Hemley, *In situ X-ray diffraction studies of iron to Earth-core conditions*, Physics of the Earth and Planetary Interiors **143-144**, 455 (2004). Cited on 30.

[125] R. Boehler, D. Santamaría-Pérez, D. Errandonea, and M. Mezouar, *Melting, density, and anisotropy of iron at core conditions: new X-ray measurements to 150 GPa*, Journal of Physics: Conference Series **121**, 022018 (2008). Cited on 30.

[126] S. Anzellini, A. Dewaele, M. Mezouar, P. Loubeyre, and G. Morard, *Melting of iron at Earths inner Core boundary based on fast X-ray diffraction*, Science **340**, 464 (2013). Cited on 30.

[127] J. Brown and G. Mcqueen, *Phase transitions, Grüneisen parameter and elasticity for shocked iron between 77 GPa and 400 GPa*, Journal of Geophysical Research **91**, 7485 (1986). Cited on 30 and 35.

[128] J. Bass, B. Svendsen, and T. Ahrens, *The temperature of shock compressed iron*, in *High-pressure research in mineral physics*, edited by M. H. Manghnani and Y. Syono (American Geophysical Union, 1987), pp. 393–402. Cited on 30.

[129] C. Yoo, N. Holmes, M. Ross, D. Webb, and C. Pike, *Shock temperatures and melting of iron at Earth core conditions*, Physical Review Letters **70**, 3931 (1993). Cited on 30 and 35.

[130] J. Nguyen and N. Holmes, *Melting of iron at the physical conditions of the Earth's core*, Nature **427**, 339 (2004). Cited on 30.

[131] A. Dewaele, M. Mezouar, N. Guignot, and P. Loubeyre, *High melting points of tantalum in a laser-heated diamond anvil cell*, Physical Review Letters **104**, 255701 (2010). Cited on 33, 34, 58, 59, 60, 61, 80, 81, 113, 114, 115, 119, and 120.

[132] M. Foata-Prestavoine, G. Robert, M. Nadal, and S. Bernard, *First-principles study of the relations between the elastic constants, phonon dispersion curves, and melting temperatures of bcc Ta at pressures up to 1000 GPa*, Physical Review B **76**, 104104 (2007). Cited on 33, 58, 59, and 60.

[133] P. Beck, A. Goncharov, V. Struzhkin, B. Militzer, H. Mao, and R. Hemley, *Measurement of thermal diffusivity at high pressure using a transient heating technique*, Applied Physics Letters **91**, 181914 (2007). Cited on 34.

[134] A. Goncharov, P. Beck, V. Struzhkin, R. Hemley, and J. Crowhurst, *Laser-heating diamond anvil cell studies of simple molecular systems at high pressures and temperatures*, Journal of Physics and Chemistry of Solids **69**, 2217 (2008). Cited on 34.

[135] S. Rekhi, J. Tempere, and I. Silvera, *Temperature determination for nanosecond pulsed laser heating*, Review of Scientific Instruments **74**, 3820 (2003). Cited on 34.

[136] K. Gallagher, J. Bass, T. Ahrens, M. Fitzner, and J. Abelson, *Shock temperature of stainless steel and a high pressure - high temperature constraint on thermal diffusivity of Al_2O_3*, AIP Conference Proceedings **309**, 963 (1994). Cited on 35.

[137] J. Brown and J. Shaner (Elsevier, Amsterdam, 1984), chap. II, pp. 91–94, ISBN 9780444869043. Cited on 35, 59, 60, 61, and 113.

[138] D. Boness and J. Brown, *The electronic band structures of iron, sulfur, and oxygen at high pressures and the Earth's core*, Journal of Geophysical Research **95**, 21721 (1990). Cited on 35.

[139] S. Luo and T. Ahrens, *Shock-induced superheating and melting curves of geophysically important minerals*, Physics of the Earth and Planetary Interiors **143-144**, 369 (2004). Cited on 35.

[140] M. Forsblom and G. Grimvall, *How superheated crystals melt*, Nature materials **4**, 388 (2005). Cited on 35.

[141] S. Luo, T. Ahrens, T. Çan, A. Strachan, W. Goddard, and D. Swift, *Maximum superheating and undercooling: Systematics, molecular dynamics simulations, and dynamic experiments*, Physical Review B **68**, 1 (2003). Cited on 36.

[142] R. Boehler, *Laser heating in the diamond cell: techniques and applications*, Hyperfine Interactions **128**, 307 (2000). Cited on 38, 92, and 93.

[143] M. Planck and M. Masius, *The theory of heat radiation* (P. Blakiston's Son & Co., 1914), 1st ed. Cited on 41.

[144] C. Gürk, *Personal communication* (Max Planck Institut für Chemie, Mainz, Germany, 2009). Cited on 41.

[145] E. Savitskii and G. Burkhanov (Consultants Bureau, 1970), chap. 2, pp. 7–58. Cited on 45.

[146] T. Tietz and J. Wilson, in *Behaviour and properties of refractory metals* (University of Tokyo Press, 1965), chap. 6, pp. 206–221, 1st ed. Cited on 45.

[147] J. Diaz, *Pure rhenium metal*, Potentials, IEEE **15**, 37 (1996). Cited on 45.

[148] A. Naor, N. Eliaz, E. Gileadi, and S. Taylor, *Properties and applications of rhenium and its alloys*, AMMTIAC Quarterly **5**, 11 (2010). Cited on 45.

[149] C. Hammond, in *CRC handbook of chemistry and physics*, edited by W. Haynes (CRC Press/Taylor and Francis, 2014), chap. 4, pp. 4.01–4.42, 96th ed. Cited on 45 and 46.

[150] C. Zha, W. Bassett, and S. Shim, *Rhenium - an in situ pressure calibrant for internally heated diamond anvil cells*, Review of Scientific Instruments **75**, 2409 (2004). Cited on 45.

[151] H. Olijnyk, A. Jephcoat, and K. Refson, *On optical phonons and elasticity in the hcp transition metals Fe, Ru and Re at high pressure*, Europhysics Letters **53**, 504 (2001). Cited on 45.

[152] Y. Vohra, S. Duclos, and A. Ruoff, *High-pressure X-ray diffraction studies on rhenium up to 216 GPa (2.16 Mbar)*, Physical Review B **36**, 9790 (1987). Cited on 45.

[153] R. McQueen, S. Marsh, J. Taylor, J. Fritz, and W. Carter, in *High-velocity impact phenomena*, edited by Kinslow Ray (Academic Press, 1970), chap. VII, pp. 348–349. Cited on 45.

[154] A. Verma, P. Ravindran, R. Rao, B. Godwal, and R. Jeanloz, *On the stability of rhenium up to 1 TPa pressure against transition to the bcc structure*, Bulletin of Material Science **26**, 183 (2003). Cited on 45.

[155] L. Vereshchagin and N. Fateeva, *Melting temperatures of refractory metals pressures high pressures*, High Temperature-High Pressure **9**, 619 (1977). Cited on 45, 53, and 54.

[156] C. Gupta, in *Extractive metallurgy of molybdenum* (CRC Press, 1992), chap. 1, pp. 1–63, 1st ed. Cited on 46.

[157] R. Hixson, D. Boness, and J. Shaner, *Acoustic velocities and phase transitions in molybdenum under strong shock compression*, Physical Review Letters **62**, 637 (1989). Cited on 46 and 47.

[158] L. Cai, Z. Zeng, X. Zhang, and J. Hu, *Experimental research on high pressure phase transitions of Mo and Ta*, in *EPJ Web of Conferences- 10* (EDP Sciences, 2010), vol. 10, p. 28. Cited on 46 and 47.

[159] D. Santamaría-Pérez, M. Ross, D. Errandonea, G. Mukherjee, M. Mezouar, and R. Boehler, *X-ray diffraction measurements of Mo melting to 119 GPa and the high pressure phase diagram*, The Journal of chemical physics **130**, 124509 (2009). Cited on 46, 47, and 54.

[160] J. Moriarty, *Angular forces and melting in bcc transition metals - A case study of molybdenum*, Physical Review B **49**, 12431 (1994). Cited on 46 and 47.

[161] L. Burakovsky, D. Preston, and R. Silbar, *Analysis of dislocation mechanism for melting of elements: Pressure dependence*, Journal of Applied Physics **88**, 6294 (2000). Cited on 46 and 47.

[162] A. Verma, R. Rao, and B. Godwal, *Theoretical solid and liquid state shock Hugoniots of Al, Ta, Mo and W*, Journal of Physics: Condensed Matter **16**, 4799 (2004). Cited on 46, 47, 59, and 60.

[163] A. Belonoshko, S. Simak, A. Kochetov, B. Johansson, L. Burakovsky, and D. Preston, *High-pressure melting of molybdenum*, Physical Review Letters **92**, 195701 (2004). Cited on 46 and 47.

[164] F. Xi and L. Cai, *Theoretical study of melting curves on Ta, Mo, and W at high pressures*, Physica B **403**, 2065 (2008). Cited on 46, 47, 59, and 60.

[165] A. Belonoshko, L. Burakovsky, S. Chen, B. Johansson, A. Mikhaylushkin, D. Preston, S. Simak, and D. Swift, *Molybdenum at high pressure and temperature: Melting from another solid phase*, Physical Review Letters **100**, 135701 (2008). Cited on 46 and 47.

[166] C. Cazorla, M. Gillan, S. Taioli, and D. Alfè, *Ab initio melting curve of molybdenum by the phase coexistence method*, The Journal of chemical physics **126**, 194502 (2007). Cited on 46 and 47.

[167] Z. Zeng, C. Hu, X. Liu, L. Cai, and F. Jing, *Ab initio study of acoustic velocities in molybdenum under high pressure and high temperature*, Applied Physics Letters **99**, 191906 (2011). Cited on 47.

[168] B. Godwal and R. Jeanloz, *Pressure induced s - d transfer and the equation of state of molybdenum*, Physical Review B **41**, 7440 (1990). Cited on 47.

[169] J. Moriarty, *Ultrahigh-pressure structural phase transitions in Cr, Mo, and W*, Physical Review B **45**, 2004 (1992). Cited on 47.

[170] N. Christensen, A. Ruoff, and C. Rodriguez, *Pressure strengthening: A way to multimegabar static pressures*, Physical Review B **52**, 9121 (1995). Cited on 47.

[171] J. Boettger, *Relativistic effects on the structural phase stability of molybdenum*, Journal of Physics: Condensed Matter **11**, 3237 (1999). Cited on 47.

[172] M. Ross, R. Boehler, and S. Japel, *Melting of bcc transition metals and icosahedral clustering*, Journal of Physics and Chemistry of Solids **67**, 2178 (2006). Cited on 47.

[173] Y. Vohra and L. Ruoff, *Static compression of metals Mo, Pb, and Pt to 272 GPa : Comparison with shock data*, Physical review B **42**, 8651 (1990). Cited on 47.

[174] A. Ruoff, H. Xia, and Q. Xia, *The effect of a tapered aperture on X-ray diffraction from a sample with a pressure gradient: Studies on three samples with a maximum pressure of 560 GPa*, Review of Scientific Instruments **63**, 4342 (1992). Cited on 47.

[175] T. Duffy, G. Shen, J. Shu, H. Mao, R. Hemley, and A. Singh, *Elasticity, shear strength, and equation of state of molybdenum and gold from X-ray diffraction under nonhydrostatic compression to 24 GPa*, Journal of Applied Physics **86**, 6729 (1999). Cited on 47.

[176] D. Brandon and W. Kaplan, in *Microstructural characterization of materials* (John Wiley & Sons, Ltd., 2008), chap. 5, pp. 261–331, 2nd ed., ISBN 9780470027844. Cited on 50, 70, and 99.

[177] L. Wittenberg and D. R., *Volume contraction during melting : Emphasis on lanthanide and actinide metals*, The Journal of Chemical Physics **56**, 4526 (1972). Cited on 54.

[178] P. Oelhafen, R. Wahrenberg, and H. Stupp, *Electronic structure of liquid transition metals studied by time resolved photoelectron spectroscopy*, Journal of Physics: Condensed Matter **12**, A9 (2000). Cited on 54.

[179] P. Oelhafen, R. Wahrenberg, and H. Stupp, *Electronic structure of liquid tungsten studied by time resolved photoelectron spectroscopy*, Europhysics Letters **49**, 782 (2000). Cited on 54.

[180] G. Miller, *Tantalum and niobium* (Butterworth Scientific Publications, 1959). Cited on 57.

[181] R. Balliett, M. Coscia, and F. Hunkeler, *Niobium and tantalum in materials selection*, Journal of Metals **38**, 25 (1986). Cited on 57.

[182] R. Buckman, *New applications for tantalum and tantalum alloys*, Journal of Metals **52**, 40 (2000). Cited on 57.

[183] L. Malter and D. B. Langmuir, *Resistance, emissivities and melting point of tantalum*, Physical Review **55**, 743 (1939). Cited on 58, 60, and 68.

[184] J. Shaner, G. Gathers, and C. Minichino, *Thermophysical properties of liquid tantalum and molybdenum*, High Temperature - High Pressure **9**, 331 (1977). Cited on 58, 60, and 68.

[185] N. Fateeva and L. Vereshchagin, *Melting curves of tantalum up to 6 GPa*, Soviet Physics DOCKLADY **16**, 322 (1971). Cited on 57, 58, 60, 113, 114, and 115.

[186] D. Errandonea, M. Somayazulu, D. Häusermann, and H. Mao, *Melting of tantalum at high pressure determined by angle dispersive X-ray diffraction in a double-sided laser-heated diamond-anvil cell*, Journal of Physics: Condensed Matter **15**, 7635 (2003). Cited on 58, 59, 60, 62, 81, 113, 114, 115, 119, 120, and 124.

[187] C. Dai, J. Hu, and H. Tan, *Hugoniot temperatures and melting of tantalum under shock compression determined by optical pyrometry*, Journal of Applied Physics **106**, 043519 (2009). Cited on 59 and 60.

[188] J. Li, X. Zhou, J. Li, Q. Wu, L. Cai, and C. Dai, *Development of a simultaneous Hugoniot and temperature measurement for preheated-metal shock experiments: melting temperatures of Ta at pressures of 100 GPa*, Review of Scientific Instruments **83**, 053902 (2012). Cited on 59 and 60.

[189] S. Taioli, C. Cazorla, M. J. Gillan, and D. Alfè, *Melting curve of tantalum from rst principles*, Physical Review B **75**, 214103 (2007). Cited on 59, 60, 119, and 120.

[190] A. Strachan, T. Çain, O. Gülseren, S. Mukherjee, R. Cohen, and W. Goddard III, *First principles force field for metallic tantalum*, Modelling and Simulation in Materials Science and Engineering **12**, S445 (2004). Cited on 59, 60, 114, 115, and 116.

[191] Y. Wang, R. Ahuja, and B. Johansson, *Melting of iron and other metals at earths core conditions: A simplified computational approach*, Physical Review B **65**, 014104 (2001). Cited on 59 and 60.

[192] J. Moriarty, J. Belak, R. Rudd, P. Söderlind, F. Streitz, and L. Yang, *Quantum-based atomistic simulation of materials properties in transition metals*, Journal of Physics: Condensed Matter **14**, 2825 (2002). Cited on 59, 60, and 120.

[193] Z. Liu, L. Cai, X. Chen, and F. Jing, *Molecular dynamics simulations of the melting curve of tantalum under pressure*, Physical Review B **77**, 024103 (2008). Cited on 59, 60, 79, 114, 115, and 116.

[194] L. Burakovsky, S. Chen, D. Preston, A. Belonoshko, A. Rosengren, A. Mikhaylushkin, S. Simak, and J. Moriarty, *High-pressure – high-temperature polymorphism in Ta: Resolving an ongoing experimental controversy*, Physical Review Letters **104**, 255702 (2010). Cited on 59, 60, and 61.

[195] J. Haskins, J. Moriarty, and R. Hood, *Polymorphism and melt in high-pressure tantalum*, Physical Review B **86**, 224104 (2012). Cited on 59 and 60.

[196] C. Wu, P. Söderlind, J. Glosli, and J. Klepeis, *Shear-induced anisotropic plastic flow from body-centred-cubic tantalum before melting*, Nature materials **8**, 223 (2009). Cited on 60 and 61.

[197] Y. Yao and D. Klug, *Stable structures of tantalum at high temperature and high pressure*, Physical Review B **88**, 054102 (2013). Cited on 60 and 61.

[198] Z. Liu, L. Cai, X. Zhang, and F. Xi, *Predicted alternative structure for tantalum metal under high pressure and high temperature*, Journal of Applied Physics **114**, 73520 (2013). Cited on 60 and 61.

[199] M. Ross, D. Errandonea, and R. Boehler, *Melting of transition metals at high pressure and the influence of liquid frustration: The early metals Ta and Mo*, Physical Review B **76**, 184118 (2007). Cited on 59 and 60.

[200] L. Hsiung and D. Lassila, *Shock-induced displacive transformations in Ta and Ta-W alloys*, Scripta Materiala **39**, 603 (1998). Cited on 61.

[201] J. Hu, C. Dai, Y. Yu, Z. Liu, Y. Tan, X. Zhou, H. Tan, L. Cai, and Q. Wu, *Sound velocity measurements of tantalum under shock compression in the 10-110 GPa range*, Journal of Applied Physics **111**, 033511 (2012). Cited on 61.

[202] P. Rigg, R. Scharff, and R. Hixson, *Sound speed measurements in tantalum using the front surface impact technique*, Journal of Physics: Conference Series **500**, 032018 (2014). Cited on 61.

[203] H. Cynn and C. S. Yoo, *Equation of state of tantalum to 174 GPa*, Physical Review B **59**, 8526 (1999). Cited on 61 and 118.

[204] L. Yang, A. Karandikar, and R. Boehler, *Flash heating in the diamond cell: melting curve of rhenium*, Review of Scientific Instruments **83**, 063905 (2012). Cited on 63 and 124.

[205] Y. Akahama and H. Kawamura, *High-pressure Raman spectroscopy of diamond anvils to 250 GPa: Method for pressure determination in the multimegabar pressure range*, Journal of Applied Physics **96**, 3748 (2004). Cited on 67 and 97.

[206] J. Orloff, M. Utlaut, and L. Swanson, in *High resolution focused ion beams: FIB and its applications* (Springer US, 2003), chap. 7, pp. 205–290, ISBN 978-1-4613-5229-7. Cited on 76, 107, and 110.

[207] M. Planck, *Über eine Verbesserung der Wienschen Spektralgleichung*, Verhandlungen der Deutscher Physikalischer Gesellschaften **2**, 202 (1900). Cited on 91.

[208] G. Kirchhoff, *Ueber das Verhältniss zwischen dem Emissionsvermögen und dem Absorptionsvermögen der Körper für Wärme und Licht*, Annalen der Physik **185**, 275 (1860). Cited on 91.

[209] J. C. de Vos, *A new determination of the emissivity of tungsten ribbon*, Physica **20**, 690 (1954). Cited on 92 and 94.

[210] R. Larrabee, *The spectral emissivity and optical properties of tungsten*, Technical Report - Research Laboratory of Electronics, Massachusetts Institute of Technology Cambridge, Massachusetts pp. 1–81 (1957). Cited on 92.

[211] L. Dubrovinsky and S. Saxena, *Emissivity measurements on some metals and oxides using multiwavelength spectral radiometry*, High Temperatures - High Pressures **31**, 393 (1999). Cited on 92.

[212] R. Boehler, *Personal communication* (Max Planck Institut für Chemie, Mainz, Germany, 2010). Cited on 93.

[213] R. Boehler, *Personal communication* (Max Planck Institut für Chemie, Mainz, Germany, 2010). Cited on 94.

[214] R. Boehler, *The phase diagram of iron to 2 Mbar: New static measurements*, AIP Conference Proceedings **309**, 919 (1994). Cited on 94.

[215] A. Zerr, G. Serghiou, and R. Boehler, in *Handbook of ceramic hard materials*, edited by R. Riedel (Wiley-VCH Verlag GmbH, 2000), chap. 2, pp. 41–65, ISBN 9783527618217. Cited on 94.

[216] R. Forman, G. Piermarini, J. Barnett, and S. Block, *Pressure measurement made by the utilization of ruby sharp-line luminescence*, Science **176**, 284 (1972). Cited on 95.

[217] J. Barnett, S. Block, and G. Piermarini, *An optical fluorescence system for quantitative pressure measurement in the diamond-anvil cell*, Review of Scientific Instruments **44**, 1 (1973). Cited on 95.

[218] D. Decker, *Equation of state of NaCl and its use as a pressure gauge in high-pressure research*, Journal of Applied Physics **36**, 157 (1965). Cited on 95.

[219] D. Decker, *Equation of state of sodium chloride*, Journal of Applied Physics **37**, 5012 (1966). Cited on 95.

[220] D. Decker, *High-pressure equation of state for NaCl , KCl , and CsCl*, Journal of Applied Physics **42**, 3239 (1971). Cited on 95.

[221] G. Piermarini, S. Block, J. Barnett, and R. Forman, *Calibration of the pressure dependence of the R1 Ruby fluorescence line To 195 Kbar*, Journal of Applied Physics **46**, 2774 (1975). Cited on 95.

[222] G. Piermarini and S. Block, *Ultrahigh pressure diamond-anvil cell and several semiconductor phase transition pressures in relation to the fixed point pressure scale*, Review of Scientific Instruments **46**, 973 (1975). Cited on 95.

[223] H. Mao, P. Bell, J. Shaner, and D. Steinberg, *Specific volume measurements of Cu, Mo, Pd, and Ag and calibration of the suby R1 fluorescence pressure gauge from 0.06 to 1 Mbar*, Journal of Applied Physics **49**, 3276 (1978). Cited on 95.

[224] P. Bell, J. Xu, and H. Mao, in *Shock waves in condensed matter*, edited by Y. Gupta (Springer US, 1986), chap. 2, pp. 125–130. Cited on 95.

[225] I. Aleksandrov, A. Goncharov, A. Zisman, and S. Stishov, *Diamond at high pressures: Raman scattering of light, equation of state, and high-pressure scale*, Soviet Physics JETP **66**, 384 (1987). Cited on 95.

[226] R. Hemley, C. Zha, A. Jephcoat, H. Mao, L. Finger, and D. Cox, *X-ray diffraction and equation of state of solid neon to 110 GPa*, Physical Review B **39**, 11820 (1989). Cited on 95.

[227] J. Eggert, K. Goettel, and I. Silvera, *Ruby at high pressure. I - Optical line shifts to 156 GPa*, Physical review B **40**, 5724 (1989). Cited on 95.

[228] J. Eggert, K. Goettel, and I. Silvera, *Ruby at high pressure. II - Fluorescence lifetime of the R line to 130 GPa*, Physical Review B **40**, 5733 (1989). Cited on 95.

[229] C. Zha, H. Mao, and R. Hemley, *Elasticity of MgO and a primary pressure scale to 55 GPa*, Proceedings of the National Academy of Sciences **97**, 13494 (2000). Cited on 95.

[230] W. Holzapfel, *Refinement of the ruby luminescence pressure scale*, Journal of Applied Physics **93**, 1813 (2003). Cited on 95.

[231] P. Dorogokupets and A. Oganov, *Equations of state of Cu and Ag and revised ruby pressure scale*, Doklady Earth Sciences **410**, 1091 (2003). Cited on 95.

[232] A. Dewaele, P. Loubeyre, and M. Mezouar, *Equations of state of six metals above 94 GPa*, Physical Review B **70**, 094112 (2004). Cited on 95 and 118.

[233] A. Chijioke, W. Nellis, A. Soldatov, and I. Silvera, *The ruby pressure standard to 150 GPa*, Journal of Applied Physics **98**, 114905 (2005). Cited on 95.

[234] A. Goncharov, J. Zaug, J. Crowhurst, and E. Gregoryanz, *Optical calibration of pressure sensors for high pressures and temperatures*, Journal of Applied Physics **97**, 094917 (2005). Cited on 95.

[235] F. Datchi, A. Dewaele, P. Loubeyre, R. Letoullec, Y. Le Godec, and B. Canny, *Optical pressure sensors for high-pressurehigh-temperature studies in a diamond anvil cell*, High Pressure Research **27**, 447 (2007). Cited on 95.

[236] H. Mao, J. Xu, and P. Bell, *Calibration of the ruby pressure gauge to 800 kbar under quasi-hydrostatic conditions*, Journal of Geophysical Research **91**, 4673 (1986). Cited on 96.

[237] M. Hanfland and K. Syassen, *A Raman study of diamond anvils under stress*, Journal of Applied Physics **57**, 2752 (1985). Cited on 97.

[238] Y. Akahama and H. Kawamura, *Pressure calibration of diamond anvil Raman gauge to 310 GPa*, Journal of Applied Physics **100**, 043516 (2006). Cited on 97.

[239] J. Goldstein, J. Newbury, D. Joy, C. Lyman, P. Echlin, E. Lifshin, L. Sawyer, and J. Michael, in *Scanning electron microscopy and X-ray microanalysis* (Springer US, 2003), chap. 1, pp. 1–20, 3rd ed., ISBN ISBN 978-0-306-47292-3. Cited on 99.

[240] *SEM - Q & A* (JEOL Ltd., 2015). Cited on 99 and 102.

[241] *JEOL guide to scanning microscope observation* (JEOL Ltd., 2015). Cited on 99 and 100.

[242] *Instruction manual AURIGA series, (Revision en4)* (Carl Zeiss NTS GmbH, 2010). Cited on 101, 108, and 109.

[243] D. Brandon and W. Kaplan, in *Microanalysis in electron microscopy* (John Wiley & Sons, Ltd, 2008), chap. 6, pp. 333–390, 2nd ed., ISBN 9780470027844. Cited on 102.

[244] *Silicon drift detectors explained* (Oxford Instruments, 2012). Cited on 103.

[245] *AZtec user manual* (Oxford Instruments, 2013). Cited on 103.

[246] R. Langford, P. Nellen, J. Gierak, and Y. Fu, *Focused ion beam micro- and nanoengineering*, Material Research Society Bulletin **32**, 417 (2007). Cited on 107.

[247] J. Orloff, M. Utlaut, and L. Swanson, in *High resolution focused ion beams: FIB and its applications* (Springer US, 2003), chap. 5, pp. 123–145, ISBN 978-1-4613-5229-7. Cited on 107.

[248] C. Volkert and A. Minor, *Focused ion beam microscopy and micromachining*, Material Research Society Bulletin **32**, 389 (2007). Cited on 107.

[249] A. Karandikar and R. Boehler, *Flash melting of tantalum in a diamond cell to 85 GPa*, Physical Review B **93**, 054107 (2016). Cited on 115 and 124.

[250] V. Kechin, *Thermodynamically based melting-curve equation*, Journal of Physics: Condensed Matter **7**, 531 (1995). Cited on 116.

[251] L. Salter, *The Simon melting equation*, Philosophical Magazine **45**, 369 (1954). Cited on 117.

[252] J. Gilvarry, *The Lindemann and Grüneisen Laws*, Physical Review **102**, 308 (1956). Cited on 117 and 121.

[253] J. Gilvarry, *Equation of the fusion curve*, Physical Review **102**, 325 (1956). Cited on 117 and 121.

[254] F. Simon, *The melting of iron at high pressures*, Nature **172**, 746 (1953). Cited on 117.

[255] R. Hixson and J. Fritz, *Shock compression of tungsten and molybdenum*, Journal of Applied Physics **71**, 1721 (1992). Cited on 117.

[256] S. Vaidya and E. Raja Gopal, *Melting Law at High Pressures*, Physical Review Letters **17**, 635 (1966). Cited on 118.

[257] K. Katahara, M. Manghnani, and E. Fisher, *Pressure derivatives of the elastic moduli of niobium and tantalum*, Journal of Applied Physics **47**, 434 (1976). Cited on 118 and 119.

[258] Y. Wang, R. Ahuja, and B. Johansson, *Reduction of shock-wave data with mean-field potential approach*, Journal of Applied Physics **92**, 6616 (2002). Cited on 118.

[259] M. Hanfland, K. Syassen, and J. Köhler, *Pressure volume relationship of Ta*, Journal of Applied Physics **91**, 4143 (2002). Cited on 118.

[260] D. Lide, ed., *American institute of physics handbook* (CRC Press, 1972), 3rd ed., ISBN 978-1420066807. Cited on 119.

[261] K. Gschneidner, in *Solid state physics*, edited by F. Seitz and D. Turnbull (Academic Press, 1964), vol. 16, chap. 4, pp. 275–426, ISBN 978-0-1260-7716-2. Cited on 119.

[262] F. Sheard, *Calculation of the thermal expansion of solids from the third-order elastic constants*, Philosophical Magazine **3**, 1381 (1958). Cited on 119.

[263] T. Rubin, H. Altman, and H. Hohnston, *Thermal expansion of rock salt*, Journal of physical chemistry **65**, 65 (1961). Cited on 119.

[264] R. Carr, R. McCammon, and G. White, *The thermal expansion of copper at low temperatures*, Proceedings of the Royal Society A **280**, 72 (1964). Cited on 119.

[265] R. Cohen and O. Gülseren, *Thermal equation of state of tantalum*, Physical Review B **63**, 224101 (2001). Cited on 119 and 120.

[266] W. Isbell, D. Christman, and S. Babcock, Tech. Rep., Materials and Structures Laboratory, Warren, Michigan (1971). Cited on 119.

[267] C. Bercegeay and S. Bernard, *First-principles equations of state and elastic properties of seven metals*, Physical Review B **72**, 214101 (2005). Cited on 120.

[268] F. Cardarelli, *Materials handbook: A concise desktop reference* (Springer-Verlag London Ltd., 2008), 2nd ed., ISBN 9781846286681. Cited on 120, 122, and 124.

[269] D. Lide, *CRC handbook of chemistry and physics* (CRC Press, 2009), 89th ed., ISBN 9781420066807. Cited on 120 and 124.

[270] F. Stacey, S. Spiliopoulos, and M. Barton, *A critical re-examination of the thermodynamic basis of Lindemann s melting law*, Physics of the Earth and Planetary Interiors **55**, 201 (1989). Cited on 121.

[271] F. Bundy and H. Strong, in *Solid state physics*, edited by F. Seitz and D. Turnbull (Academic Press, 1962), vol. 13, pp. 81–146, ISBN 9780126077131. Cited on 121.

[272] A. Kavner and R. Jeanloz, *High pressure melting curve of platinum*, Journal of Applied Physics **83**, 7553 (1998). Cited on 122.

[273] D. Errandonea, *High-pressure melting curves of the transition metals Cu, Ni, Pd, and Pt*, Physical Review B **87**, 054108 (2013). Cited on 122 and 124.

[274] P. Lazor, Ph.D. thesis (1994). Cited on 122 and 124.

[275] O. Lord, I. Wood, D. Dobson, L. Vočadlo, W. Wang, A. Thomson, E. Wann, G. Morard, M. Mezouar, and M. Walter, *The melting curve of Ni to 1 Mbar*, Earth and Planetary Science Letters **408**, 226 (2015). Cited on 122.

[276] V. Stutzmann, A. Dewaele, J. Bouchet, F. Bottin, and M. Mezouar, *High-pressure melting curve of titanium*, Physical Review B **92**, 224110 (2015). Cited on 124.

[277] P. Mirwald and G. Kennedy, *The melting of gold, silver and copper to 60 kbar pressure - A reinvestigation*, Journal of Geophysical Research **84**, 6750 (1979). Cited on 124.

[278] B. Godwal, C. Meade, R. Jeanloz, A. Garcia, A. Liu, and M. Cohen, *Ultrahigh-pressure melting of lead - A multidisciplinary study*, Science **248**, 462 (1990). Cited on 124.

[279] E. Tankov and E. Ponyatovsky, *Phase transformations of elements under high pressure* (CRC Press, 2004), ISBN 9781420037609. Cited on 125.

[280] D. Young, *Phase diagrams of the elements* (University of California Press, 1991), ISBN 9780520911482. Cited on 125.

List of Figures

List of Tables

List of Abbreviations

ADXRD : Angle Dispersive X-ray Diffraction
AFM : Atomic Force Microscopy
bcc : body centered cubic
BSE : Back Scattered Electron
CCD : Charge-Coupled Device
CW : Continuous Wave
DAC : Diamond Anvil Cell
DFT : Density Functional Theory
dhcp : double hexagonal closed-pack
DTA : Differential Thermal Analysis
EDS : Energy Dispersive X-ray Spectroscopy
EDXRD : Energy Dispersive X-ray Diffraction
EFS : Extended Finnis-Sinclair
EOS : Equation Of State
ESRF : European Synchrotron Radiation Facility
fcc : face centered cubic
FIB : Focused Ion Beam
FIBM : Focused Ion Beam Milling
FM : Force-Matching
GGA : Generalised Gradient Approximation
GUI : Graphical User Interface
hcp : hexagonal closed-pack
IR : Infrared
IRnf : Infrared Notch Filter
IRsf : Infrared Short Pass Filter
ISRO : Icosahedral Short Range Order
LHDAC : Laser-heated Diamond Anvil Cell
LREP : Long-Range Emperical Potential

MAA : Multi-Anvil Apparatus
MGPT : Model Generalized Pseudopotential Theory
ndf : Neutral Density Filter
P : Pressure
PAW : Projector Augmented-Wave
PD : Photo Diode
PE : Primary Electron
PG : Pulse Generator
PI : Primary Ion
PMT : Photo Multiplier Tube
RS : Raman Spectroscopy
SDD : Silicon Drift Detector
SE : Secondary Electron
SEM : Scanning Electron Microscope
SI : Secondary Ion
SMS : Synchrotron Mössbauer Spectroscopy
T : Temperature
TEM : Transmission Electron Microscope
TEM_{00} : Transverse Electric and Magnetic 00 mode
WC : Tungsten Carbide
XAS : X-Ray Absorption Spectroscopy
XRD : X-Ray Diffraction
YAG : Yttrium Aluminium Garnet
YLF : Yttrium Lithium Fluoride

——o——

Eidesstattliche Erklärung

Hiermit versichere ich, dass ich die vorliegende Arbeit ohne unzulässiger Hilfe Dritter und ohne Benutzung anderer als der angegebenen Hilfsmittel angefertigt habe. Die aus fremden Quellen direkt oder indirekt übernommenen Gedanken sind als solche kenntlich gemacht. Diese Arbeit wurde bisher weder im Inland noch im Ausland in gleicher oder ähnlicher Form einer anderen Prüfungsbehörde vorgelegt.

Es haben keine früheren Promotionsverfahren stattgefunden.

Frankfurt am Main, der 22.04.2016

(Amol Karandikar)